A numerical study on the irregular roughness effects in compressible natural convection flow

任, 淳麒

(Degree)
博士（工学）

(Date of Degree)
2023-03-25

(Date of Publication)
2024-03-01

(Resource Type)
doctoral thesis

(Report Number)
甲第8656号

(URL)
https://hdl.handle.net/20.500.14094/0100482404

博 士 論 文

A numerical study on the irregular roughness effects in compressible natural convection flow

圧縮性自然対流における不規則粗度の影響に関する数値解析

２０２３年１月

神戸大学大学院システム情報学研究科

任 涛麒　REN BOQI

A numerical study on the irregular roughness effects in compressible natural convection flow

圧縮性自然対流における不規則粗度の影響に関する数値解析

by

Ren Boqi

A Dissertation

Submitted to Graduate School of System Informatics

In Partial Fulfilment of the Requirements

For DOCTOR OF PHILOSOPHY

January 2023

TABLE OF CONTENTS

ABSTRACT

Natural convection in a three-dimensional square cavity with isotropic irregular roughness on both vertical walls is studied numerically considering the compressibility of the working fluid under both laminar and turbulent conditions. Based on consideration of realistic conditions, the roughness is generated using a given power spectrum density, and a compressible solver with preconditioning that uses a dual time-stepping method is applied to handle the low velocity of the natural convection flow. The compressible solver demonstrates satisfactory accuracy in terms of the average Nusselt number (*Nu*) when compared with incompressible benchmark solutions. However, the results for the local Nusselt number from the compressible and incompressible solvers differ. As the temperature difference between the two vertical sidewalls increases, the maximum value of the local Nusselt number increases, but in the downstream region, the local Nusselt number actually decreases.

It is found that the surface roughness affects the temperature fields near the wall but there is no effect on the temperature at the cavity center. The existence of roughness peaks will amplify the local *Nu* and under the condition of Rayleigh number (*Ra*) equal to 10^6, as the roll-off wavenumber of roughness elements increases, this augment will increase as well. In contrast, the rough valleys will decrease the local *Nu*. Further, the partial average *Nu* over the roughness top region is affected slightly by the change of roughness roll-off wavenumber, but this effect is much more appreciable on the partial average *Nu* over the roughness bottom region. For the average *Nu* over an entire rough surface, the increase of roll-off wavenumber causes the decrease in average *Nu*.

For a *Ra* of 1×10^{10}, the turbulent natural convection flows in a cavity of aspect ratio 4 with irregular roughness on vertical isothermal sidewalls have been investigated using the method of compressible direct numerical simulation (DNS). The profiles of probability density functions of the thermal and hydrodynamic quantities show that at this *Ra*, the roughness will increase the instability of the nearby fluid. At the quasi-steady state, the results show the cavity with rough sidewalls has a lower Nusselt number on the hot wall than the smooth cavity. In other words, the roughness has a negative effect on the wall heat transfer performance. However, the results of eddy heat flux (*EHF*) represent the turbulent flows generated by the

roughness will enhance the heat transfer near the sidewalls obviously. For the instantaneous results, the isosurfaces of the Q-criterion uncover that the vortex will be generated in the vicinity of roughness peaks and increase the local heat transfer, but in the valley regions, it is difficult to find the vortex structures like the peak region. As Ra increases, the mixing effects of turbulent flows will strengthen, then the disparity of the average Nusselt number on the sidewall between rough and smooth cases will be reduced.

ACKNOWLEDGEMENT

I would like to acknowledge and give my most sincere gratitude to my supervisor Prof. Makoto Tsubokura who made this work possible. His continuous guidance and advice carried me throughout my doctorial study. I will never forget the hearty encouragement he gave me when I was in the dark and motivate me to keep going.

I should also state my thanks to Dr. Chung-gang Li, National Cheng Kung University, Taiwan for his patience, discussions on research topic and significant comments and suggestions.

Last but not the least, I expressed my deepest thanks to my parents Mr. Wanyin Ren and Mrs. MingJing Qu for their continuous support and understanding. Whenever, they are always there for me.

Boqi Ren

Computational Fluid Dynamics Lab.

Graduate School of System Informatics

Kobe University, Japan

January, 2023

LIST OF TABLES

LIST OF FIGURES

NOMENCLATURE

Roman Symbols

A	Projected Area of a surface
ACF	Autocorrelation function of the roughness element heights
C	Magnitude of power spectral density of a rough surface
C_p	Specific heat of the fluid
e	Specific energy
EHF	Eddy heat flux
g	Gravitational acceleration
h	Height of individual roughness element
H	Hurst exponent
k	Thermal conductivity
L_1, L_2, L_3	Width, Height and Depth of the cavity
n	Local normal direction of the measured surface
Nu	Nusselt number
P	Pressure
Pr	Prandtl number
q	Wavevector or wavenumber of roughness elements
R	Gas constant
Ra	Rayleigh number based on cavity height
Re	Reynolds number
t	Physical time
T	Temperature
u_1, u_2, u_3	Velocity components in x_1, x_2 and x_3 directions
w	Interpolation weight
x_1, x_2, x_3	Spatial coordinates

Greek Symbols

α	Thermal diffusivity
β	Expansion coefficient of fluid
γ	Specific heat ratio

Γ	Time derivative preconditioning matrix
δ_{ij}	Kronecker delta
δ_{x_i}	Central difference operator
ε	Dissipation rate of turbulent kinetic energy
ϵ	Temperature difference ratio
η	Kolmogorov microscale
θ	Direction of the distance vector on surface roughness
μ	Dynamic viscosity
ν	Kinematic viscosity
ρ	Density of fluid
σ	Root-mean square of the roughness element heights
τ	Artificial time or shear stress
ϕ	Arbitrary physical value
φ	Phase of roughness

Subscripts

0	Ambient or initial value
C	Cold wall
H	Hot wall
i, j, k	Indices for Cartesian coordinates
IC	Interface cell
IP	Image point
l	Local value
L	Largest wavelength or left cell face value
overall	Average value over an entire sidewall
p	Primitive form of variables
ref	Reference quantity
R	Roll-off wavenumber or right cell face value
S	Smallest wavelength
w	Quantity on the wall

Superscripts and Other Symbols

H	Physical quantity in halo cell
k	Artificial time
n	Physical time
t	Physical quantity in fine cube
T	Physical quantity in coarse cube
$*$	Nondimensional value
$< >$	Ensemble average quantity
$\bar{}$	Time-averaged and spanwise-averaged result
$'$	Fluctuation of physical value with respect to corresponding average

Abbreviation

BCM	Building-cube method
CFL	Courant–Friedrichs–Lewy condition or Courant number
DNS	Direct numerical simulation
FT, IFT	Fourier transform and inverse Fourier transform
IBM	Immersed-boundary method
LUSGS	Lower-upper symmetric-Gauss-Seidel
MUSCL	Monotonic upstream-centered scheme for conservation laws
PSD	Power spectral density
RMS	Root-mean square

CHAPTER 1. INTRODUCTION

1.1 Natural Convection

Heat transfer is one of the most common phenomena in modern industry and daily life, and attracts lots of researchers, engineers and manufacturers. Roughly, heat transfer can be classified into these three forms: Radiation, Conduction and Convection[1]. The thermal convection widely exists in the applications where the fluid are involved in the heat transfer, such as power generators and turbines, and according to the driven forces of the fluid, convective heat transfer is further divided into forced convection, natural convection and combined-convection. In this study, the major concern is natural convection where the buoyancy force plays a role as the driving force of the fluid flow. The generation of buoyancy originates from the inhomogeneous density of the fluid, i.e. the fluid motion is not driven by any external force. The denser or heavier particles of fluid will be pulled by the gravity more strongly than the lighter particles, thus the relative motion inside the fluid will occur, and as the carrier of the energy and mass, convection of the fluid will bring the delivery of the energy. Generally, without considering the phase change, the temperature difference will mostly cause the density difference. In terms of the directions of the temperature gradient and the gravitational acceleration, the natural convection of the fluid will show different forms. Figure 1.1 shows three typical examples. In these examples of natural convection flows, the temperature difference and the characteristic length are two key points to affect the instability of the fluid flow. Therefore, one dimensionless parameter, Rayleigh number (Ra), has been introduced to describe the structure of fluid flows. The classical form of Ra can be defined as following,

$$Ra_x = \frac{g\beta}{\nu\alpha}(T_w - T_\infty)x^3 \tag{1.1}$$

where, g represents the acceleration caused by the gravity, β is the expansion coefficient of the working fluid, ν is the kinematic viscosity, α is the thermal diffusivity, x is the characteristic length and T_w, T_∞ indicate the temperature on the object surface and the temperature of the fluid far from the object surface respectively.

No matter in nature or in engineering applications, the phenomenon of natural convection is so dominant and significant that it attracts lots of attention and interest from researchers and

engineers. Since no external source is required, natural convection can be found in small-scale to large-scale industrial applications. Thus, a better understanding of natural convection will lead to improving efficiency and saving energy.

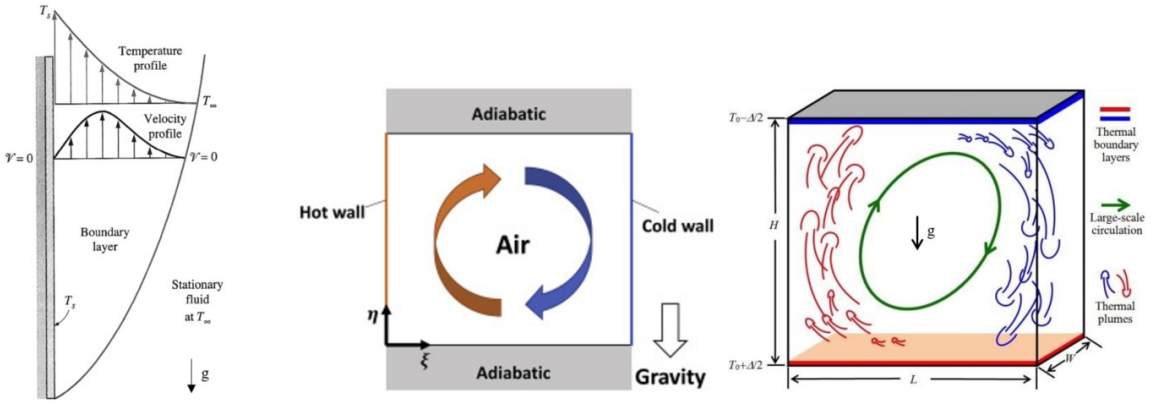

(a) (b) (c)

Figure 1.1. Typical natural convection examples: (a) over a hot vertical plate[2], (b) in an enclosured cavity with vertical heated walls[3], (c) Rayleigh-Bénard thermal convection[4].

1.2 Boussinesq or non-Boussinesq considerations

Due to the universality of natural convection, large volume numerical methods have been developed by previous researchers. One of the vital issues which all researchers should pay attention to is the change in the fluid density because of the change in temperature and the heat transfer. In order to deal with this issue, the Boussinesq approximation has been proposed. According to this approximation, the variation of the fluid density will only be considered when it is multiplied by the gravitational acceleration in the body force term of the momentum equations, and the fluctuations of density in the motion of the fluid are principally treated as the results from the heat transfer [5]. The other variations of fluid properties are negligible entirely. Thus, under the Boussinesq approximation, the continuity equation will keep its incompressible form and be able to deal with the effects of buoyancy in the flow problems. Obviously, the Boussinesq approximation will be valid under some specific conditions. Gray and Giorgini[6] assessed the validity of this approximation for liquids and gases, and pointed out that for the Rayleigh-Bénard problems, when the working fluid is air, the temperature difference should be smaller than 28.6K and the distance between roof and bottom boundaries should be smaller than 8.3×10^4 cm. For the flows in an enclosure cavity with 2 vertical heated

sidewalls, when the temperature difference ratio which is defined as $\epsilon = (T_H - T_C)/T_C$ is more than 0.1, the Boussinesq approximation might not be accurate[7]. For natural convection flows, the Mach numbers of main flows are usually much smaller than forced convection, a high enough temperature difference can also affect the velocity fields and heat transfer distributions[8]. Paillere et al.[9] found large temperature difference will result in the non-symmetrical distribution of the heat transfer and the flow patterns, and the compressibility of the fluid must be taken into account and due to the low Mach number in natural convection flow, Low-Mach approximated solver is necessary[10]. Talukdar et al[11] also observed the anti-symmetry in the patterns of buoyancy-driven laminar flows in the square cavities, and the emergence of this anti-symmetry was attributed to the temperature-dependent fluid properties. Hamimid et al.[12] showed that the Boussinesq approximation will lack the accuracy to simulate the double-diffusive natural convective flow problem at a high buoyancy ratio, because in this situation, the temperature/solutal difference will conspicuously modify the physical properties of the fluid and the flow is compressible. There is no doubt that the Boussinesq approximation can be very convenient for incompressible solvers to handle the problems which involve the fluctuations of the fluid density, but the limitations of this approximation deserve thoughtful consideration. Although the mathematical formulations would be more complex when the fluid properties are variable[13], from the view of realistic industrial equipment, natural convection tends to occur under relatively imperfect and extreme conditions. For the applications which demand high heat transfer efficiencies, such as solar collectors, nuclear reactors, or building ventilation, because of the large and complex structures or the working environment of the extremely large temperature difference, it is difficult to investigate them through the numerical methods with Boussinesq approximation or the experimental methods in laboratory scale. Hence, it is of great significance to implement the numerical analysis under the non-Boussinesq conditions.

1.3 Surface roughness

For solid materials, the surface roughness is inevitable and roughness can influence the flow field near the surface directly, thus there are numerous studies on it. In terms of the typology, the rough surfaces can be generally classified into homogeneous and inhomogeneous[14], as shown in Figure 1.2. Most engineering surfaces can be categorized into homogeneous surfaces. The homogeneous surface will be further divided into deterministic

and random surfaces according to the shapes of the roughness elements. For the deterministic surface, the roughness elements have identical shapes and sizes or periodically changing shapes. That means the shapes or the sizes of roughness elements are regular. The effects of the deterministic roughness on the flow field are more predictable, so the researchers and engineers can choose different types of roughness according to demand. However, for the random roughness, as the name implies, the most notable characteristic is the irregular element distribution. It is clear that in nature most surfaces show the characteristic of random roughness. Figure 1.3 shows the examples of these two different solid surface types. Because of the randomness of roughness element distribution, some statistical methods should be utilized to describe one random solid surface. Let us take $h(x, y)$ to represent the local height on one random rough surface, (x, y) is the location on the mean plane of the rough surface where the ensemble average of h equals 0. If the distribution of the local height h fits a Gaussian distribution, then this random rough surface is a Gaussian rough surface, otherwise, the surface is a non-Gaussian rough surface. In industry, the processing methods will determine the types of surfaces. Some cumulative processes like electropolishing or grinding will usually generate a surface of Gaussian type, and some single-point processes will lead to a non-Gaussian surface and anisotropic[17]. Furthermore, to uncover the statistical information on the random rough surface detailly, the power spectral density (*PSD*) of the surface is necessary[18]. We can draw an analogy between a randomly rough surface with a combination of several waves with different amplitudes and wavelengths. So, the *PSD* can depict the distribution of the roughness elements on the inverse-length units. Different from other description methods such as root-mean square (*RMS*), *PSD* contains the surface information in both lateral and vertical directions, and different techniques of roughness measurement can be easily and conveniently expressed through the *PSD* function[19]. In current research, the *PSD* has been adopted as the main method to express and generate the random rough surface.

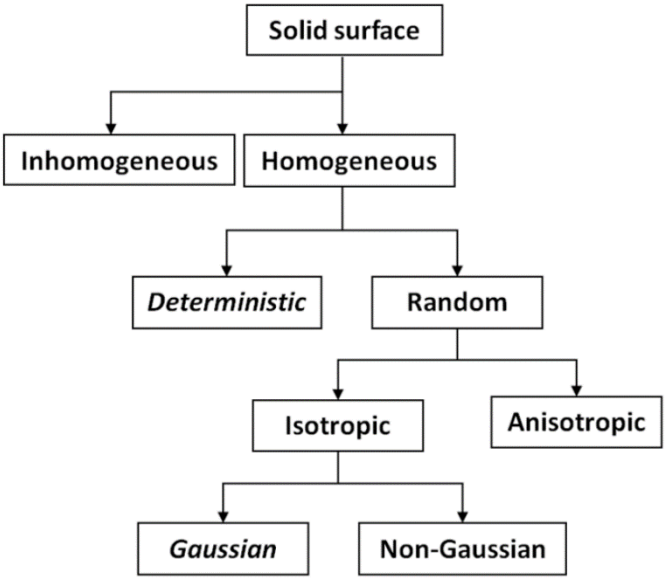

Figure 1.2. The general typology of solid surfaces.

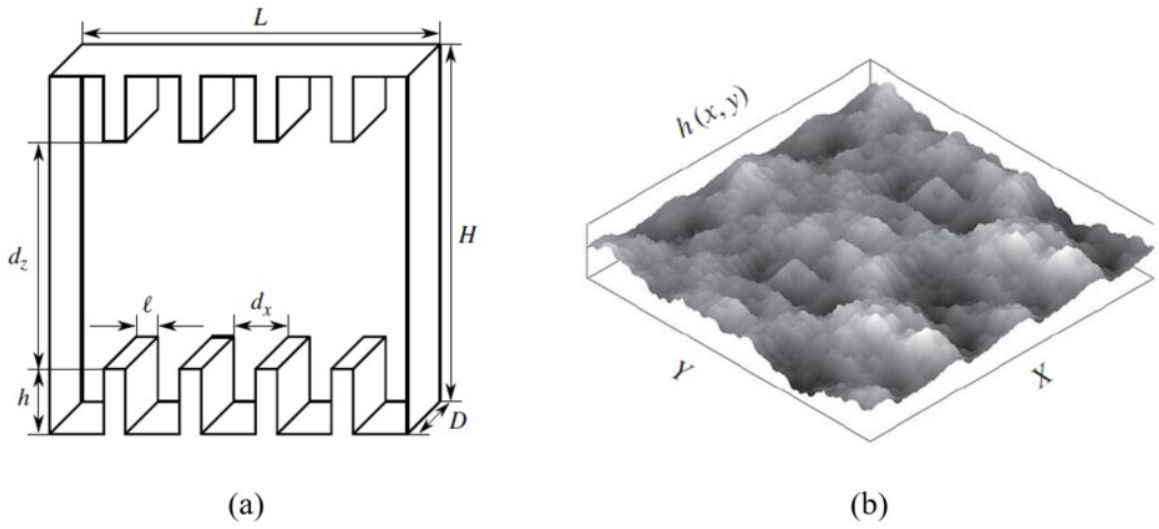

Figure 1.3. Comparision of different solid surface: (a) deterministic[15], (b) random[16].

1.4 Previous investigations

For the situation of high-temperature difference (>30K), the compressibility of the fluid should be considered during the numerical calculations, thus it is necessary to utilize the compressible flow solver due to the conspicuous density variations of fluid. But, the magnitude of fluid speed is too small compared with the speed of sound, as the result, the original

compressible solver is not allowed to be used directly. Thus, Weiss and Smith[20] adopted the preconditioning method to natural convection in a horizontal annulus and the results showed that the accuracy of this method is satisfied at the condition of Rayleigh number equals 4.7×10^4. Yamoto et al[21] simulated the natural convection in a horizontal circular pipe using the same method to deal with compressible flows with low velocity and had proved that under the conditions of 32.5K temperature difference and $Ra = 10^5$, the preconditioning method could achieve a good agreement with experimental results in thermal boundary-layers and the heat transfer performance. Also, the preconditioning method can accelerate the simulation to the convergence in a steady situation[22].

Natural convection flows in enclosed cavities with differently heated sidewalls have been studied extensively. From the achievements of previous researchers[23-26], flow mechanisms have been interpreted meticulously, and the benchmark solutions of heat transfer (Nusselt number) and hydrodynamic performance (maximum value of velocity and its location) have been calculated and obtained accurately. Under the consideration of non-Boussinesq approximation, Chenoweth and Paolucci[27] reported that in 2D cavities, the temperature-difference parameter has a conspicuous influence on the temperature and velocity fields, while the average Nu is quite independent of the changes in temperature difference. Wang et al. [28] also found this phenomenon in a wider *Ra* range from 10^5 to 2×10^9. Demou et al.[29] conducted the simulations in a 3D cavity with an aspect ratio equal to 4, the results showed that when *Ra* is set at 2×10^9, the transition can be found in the downstream regions on both hot and cold walls, and as the temperature difference between the heated walls increases, the laminar-turbulence transition point on the hot wall will move upstream but on the cold wall, this point will move downstream. The movement of transition points cannot be found in 2D simulations clearly. According to the results of direct numerical simulations (DNS) in 2D and 3D cavities, M Soria et al.[30] concluded that for natural convection flows in enclosure cavities, the 2D simulation may only be enough for general features, such as average *Nu*. When it comes to turbulent statistics, 3D simulations are necessary.

The methods to enhance the heat transfer property of natural convection flows, such as nanofluids[31], bubbles[32], and roughness or partitions[33] on the heated walls, have been studied extensively and the method of roughness or partitions on the sidewalls has been proved as an effective way to influence the heat transfer. Xu et al.[34] installed a thin fin on the hot sidewall of a differentially heated cavity, and investigated the effects of this fin on the flow field. At the *Ra* of 2.29×10^8, and behind the fin, the intermittent plume of the fluid will be

generated due to the existence of the adverse temperature gradient in this region. The intermittent plume will trigger the fluctuations of the thermal boundary layer in the downstream area, then, near the fin, natural convection flows will be periodic based on time. Further, Dou and Jiang[35] showed the influence of the fin number on the hot sidewall on the heat transfer performance. At *Ra* of 3.38×10^6, the fin will aggravate the average *Nu*, but enhance the heat transfer at a higher *Ra* of 3.38×10^9. Differently, the effect of the fin number can be ignored at both *Ra*. Yousaf and Usman[36] used the Lattice Boltzmann method to study the influence of the sinusoidal roughness elements on vertical sidewalls on the heat transfer in a two-dimensional square cavity. They found that, under a condition of laminar flow ($Ra = 10^3$ to 10^6), as the number and size of roughness elements increase, the heat transfer performance decreases. At the same time, some eddies were observed in the interstice between two roughness elements at $Ra = 10^4$, but disappeared in the case of 10^6. The authors pointed out the reason may be the larger Rayleigh number brings larger buoyancy to the fluid and then prevented the fluid gets trapped between two roughness elements. Shakerin et al[37] took the method of the experiment to investigate the flow field in an air-filled square cavity with single discrete rectangular roughness on the hot sidewall. The results showed, at the Rayleigh number of 10^8, no obvious eddy was observed in the vicinity of the roughness element, and compared with the smooth case, in the region just below and above the roughness element, the heat flux was reduced along the wall. Mohebbi et al[38] researched the natural convection flows in 2D square cavities filled with nanofluid using the Lattice Boltzmann method. Square roughness elements had been chosen to install on the vertical sidewall. The results indicated that when the size of roughness elements was one-tenth of the cavity height, the influence of the element number depended on *Ra*. For a lower *Ra* ($Ra =10^3$), the average *Nu* on the hot wall was independent of the roughness element number, while for a higher *Ra* ($Ra = 10^6$), as the roughness element number increased from 0 to 4, the average *Nu* decreased, and the number changed from 4 to 6, the average *Nu* kept constant. H Jiang et al. [39] used both experimental and incompressible numerical methods to investigate the natural convection in a rectangular cell with asymmetric ratchet surfaces at $Ra = 5.7 \times 10^9$. For the case with vertical heated sidewalls, they found that the roughness increased the Reynolds number (*Re*) of the large-scale circulation roll and the case where the large-scale circulation roll sweeping along the smaller slope side of the ratchet surfaces had a better performance in heat transfer than the case where the large-scale circulation roll flowing along the steeper slope of the ratchets. But, for the Rayleigh-Bénard convection with ratchet-shaped roughness on horizontal walls, the result was opposite, that the large-scale circulation roll sweeping along the larger slope side of the ratchet

surfaces had a better heat transfer. This difference could be attributed to the plume emissions. When the circulation flow hit the sharp corners on the roughness elements, a greater number of emissions was caused and the convection from the boundary to the cavity bulk will be intensified.

In most of the above researches, the thin sheet, rectangular or sinusoidal were chosen as the shapes of roughness or partition. Considering the wall roughness geometry is characterized by irregular shapes in nature and engineering, Napoli et al[40] introduced the effective slope as a universal geometrical parameter to characterize the shapes of the irregular rough walls. At the condition of turbulence, Peeters and Sandham[41] researched the forced convection in the channel with cold irregular rough top and bottom filled with heated fluid. The authors found that the Reynolds stress and the heat flux near the rough wall decreased as the sizes of roughness elements increased. Kuwata[42] conducted similar simulations and the results showed, above the mean plane of the roughness, the sum of the viscous drag and pressure terms was much larger than the wall heat transfer term, thus, the Reynolds analogy factors of the rough walls decreased as the effect slope increased. For the laminar flows, the convections in microtubes with 3D random rough surfaces had been studied by Xiong and Chung[43] and it had been found that in the range of Reynolds number equal to 40 to 2000, the influence of roughness on the heat transfer could be ignored.

1.5 Overview of the present study

The main objective of this study can be summed up as investigating the effects of 3D irregular surface roughness on natural convection flows in enclosed cavities considering the compressibility of the working fluid. To fulfill this objective, the process of current research has been divided into the following three sub-objectives:

- Generate and install the 3D irregular surface roughness on the sidewalls of cavities.
- Investigate the effects of different surface roughness on the heat transfer performance inside the cavities.
- Investigate the influence of one certain irregular rough surface on flow fields and heat transfer of cavity flows under different Rayleigh numbers.

To fit the reality of industrial devices' surfaces, irregular or random surface roughness should be considered. Due to the complexity of the geometric features, the roughness is generated through a given power spectrum density function and this given *PSD* function comes from the measurements of real industrial or natural surfaces. By changing the relative parameters of the *PSD* function, different roughness with different traits will be generated. Under a constant condition, such as same temperature difference or same size of cavities, the changes of irregular roughness will directly affect the heat transfer and flow fields nearby. This is helpful to survey the changes in the fluid state and understand the mechanism hidden behind these changes. Meanwhile, as the *Ra* increases from a low level to a relatively high level, the instability of the fluid will increase. Since the fluid flows differently from laminar to turbulent situations, the effects of one surface roughness will be different as well. Therefore, there is significance to investigating the influence of irregular roughness under different *Ra*.

In terms of the above three sub-objectives, the dissertation is organized in the following sequence.

In Chapter 2, the governing equations and relevant numerical methods for compressible natural-convection flows will be introduced in detail. Because of the complex geometry of the irregular roughness, the immersed-boundary method (IBM)[44] is adopted in this study. On the other hand, to capture the information on the roughness accurately, the building-cube method (BCM)[45] is chosen to generate the numerical grids for the large-scale simulations.

In Chapter 3, the method to generate the 3D irregular roughness will be presented. The examples of *PSD* measured from reality will be shown, and the *PSD* type used in this study will be discussed.

The results of laminar flows in one square cavity will be reported in Chapter 4. The smooth and rough sidewalls will be installed respectively. In this chapter, the numerical method described in Chapter 2 will be proved effective and efficient to deal with the low-match natural convection considering the fluid's compressibility and with the complex boundaries. The flow fields near both smooth and rough sidewalls will be also discussed.

Chapter 5 will show the results of the cavity flows with different rough surfaces. The specific differences of these rough surfaces will be described. Details of the flow fields near different irregular rough surfaces will be compared with each other. The temperature gradients inside the cavities will be shown and discussed.

In Chapter 6, the influence of one certain irregular surface roughness will be first investigated under turbulent condition. The statistical results of the flow fields near the rough sidewall will be compared with the smooth case. Comparison will be also made to Nusselt numbers and the results of eddy heat flux. Then, under different Rayleigh numbers, the influence of the roughness under different Rayleigh numbers will be discussed.

The conclusions of current studies will be eventually presented in Chapter 7 as well as suggestions for future works.

CHAPTER 2. GOVERNING EQUATIONS AND NUMERICAL METHOD

2.1 Governing Equations

To deal with the the natural convection under high temperature differences, the compressible governing equation has been considered, and the abbreviation for the governing equation is shown like the following form:

$$\frac{\partial U}{\partial t}+\frac{\partial F_1}{\partial x_1}+\frac{\partial F_2}{\partial x_2}+\frac{\partial F_3}{\partial x_3}=S \tag{2.1}$$

U and F_i can be written in following format,

$$U=\begin{bmatrix}\rho\\ \rho u_1\\ \rho u_2\\ \rho u_3\\ \rho e\end{bmatrix} \tag{2.2}$$

$$F_i=\begin{bmatrix}\rho u_i\\ \rho u_i u_1+P\delta_{i1}-\mu A_{i1}\\ \rho u_i u_2+P\delta_{i2}-\mu A_{i2}\\ \rho u_i u_3+P\delta_{i3}-\mu A_{i3}\\ (\rho e+P)u_i-\mu A_{ij}u_j-k\dfrac{\partial T}{\partial x_i}\end{bmatrix}, \forall i=1,2,3 \tag{2.3}$$

and

$$S=\begin{bmatrix}0\\ 0\\ -(\rho-\rho_0)g\\ 0\\ -(\rho-\rho_0)gu_2\end{bmatrix} \tag{2.4}$$

where specific energy is $e=\frac{P}{\rho(\gamma-1)}+\frac{1}{2}({u_1}^2+{u_2}^2+{u_3}^2)$, μA_{ij} indicates the stress term with $A_{ij}=\partial u_j/\partial x_i+\partial u_i/\partial x_j-2/3(\nabla\cdot u)\delta_{ij}$ and δ_{ij} is Kronecker delta. The relationship between pressure and density of air is represented by the ideal gas equation, $P=\rho RT$. According to Sutherland's Law[46], the dynamic viscosity and thermal conductivity of working fluid are determined as:

$$\mu(T) = \mu_0 \left(\frac{T}{T_0}\right)^{\frac{3}{2}} \frac{T_0 + 110.4}{T + 110.4} \tag{2.5}$$

$$k(T) = \frac{\mu(T)\gamma R}{(\gamma - 1)Pr} \tag{2.6}$$

where, the reference temperature of the fluid: $T_0 = 298.06\,K$, the reference fluid density at reference temperature: $\rho_0 = 1.18\,kg/m^3$, acceleration due to gravity: $g = 9.81\,m/s^2$, the reference dynamic viscosity: $\mu_0 = 1.85 \times 10^{-5}\,N \cdot s/m^2$, specific heat ratio: $\gamma = 1.4$, gas constant: $R = 287\,J/kg$, and Prandtl number: $Pr = 0.72$.

2.2 Numerical Method

For natural convection, the magnitude of fluid velocity due to the buoyancy force is generally smaller than the speed of sound by several orders of magnitude. For this reason, original compressible solvers are unsuited for this kind of flow field. To increase the efficiency of solving natural convection problems of compressible flows, a preconditioning method is adopted to resolve the governing equations which are developed by Weiss and Smith[20]. Combined with the Roe scheme[47] and dual time-stepping method[48], the new governing equation is shown as:

$$\Gamma \frac{\partial U_p}{\partial \tau} + \frac{\partial U}{\partial t} + \frac{\partial F_1}{\partial x_1} + \frac{\partial F_2}{\partial x_2} + \frac{\partial F_3}{\partial x_3} = S \tag{2.7}$$

where, Γ is the preconditioning matrix provided by Weiss and Smith, and U_p is the primitive form of the variables, $[P, u_1, u_2, u_3, T]$, but U is the conservative form of $[\rho, \rho u_1, \rho u_2, \rho u_3, \rho e]$. τ and t represent the artificial and physical time respectively. Here, the dual time stepping technique is applied for speedy convergence of simulation and to ensure the stability of the numerical scheme.

The discretized form of Eq. (2.7) is

$$\Gamma \frac{U_p^{k+1} - U_p^k}{\Delta\tau} + \frac{3U^{k+1} - 4U^n + U^{n-1}}{2\Delta t} + \frac{1}{\Delta x_1}\left(F_{1_{i+\frac{1}{2},j,k}}^{k+1} - F_{1_{i-\frac{1}{2},j,k}}^{k+1}\right) + \frac{1}{\Delta x_2}\left(F_{2_{i,j+\frac{1}{2},k}}^{k+1} - F_{1_{i,j-\frac{1}{2},k}}^{k+1}\right) + \frac{1}{\Delta x_3}\left(F_{3_{i,j,k+\frac{1}{2}}}^{k+1} - F_{3_{i,j,k-\frac{1}{2}}}^{k+1}\right) = S^k \tag{2.8}$$

The iteration of artificial time and physical time is shown through two superscripts k and n in Eq.(2.8). It is noting that, when the iteration of artificial time reaches a situation of convergence, the residual of $\partial U_p/\partial\tau$ less than 10^{-3}, the magnitude of the artificial term at (k+1)th step is equivalent to the magintude of physical time term at (n+1)th step, then, Eq. (2.8) would return back to the original Navier-Stokes equation approximately.

Afterward, it is necessary to linearize the terms of U^{k+1} and F_i^{k+1}. Thus, these terms can be expressed as follows:

$$U^{k+1} = U^k + M\Delta U_p \tag{2.9}$$

$$F_1^{k+1} = F_1^k + A_p\Delta U_p \tag{2.10}$$

where, $M = \partial U/\,\partial U_p$, $\Delta U_p = U_p^{k+1} - U_p^k$. A_p is the flux Jacobian ($A_p = \partial F_1^k/\partial U_p$) and in the other 2 directions, the flux Jacobians are $B_p = \partial F_2^k/\partial U_p$, $C_p = \partial F_3^k/\partial U_p$ for F_2^{k+1} and F_3^{k+1} respectively.

Thus, by substituting Eq. (2.9) and Eq. (2.10) into Eq. (2.8), the Eq. (2.8) can be rewritten into the following format as

$$\left[\frac{I}{\Delta\tau} + \Gamma^{-1}M\frac{3}{2\Delta t} + \Gamma^{-1}\left(\delta_{x_1}A_p^k + \delta_{x_2}B_p^k + \delta_{x_3}C_p^k\right)\right]\Delta U_p = \Gamma^{-1}R^k \tag{2.11}$$

where, $R^k = S^k - (3U^k - 4U^n + U^{n-1})/2\Delta t - (\delta_{x_1}F_1^k + \delta_{x_2}F_2^k + \delta_{x_3}F_3^k)$, and δ_{x_i} is the central-difference operator. After the convergence in artificial time term, Eq. (2.11) can be rewritten into Eq. (2.12):

$$\left[\Gamma^{-1}M\frac{3}{2\Delta t} + \Gamma^{-1}\left(\delta_{x_1}A_p^k + \delta_{x_2}B_p^k + \delta_{x_3}C_p^k\right)\right]\Delta U_p = \Gamma^{-1}R^k \tag{2.12}$$

The lower-upper symmetric-Gauss-Seidel (LUSGS) implicit method is then used to solve Eq. (2.12). To perform the calculation of R^k in Eq. (2.12), it is helpful to divide the flux term in Eq.(2.3) into inviscid term and viscid term, shown in Eq.(2.13) and Eq.(2.14) respectively. Then the inviscid term in Eq.(2.12) can be discretized into Eq.(2.15) through Roe upwind scheme.

$$F_{inviscid} = \begin{pmatrix} \rho u_i \\ \rho u_i u_1 + P\delta_{i1} \\ \rho u_i u_2 + P\delta_{i2} \\ \rho u_i u_3 + P\delta_{i3} \\ (\rho e + P)u_i \end{pmatrix} \tag{2.13}$$

$$F_{viscous} = -\begin{pmatrix} 0 \\ \mu A_{i1} \\ \mu A_{i2} \\ \mu A_{i3} \\ \mu A_{ij} u_j + k \dfrac{\partial T}{\partial x_i} \end{pmatrix} \tag{2.14}$$

$$F_{inviscid,i+\frac{1}{2}} = \frac{1}{2}[F_R(U) + F_L(U)] + F_d \tag{2.15}$$

where, F_d is the Roe dissipation term which can be described as: $F_d = -\frac{1}{2}\{|\Gamma^{-1} A_p|\Delta U_p\}$.

For the convective terms (F_R and F_L) in Eq.(2.15), the values at interfaces of cells are calculated by interpolating the corresponding values from a group of cell centers through fifth-order Monotonic Upstream-centered Scheme for Conservation Laws (MUSCL)[49] without a limitor function, shown in following way:

$$U_{L_{1+\frac{1}{2}}} = \frac{1}{60}[-3U_{i+2} + 27U_{i+1} + 47U_i - 13U_{i-1} + 2U_{i-2}] \tag{2.16}$$

$$U_{R_{1+\frac{1}{2}}} = \frac{1}{60}[2U_{i+3} - 13U_{i+2} + 47U_{i+1} + 27U_i - 3U_{i+1}] \tag{2.17}$$

In x_1-direction, F_d is expressed by Eq. (2.19):

$$F_{d,x_1} = -\frac{1}{2}\left\{ |U_{IC}| \begin{bmatrix} \Delta\rho \\ \Delta(\rho u_1) \\ \Delta(\rho u_2) \\ \Delta(\rho u_3) \\ \Delta(\rho e) \end{bmatrix} + \delta U \begin{bmatrix} \rho \\ \rho u_1 \\ \rho u_2 \\ \rho u_3 \\ \rho H \end{bmatrix} + \delta p \begin{bmatrix} 0 \\ 1 \\ 0 \\ 0 \\ u_1 \end{bmatrix} \right\} \tag{2.18}$$

where U_{IC} is the cell interface velocity, and Δ indicates the discontinuous jumps between the left and right states which can be obtained by Eq. (2.16) and (2.17), $H = e + \frac{p}{\rho}$. δU and δp are expressed respectively as:

$$\delta U = \left(c' - \frac{1-\theta'}{2} u_1 \frac{U'}{\tilde{c}} - \theta' |u_1| \right) \frac{\Delta p}{\rho \theta c^2} + \frac{U'}{\tilde{c}} \Delta u_1 \tag{2.19}$$

$$\delta p = \frac{U'}{\tilde{c}} \Delta p + \left(c' - |u_1| + \frac{1-\theta'}{2} u_1 \frac{U'}{\tilde{c}} \right) \rho \Delta u_1 \tag{2.20}$$

where $\theta' = \min[M_{local}^2, 1]$, $\theta = \min[\max(M_{ref}^2, M_{local}^2), 1]$, M_{local} is the local Mach number and M_{ref} is a global cut-off Mach number. The discontinuous jumps of velocity and pressure are respectively calculated by $\Delta u_1 = u_{1R} - u_{1L}$ and $\Delta p = p_R - p_L$. Additionally, c represents the sound speed, $c' = 0.5\sqrt{4c^2\theta' - (1-\theta')^2 u_1^2}$, $\tilde{c} = \min[\max(M_{ref}^2, M_{local}^2), 1]c$ and $U' = 0.5(1+\theta')u_1$. It should be noted that, in the dissipation part, all variables are obtained from the Roe averages[47]. From Eq. (2.15), the calculation of inviscid terms will utilize both F_R and F_L, thus the accuracy order is sixth.

Different from the inviscid term, the viscous terms are discretized by second-order central differencing. Due to the primitive variables being defined at the location of numerical grid centers, the derivatives in viscous terms can be discretized using the following equations.

$$\frac{\partial}{\partial x_1}\left[\frac{\partial u_1}{\partial x_1}\right] = \frac{\left(u_{1_{i+1,j,k}} - 2u_{1_{i,j,k}} + u_{1_{i-1,j,k}}\right)}{(\Delta x_1)^2},$$

$$\frac{\partial}{\partial x_1}\left[\frac{\partial u_1}{\partial x_2}\right] = \frac{\left(u_{1_{i+1,j+1,k}} - u_{1_{i+1,j-1,k}} - u_{1_{i-1,j+1,k}} + u_{1_{i-1,j-1,k}}\right)}{4\Delta x_1 \Delta x_2}, \tag{2.21}$$

$$\frac{\partial}{\partial x_1}\left[\frac{\partial u_1}{\partial x_3}\right] = \frac{\left(u_{1_{i+1,j,k+1}} - u_{1_{i+1,j,k-1}} - u_{1_{i-1,j,k+1}} + u_{1_{i-1,j,k-1}}\right)}{4\Delta x_1 \Delta x_3}$$

2.3 Immersed Boundary Method for Compressible Flows

Because of the complex geometry of the irregular rough surface, the immersed boundary method (IBM)[50] has been applied to ensure that the geometrical details are reproduced as accurately as possible. The key point of IBM is to simulate the existence of geometry by imposing the physical values into the numerical grids in the vicinity of geometry. Figure 2.1 shows the configuration of IBM. The cells which are defined as interface cell (IC) has the characteristic that the distance (d) from the cell center to the closest geometry element is less than one cell size. Image point (IP) is the point that the distance from which to IC is equal to d in the normal direction of the geometry element. IC and IP must be on the same side of geometry. Then, according to the relative locations of surrounding cells to IP, the physical value at IP, ϕ_{IP}, can be calculated by bilinear interpolation:

$$\phi_{IP} = w_1\phi_1 + w_2\phi_2 + w_3\phi_3 + w_{IC}\phi_{IC} \tag{2.22}$$

where, w_1, w_2, w_3 and w_{IP} can be obtained using VanderMonde matrix [50]. Tullio et al.[51] recommended applying linear interpolation to evaluate ϕ_{IC}, shown in following equations:

$$\phi_w = \phi_{IC} - \left(\frac{\partial\phi}{\partial n}\right) d = \phi_{IC} - \frac{\phi_{IP} - \phi_w}{2d} d \tag{2.23}$$

$$\phi_{IC} = \frac{1}{2}(\phi_w + \phi_{IP}) \tag{2.24}$$

In present study, the no-slip and isothermal conditions are implemented on the walls, so ϕ_w is an assigned value ϕ_{assign}, thus the Dirichlet condition should be considered. Then according to Equations (2.22), (2.23) and (2.24), ϕ_{IC} can be presented as following:

$$\phi_{IC} = \frac{w_1\phi_1 + w_2\phi_2 + w_3\phi_3 + \phi_{assign}}{2 - w_{IC}} \tag{2.25}$$

However, for pressure, Neumann condition, which considers $\phi_w = \phi_{IP}$, should be used, then ϕ_{IC} can be presented as following:

$$\phi_{IC} = \frac{w_1\phi_1 + w_2\phi_2 + w_3\phi_3}{1 - w_{IC} + \psi} \tag{2.26}$$

where ψ is a small value to prevent the denominator becoming zero. Because when IC is very close to the wall, w_{IC} will approach 1.

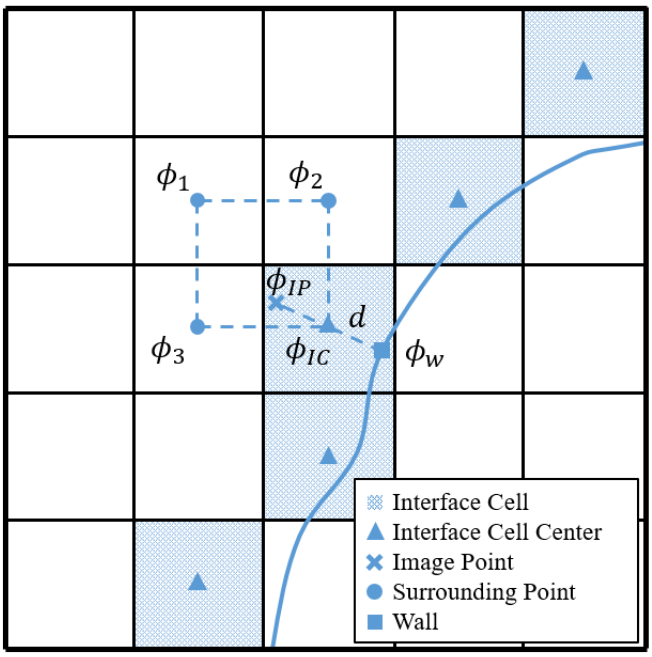

Figure 2.1. Configuration of Immersed Boundary Method.

2.4 Building Cube Method

Because of the irregular distribution and sizes of the roughness elements, the normal numerical grids in curve-linear distribution are hard to capture the detail of the roughness. In the Cartesian coordinate system, the complex geometry demands a fine distribution of numerical grids in three axes. Thus, the Building cube method (BCM)[52] has been chosen to discretized the calculation domains in present study. This method employs the uniform-spacing mesh, so it is suitable for the numerical calculation problem with complex geometry. In addition, based on the uniform-spacing mesh, it is simpler to generate mesh and program the solution algorithm. In BCM, the calculation domain will be divided into numerous cubic subdomains called cubes, and every cube will further divided into cubic cells. In this way, each cube will contain the same number of cells. Due to the equal cell number, the cubes are equal and independent of each other. So, it is easy to achieve a high parallel efficiency[53].

The density of cell in each cube is constant, but the sizes of cubes are different according to the local size of the geometry. In general, fine cubes will be arranged around the geometry to ensure accurate representation of the geometry. Figure 2.2 shows an example of numerical grids generated via BCM. The procedure of the mesh generation can be concluded in several steps. The computational domain should be determined first in terms of the simulation

conditions, such as the size of geometry and the boundary conditions. Then, the domain is divided into some coarse cubes, and to generate finer meshes, division should be repeated several times until a preset threshold such as the minimum size of the girds. In this process, the refinement ratio has to be restricted as constant for a constant mesh density in one cube. For instance, in Figure 2.2, the refinement ratio is kept as 2, and the refinement is conducted near the geometry. Therefore, the sizes of the adjacent cube are halved when moving closer to the geometry. After the determination of the cube distribution, each cube will be divided into equivalent cells and then the mesh generation is finished.

Attributed to the constant refinement ratio, the accuracy and efficiency of the data communication between cubes can be assured[54]. The calculations in the cells near the cube boundaries need the information from the neighboring cubes, so it is significant to exchange the necessary data between the cubes. A halo region are created around each cube, and the region is made up of several layers of dummy or ghost cells. The layer number is determined by the adopted numerical method. Taking one-layer halo region as the example, the ghost cells play a role as temporary storage cells for the data copied from the neighboring cubes, shown in Figure 2.3. Between cubes with the same size, the copied data can be directly used in the information communication. But for the communication between cubes with different sizes, the data interpolation has to be involved. This data interpolation is classified into these two types: interpolating data from a fine cube to a coarse one, and interpolating data from a coarse cube to a fine one. Figure 2.4 shows the diagrams of the 2 types of data interpolation respectively. For the data interpolation from fine cube to coarse cube, the exchanged data can be obtained through the following equation:

$$\phi_{I,J}^{TH} = w_{i,j}\phi_{i,j}^{t} + w_{i+1,j}\phi_{i+1,j}^{t} + w_{i,j+1}\phi_{i,j+1}^{t} + w_{i+1,j+1}\phi_{i+1,j+1}^{t} \tag{2.27}$$

here, ϕ represents the arbitrary data in the cell center, w is the interpolation weight and the superscripts (T, t and H) indicate coarse cube, fine cube and halo cell. Data exchange from a coarse cube to a fine cube halo cells can be achieved through simply copying the coarse cell data and allocating these data to all corresponding fine halo cells. This procedure shown in Figure 2.4(b) can be expressed as:

$$\phi_{I-1,J}^{T} = \phi_{i-2,j}^{tH} = \phi_{i-1,j}^{tH} = \phi_{i-2,j+1}^{tH} = \phi_{i-1,j+1}^{tH} \tag{2.28}$$

In summary, uniform spacing and the equal number of mesh in each cube make it easy to deal with massively parallel simulation with complex geometry, and the easy and

straightforward method of data exchange guaranteed the high efficiency of the information communication between the cubes.

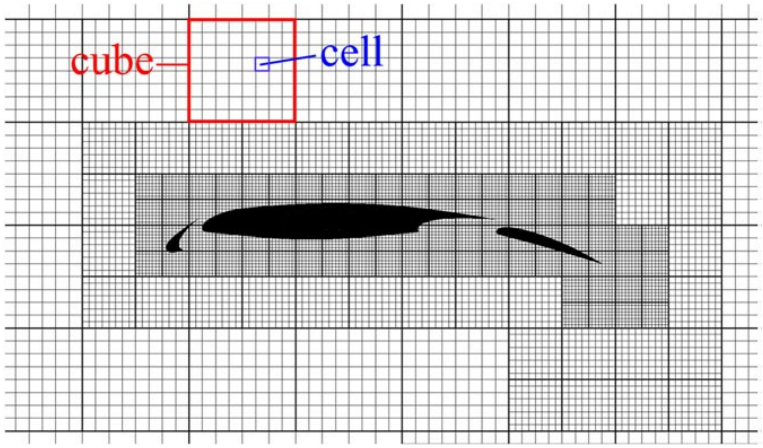

Figure 2.2. Example of BCM mesh[53].

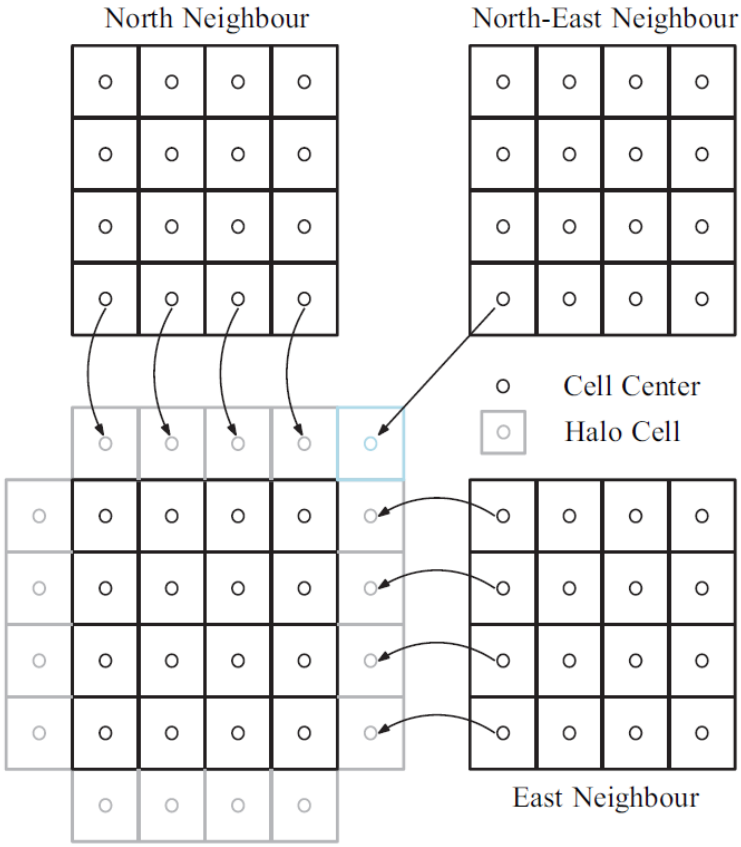

Figure 2.3. Halo region of one cube[54].

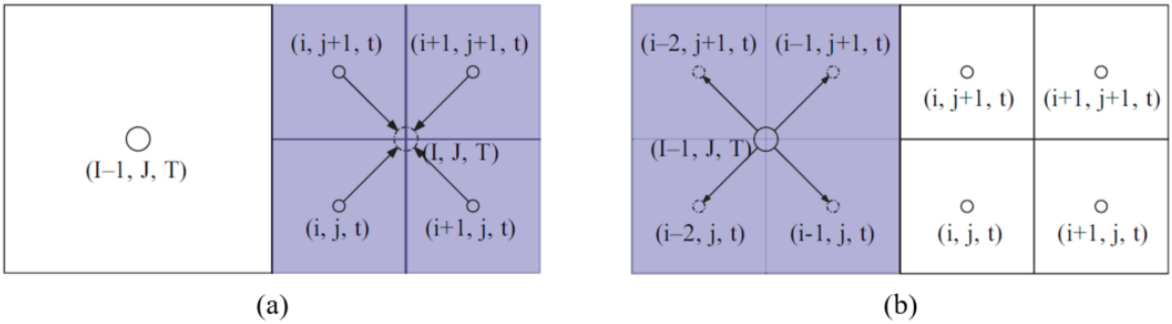

Figure 2.4. Data interpolation between cubes with different sizes. (a) from fine cube to coarse cube; (b) from coarse cube to fine cube[54].

CHAPTER 3. GENERATION OF IRREGULAR ROUGHNESS

In current study, the type of roughness has been selected as irregular and random. Different from other deterministic surfaces such as a surface with rectangular or sinusoidal roughness elements, the irregular roughness is indescribable to some extent, but it can represent the real surface roughness in nature or industry. Although a full description cannot be provided based on a finite number of parameters, a more number of parameters can describe the irregular roughness more accurately[55]. The parameters to describe an irregular roughness should include the height of the roughness element, the probability density of the roughness element's height, and the change frequency of the roughness elements and other necessary parameters, thus the power spectral density(*PSD*)[56][57] is an easy and efficient way to combine the structural information of the roughness in both vertical and lateral directions.

Consistent with Chapter 1, the height of a roughness element is indicated as h, therefore, considering an irregular roughness located in a Cartesian system, the undulation on the surface can be represented as $h(x, y)$ where x and y are Cartesian coordinates. To minimize the quantities of roughness element size, such as heights and *RMS*, $h(x, y)$ is measured from the mean plane of the roughness thus $\langle h \rangle = 0$, $\langle ... \rangle$ stands for the ensemble averaging. The spans of the rough surface in both x and y directions are denoted as L_x and L_y respectively, then the autocorrelation function (*ACF*) of the height is then defined as the following:

$$ACF(x, y) = \frac{1}{L_x L_y} \int_{-\frac{L_x}{2}}^{\frac{L_x}{2}} \int_{-\frac{L_y}{2}}^{\frac{L_y}{2}} h(x_0 + x, y_0 + y) h(x_0, y_0)\, dx_0 dy_0 \tag{3.1}$$

where, (x_0, y_0) is a point on the rough surface, and (x, y) is the in-plane distance. If the irregular roughness is isotropic, the *ACF* depends only on the distance, $r = (x^2 + y^2)^{1/2}$, but not on the the choice of (x_0, y_0), that means the location of (x_0, y_0) will not affect the result of *ACF* or the direction of the distance vector $\theta = \arctan(y/x)$ [14]. So, (x_0, y_0) can be chosen as the origin, and then (x, y) is the location on the rough surface. From Equation (3.1), it is clear that when distance is 0, then the *ACF* of the height is equivalent to the root-mean square σ of the roughness.

From Wiener–Khinchin theorem, the power spectral density (*PSD*) can be attained from the Fourier transform (FT) of *ACF*[58][59]:

$$C(q_x, q_y) = \frac{1}{4\pi^2} \iint ACF(x,y) e^{-i(xq_x + yq_y)}\, dxdy \tag{3.2}$$

here, q_x and q_y are the components of the wavevector $\boldsymbol{q}$.

The inverse Fourier transform (IFT) of Equation (3.2) follows as:

$$ACF(x,y) = \iint C(q_x, q_y) e^{i(xq_x + yq_y)}\, dq_x dq_x \tag{3.3}$$

thus, σ can be also treated as the integral of the *PSD* at the origin. This indicates the relationship between *PSD* and *RMS*. Furthermore, BNJ Persson et al.[60] pointed out when $h(x,y)$ follows a Gaussian distribution, *PSD* can completely dominate the statistical properties of the rough surface. Therefore, we can change the roughness by only changing the *PSD*.

In order to generate an irregular roughness according to a given *PSD*, more information we should know. From Equation (3.2), we can deduce that

$$\langle h(x,y) h(0) \rangle = C(x,y)$$

then Equation (3.3) can be rewritten as following:

$$C(q_x, q_y) = \frac{1}{4\pi^2} \iint C(x,y) e^{-i(xq_x + yq_y)}\, dxdy \tag{3.4}$$

The height of roughness can be represented through its Fourier series[61], shown as

$$h(x,y) = \sum_{\boldsymbol{q}} B(x,y) e^{i[xq_x + yq_y + \varphi(\boldsymbol{q})]} \tag{3.5}$$

where, $\varphi(\boldsymbol{q})$ is the phase, as mensioned above, for an isotopic roughness, the phase have no influence on the distribution of roughness elements, thus, in the roughness generation, $\varphi(\boldsymbol{q})$ is independent and uniformly distributed random variable. After substituting Equation (3.5) into Equation (3.4), and we can achieve the next equaton:

$$C(\boldsymbol{q}) = \frac{A}{(2\pi)^2} |B(\boldsymbol{q})|^2 \tag{3.6}$$

where, $A = L_x L_y$. This is an important equation, because it reveals the connection between the surface height $h(x,y)$ and the PSD. By imposing $C(\boldsymbol{q}) = C(q)$, here q is the magnitude of wavevector $\boldsymbol{q}$, the directions of wavevectors will be eliminated, thus the statistical properties of this rough surface will show as isotropic.

Figure 3.1 shows some *PSD*s of different rough surfaces[60]. From these experimental results of real surfaces, asphalt surfaces have several conspicuous features, which include a large and relatively constant *PSD*, a clear inflection point on the *PSD* curve, and a decrease of *PSD* magnitude after the inflection point. In fact, the road surface like asphalt and concrete surface has nearly perfect power spectra of the self-affine fractal surface, which forms the fundamentals for the studies of all thin-film rough surfaces. In addition, the description of the self-affine fractal surface is the most convenient and simplest[62]. This kind of surface has the property that the surface statistical properties are invariant under the uniform scaling[60][63]. For this reason, the isotropic self-affine fractal surface has been chosen in current study.

The *PSD* curve of a self-affine fractal surface can be abstracted in general terms as Figure 3.2. The curve is located in the range of $q_L < q < q_S$, here q_L and q_S represent the wavenumber of the largest wavelength and the wavenumber of the smallest wavelength respectively. Because for both experimental measurement of a real surface or the generation of the numerical surface, the spans of the surface are limited usually, thus there is a largest wavelength to restrict the smallest q, meanwhile sample interval cannot be infinitely small, so there is a smallest wavelength to restrict the largest q as well. From the figure, the curve of *PSD* is separated into two parts by a special wavenumber q_R, roll-off or cut-off wavenumber. In the range of $q_L < q < q_R$, the magnitude of *PSD* keeps invariant, and in the range of $q_R < q < q_S$, the log *C*-Log *q* plot abides a constant slope. This slope shows the power-law behavior in the power spectrum of the self-affine surface, and can be expressed as following[64]:

$$C(q) \sim q^{-2(H+1)}$$

where *H* is the Hurst exponent which is related to the fractal dimension of the surface. Therefore, a *PSD* curve will be determined with precision by giving largest *C*, q_L, q_R, q_S and *H*.

Following the theories introduced above, the generation of a numerical irregular rough surface can be broken down into these 5 steps:

Step 1: the spans of the rough surface in the Cartesian system (L_x, L_y) should be confirmed. Meanwhile, the pixel numbers along the *x* and *y* directions should be considered to guarantee appropriate q_S. After this step, the coordinates of pixels will be built.

Step 2: the pixels should be converted into a polar system. Therefore, the information of wavevectors will be generated which includes the wavenumber q and phase φ.

Step 3: the *PSD* distribution should be decided. In present study, the rough surface is chosen as an isotropic self-affine fractal surface, thus, the q_R and H should be given. In addition, based on the Equation (3.1) and (3.3), the magnitude of *PSD* can be calculated through a provided root-mean square of roughness height. After the determination of *PSD* distribution in log C–Log q domain, B(q) in Equation (3.6) can be obtained.

Step 4: in step 3, we only consider the magnitude of wavevectors because of the isotropic roughness we want to generate. But, the information of the phase is necessary, thus, the phase of the wavevector will be decided as uniformly random. After this step, all the variables on the right-hand side of Equation (3.5) have been determined.

Step 5: so far, all the information is presented in the polar system, hence, we should convert the polar system back to the Cartesian system. Then, inverse Fourier transform (IFT) has to be utilized to get the heights of roughness elements, $h(x,y)$.

Figure 3.3 shows the example of generated rough surface with the parameters of $q_R = 0.001\ m^{-1}$, $H = 0.8$, $\sigma = 0.5\ mm$.

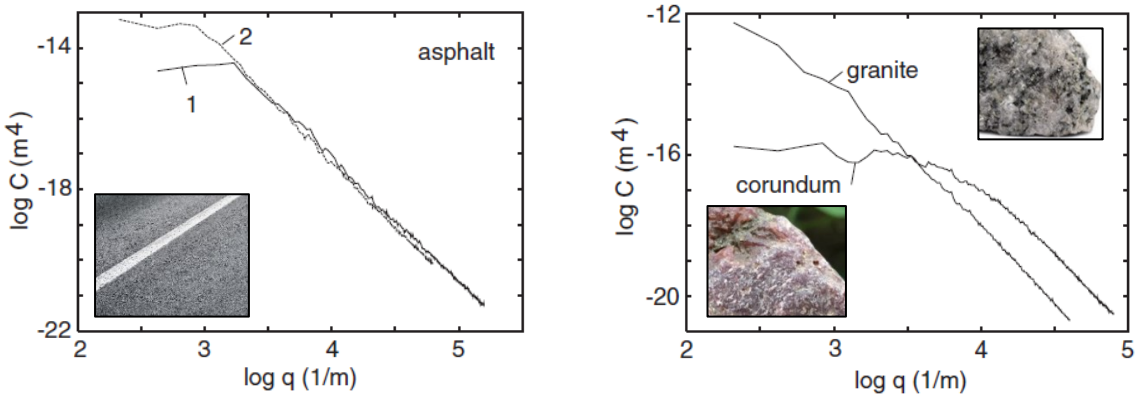

Figure 3.1. Examples of different rough surfaces and their *PSD* distributions.

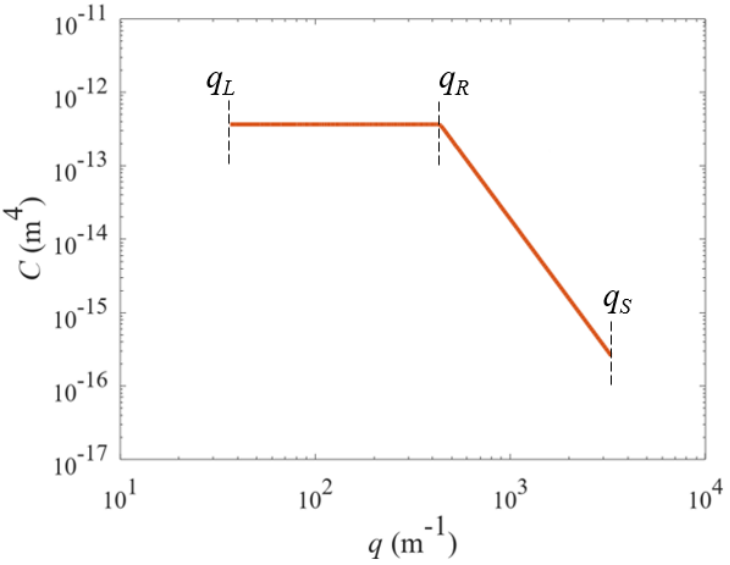

Figure 3.2. Power spectrum of a self-affine fractal rough surface.

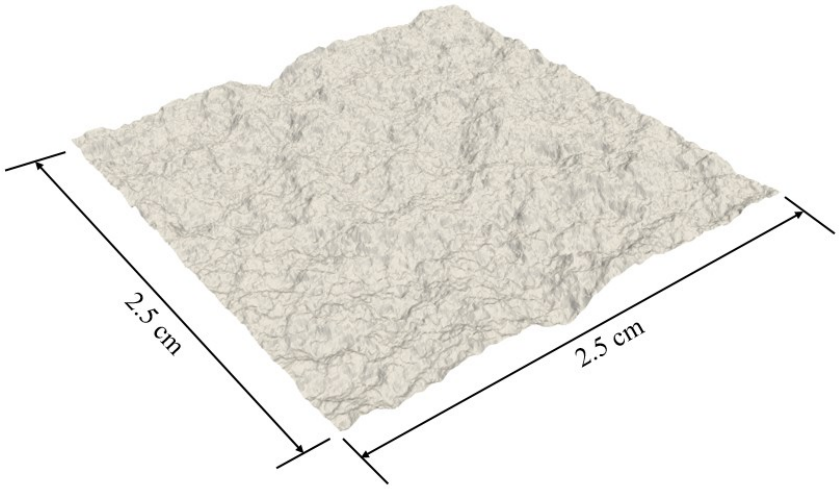

Figure 3.3. The example of a computer generated rough surface.

CHAPTER 4. LAMINAR NATURAL CONVECTION IN A SQUARE CAVITY WITH 3D RANDOM ROUGHNESS ELEMENTS CONSIDERING THE COMPRESSIBILITY OF THE FLUID

4.1 Physical Model

Because the three-dimensional geometries of random rough surfaces cannot be ignored in this work, the numerical simulations of the flows in the square cavity are performed under 3D conditions. Figure 4.1 shows the physical model of current study with differentially heated vertical sidewalls and adiabatic top and bottom surfaces. A high temperature of T_H and a low temperature of T_C, which are both constant and isothermal, are set on the left and right sidewalls, respectively. The no-slip boundary condition is imposed on the top, bottom and both sidewalls of the cavities, but slip boundary condition is imposed on both x_3-direction boundaries (at $x_3/L_3 = 0$ and$x_3/L_3 = 1$ planes). For all cavity flows, Rayleigh number is constant at 10^6. The air with a Prandtl number (Pr) of 0.72 is selected as the working fluid. The initial temperature of the air contained in the core of the square cavity is $T_0 = (T_H + T_C)/2$ and the pressure is 101,300 Pa.

The artificial random surface roughness is generated by using the method mentioned in Chapter 3 and based on a given power spectrum density (PSD), as illustrated in Figure 4.2. In this research, the root mean square roughness (σ) is equal to 1.5% of the cavity width (L_1), where, $\sigma = \sqrt{\frac{1}{n}\sum_{i=1}^{n} h_i^2}$, and h_i is the height of each roughness element from the mean plane of the roughness. On the mean plane's position, the heights of peaks and depths of valleys all add to zero. Because of the random distribution of the roughness elements, the depth-to-width aspect ratio (L_3/L_1) is selected to be 2 and the arrangement of the roughness elements is symmetrical with respect to the middle of the depth of the cavity. As noted above, in many previous works [36-38], the existence of the roughness will reduce the effective volume of fluid in the cavity. Therefore, to maintain a constant value for the effective volume, rough surfaces have been installed on both hot and cold sidewalls in this research, and the rough surface on the cold wall is generated by direct translation of the rough surface on the hot wall.

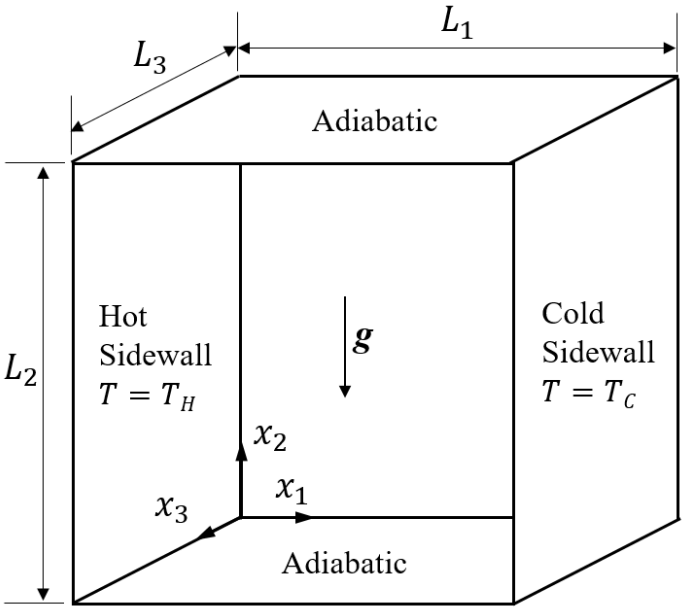

Figure 4.1. Physical Model of the Square Cavity.

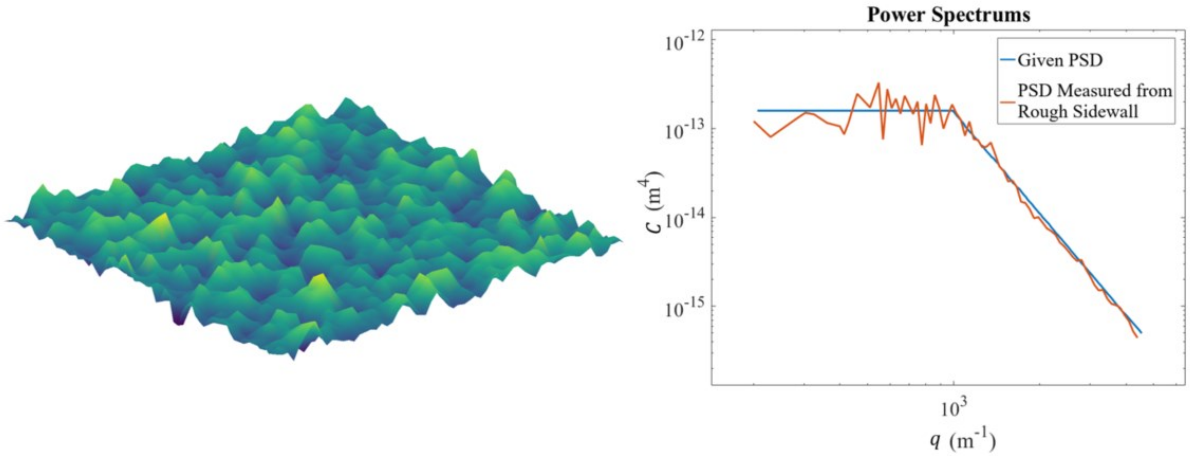

Figure 4.2. 3D random artificial roughness and the power spectrum.

4.2 Results and Discussion

4.2.1 Investigation of Fluid Compressibility in Enclosed Square Cavity

To discuss the effects of the compressible fluid on heat transfer, 3D cavities, shown in Figure 4.1, with smooth hot and cold sidewalls are investigated in this section. For all cavities, the Rayleigh number remains constant, where the Rayleigh number $Ra = g\beta_0 \Delta T {L_2}^3 Pr/{\nu_0}^2 = 10^6$ and all fluid properties are determined based on the ambient temperature.

With regard to the influence of the compressibility of the working fluid on the heat transfer, three different temperature differences (10 K, 50 K, and 120 K) have been studied and the mesh distributions have been shown in Figure 4.3 (a). The finest grids are implemented in the vicinity of two sidewalls, and to save the computational resources, the coarser grids are implemented in the core regions of the cavities. There are 256 finest grids along with the height (L_2) direction of the enclosed cavities, and the distributions of grids along the depth (L_3) direction are uniform for all three cases. The Courant number (CFL) for all cases is set as 0.5 where $CFL = \max(u_i \cdot \Delta t/\Delta x_i), i = 1, 2, 3$ to represent the components acting along the three axes in the coordinate system.

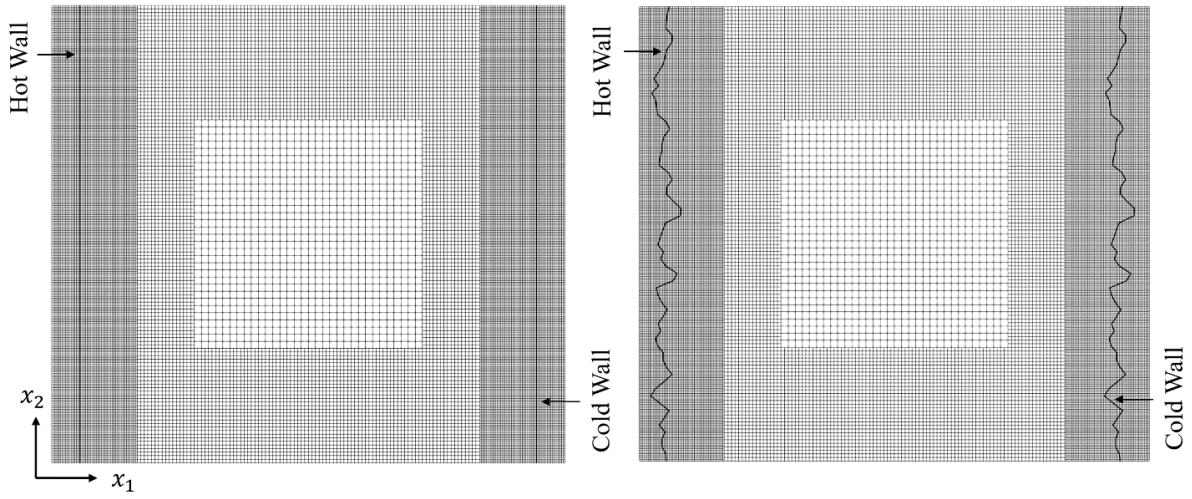

Figure 4.3. Numerical grids distributions of smooth (a) and rough (b) cases at $x_3 = 0.5$ plane.

Table 4.1 shows the average Nusselt numbers across the x_2-direction and the maximum values of the local Nusselt numbers on the hot sidewalls across the height at $x_3/L_3 = 0.5$ plane; these numbers can be obtained using Equation (4.1) and (4.2). The average Nusselt number over entire hot sidewall is calculated through Equation (4.3). The maximum nondimensional vertical velocity at the center of the hot sidewall across the nondimensional width of the cavity (x_1/L_1) is also presented in the table. The nondimensional velocity is defined as $u_i^* = u_i/\sqrt{g\beta_0 \Delta T L_2}$.

$$\overline{Nu} = \frac{1}{L_2}\int_0^{L_2} Nu_l dx_2 \tag{4.1}$$

$$Nu_l = \frac{L_2}{k_0(T_h - T_c)} k(T) \frac{\partial T}{\partial x_1} \tag{4.2}$$

$$\overline{Nu}_{overall} = \frac{1}{A} \int_0^A Nu_l dA \tag{4.3}$$

where $k_0 = k(T_0)$ and $A = L_2 \cdot L_3$.

Table 4.1. Convergence behaviors of hydrodynamic quantities and Nusselt numbers.

Ra	Ref.	Numerical method	$u_2^*{}_{\max}$ (x_1/L_1)	$\overline{Nu}$
10^6	E Tric[65]	Incompressible	0.258 (0.033)	8.877
	A Xu[66]	Incompressible	0.258 (0.037)	8.881
	Present	Compressible (10 K)	0.260 (0.039)	8.854
	Present	Compressible (50 K)	0.259 (0.041)	8.874
	Present	Compressible (120 K)	0.264 (0.043)	8.787

The average Nusselt numbers of the three cases with various temperature differences from Table 4.1 show good agreement with the results from previous studies at the *Ra* of 10^6. The maximum deviation is 1.06%, which is the error between the case with the temperature difference of 120 K and the results of A Xu [66]. Figure 4.4 presents the local Nusselt number distributions at the middle depth on the hot sidewall. For the compressible solver, it is evident that as ΔT increases, the pattern of the local *Nu* numbers on the hot wall becomes steeper, i.e., the maximum value of the local *Nu* increases, but the cases with larger ΔT values will have smaller local *Nu* magnitudes in the $x_2/L_2 > 0.3$ region. Between the case with the temperature difference of 120 K and the results of Kuyper et al. [67], the maximum local Nusselt numbers reach their largest deviation of 6.233%. For the vertical velocity, Table 4.1 indicates that as the temperature difference increases, the location of the maximum vertical velocity moves away from the hot sidewalls. This phenomenon where the distribution of the local Nusselt number changes with the temperature difference was also reported in [68] and it was attributed to the temperature dependences of the fluid properties, as shown in Equation (2.5) and (2.6). In summary, a temperature difference between two heated sidewalls will change the local Nusselt number distribution but will have no effect on the average Nusselt number for a Rayleigh

number of 10^6. Therefore, it becomes necessary to consider adopting a compressible solver when local region heat transfer is the research target.

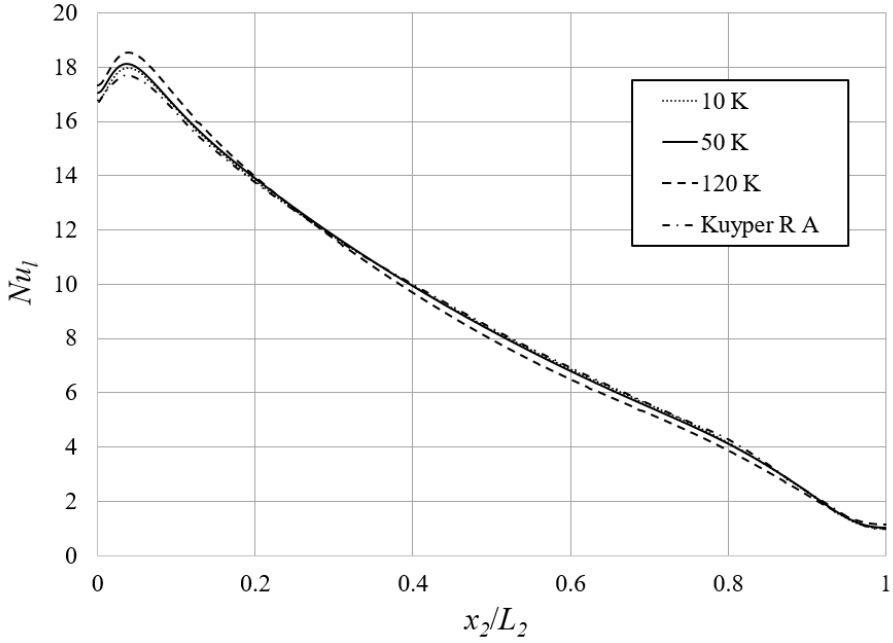

Figure 4.4. Local Nusselt numbers of smooth cases with various temperature differences.

4.2.2 Grid Sensitivity for the Enclosure with Rough Sidewalls

Due to the complex 3D random roughness, the Immersed-boundary method which is mentioned in section 2.3 requires suitable girds to capture the geometric features of the roughness. Meanwhile, for the simulation of the fluid among the roughness elements, an appropriate mesh resolution is necessary. Therefore, in this part, the cavity with rough sidewalls is filled by numerical grids with 3 different resolutions shown in Table 4.2. The mesh resolutions of 128 and 512 are respectively generated by coarsening or refining the grids based on the resolution of 256, shown in Figure 4.3 (b). For convenience, we use grid 128, grid 256 and grid 512 to represent these three mesh resolutions. Table 4.2 shows the average Nusselt numbers over the entire hot sidewall from these 3 different grid strategies. After a comparison between the results of grid 256 and grid 512, the average Nusselt numbers are almost same and the difference is only 0.023%. However, the difference between grid 512 and grid 128 is 10.942%. Further, Figure 4.5 shows the nondimensional temperature distributions across the horizontal centerline of the cavities' midplane ($x_2/L_2 = 0.5$ line at $x_3/L_3 = 0.5$ plane). The profiles show that the temperature distributions of grid 256 and gird 512 almost overlapped near the

hot sidewall, but due to the insufficient resolution, grid 128 shows a different profile of temperature from the other two mesh resolutions.

According to the arrangement of roughness elements in current study, for the resolution of grid 256, there are at least 4 grids along x_2 or x_3-directions for one peak or one valley on the rough surface, but for the resolution of grid 128, this number is only 2 for one peak or one valley. Thus, all subsequent results in the following section are based on the mesh resolution of grid 256.

Table 4.2. Values of average *Nu* for grid sensitivity study.

Mesh resolution	$\overline{Nu}_{overall}$	Difference (%)
512	8.719	-
256	8.717	0.023
128	7.765	10.942

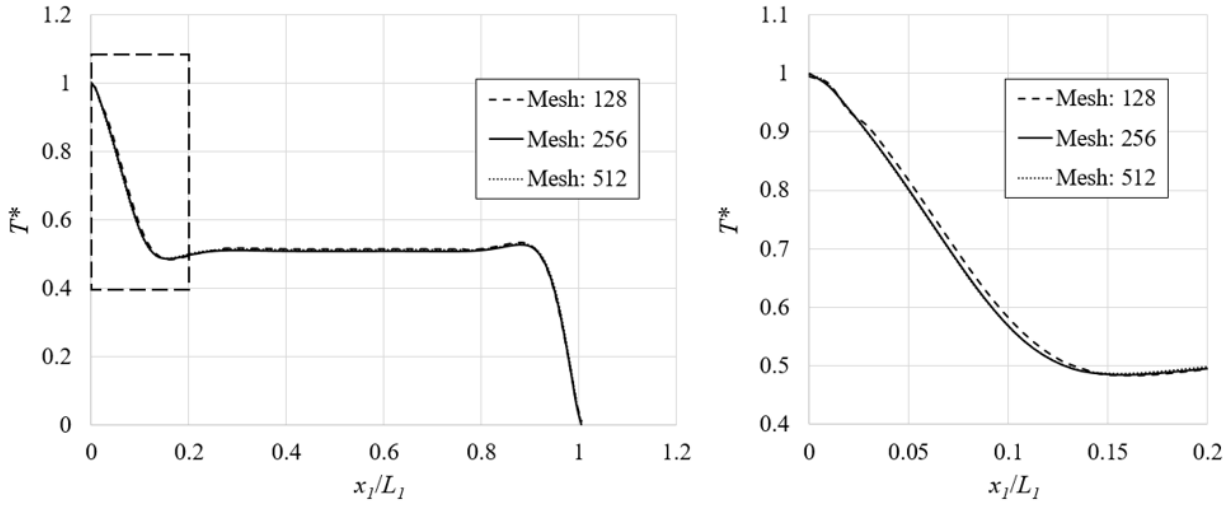

Figure 4.5. Nondimensional temperature profiles.

4.2.3 Influence of Roughness on Heat Transfer

Figure 4.6 shows the local Nusselt number distributions on the hot sidewalls of the smooth and rough cavity cases. For both the smooth case and the rough case, the local Nusselt numbers show a trend of being higher in the upstream region and lower in the downstream region. Because of the existence of the peaks and valleys on the sidewalls, the local Nusselt number

distribution on the rough surface shows good agreement with the distribution of the roughness elements and the local Nusselt numbers on the peaks are larger than those in the valleys. Table 4.3 shows the average Nusselt numbers over the entire hot sidewall and the maximum values of the local Nusselt numbers for the two cases, where the symbols of + and – represent that compared with the results of the smooth case, the increase or decrease of the investigated values due to the rough sidewalls respectively. In Table 4.3, the largest local Nusselt number in the rough cavity case is much larger than that in the smooth case; however, in contrast, the average Nusselt number of the rough case is slightly smaller than that in the smooth case by 1.769%.

Table 4.4 presents the local average Nusselt numbers of the two cases above in the upstream and downstream regions. Here, the local average Nusselt number is considered to be the integral of the Nusselt number on a local part of the heated sidewall, as defined in Equation (4.4):

$$\overline{Nu}_l = \frac{1}{A_l}\int_0^{A_l} Nu_l dA \tag{4.4}$$

where the subscript *l* indicates a specific local part of the heated sidewall.

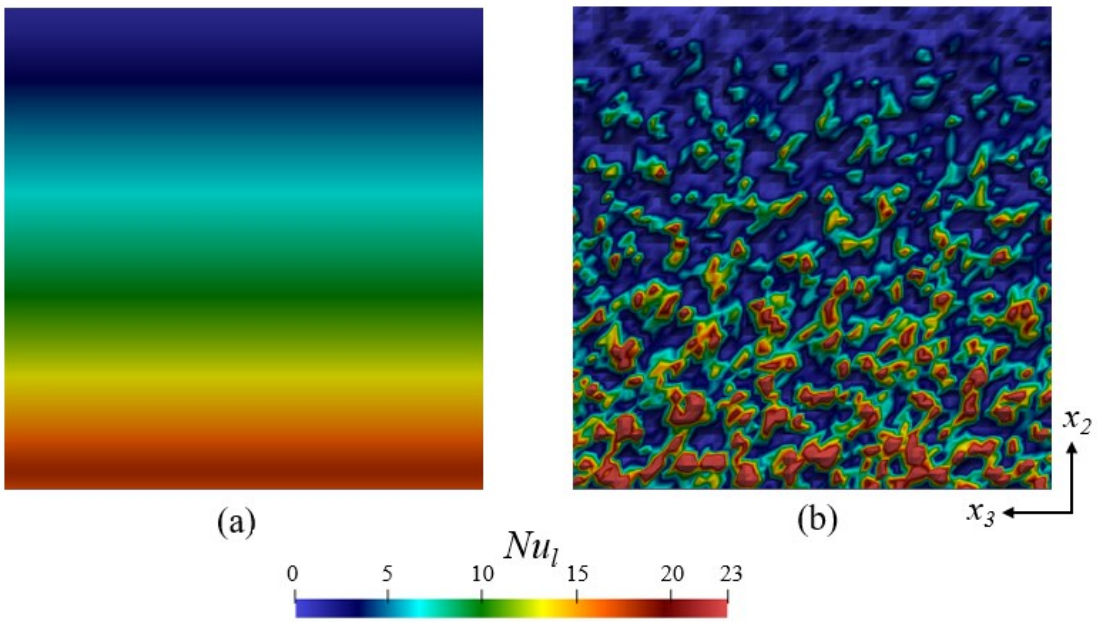

Figure 4.6. Distributions of the local *Nu* values of the (a) smooth and (b) rough cases on the hot walls.

Table 4.3. Maximum values of the local Nusselt numbers and the average Nusselt numbers for the smooth and rough cases.

	smooth	rough	Difference (%)
Nu_{lmax}	18.134	60.207	+232.012
$\overline{Nu}_{overall}$	8.874	8.717	-1.769

Table 4.4. Local average Nusselt numbers in the upstream and downstream regions.

	Smooth	Rough	Difference (%)
Upstream (x_2/L_2 = 0 to 0.1)	17.613	18.622	+5.729
Downstream (x_2/L_2 = 0.75 to 1)	2.822	2.743	-2.799

When compared with the smooth case, the local average Nusselt number in the upstream region in the rough case is higher, but in the downstream region, the local average Nusselt number in the rough case is smaller than that in the smooth case. To explain this phenomenon in greater depth, the temperature distribution on a slice at a quarter of the depth of the cavity is shown in Figure 4.7, where the nondimensional temperature is calculated using the following equation: $T^* = (T - T_c)/(T_h - T_c)$. In the upstream region, the peaks will reduce the thermal boundary layer thickness, while the valleys can make the thermal boundary layer thicker, which means that the thermal boundary layer will undergo drastic changes in thickness within this region. However, as the thermal boundary layer develops, the thickness will inevitably increase, and then the effects of the roughness elements on the thermal boundary layer will decrease. From Figure 4.7 (c) and (d), the isothermal surfaces are distorted by the roughness elements near the rough sidewall, but in the core region of the cavities, the temperature stratifications are almost identical for smooth and rough cases.

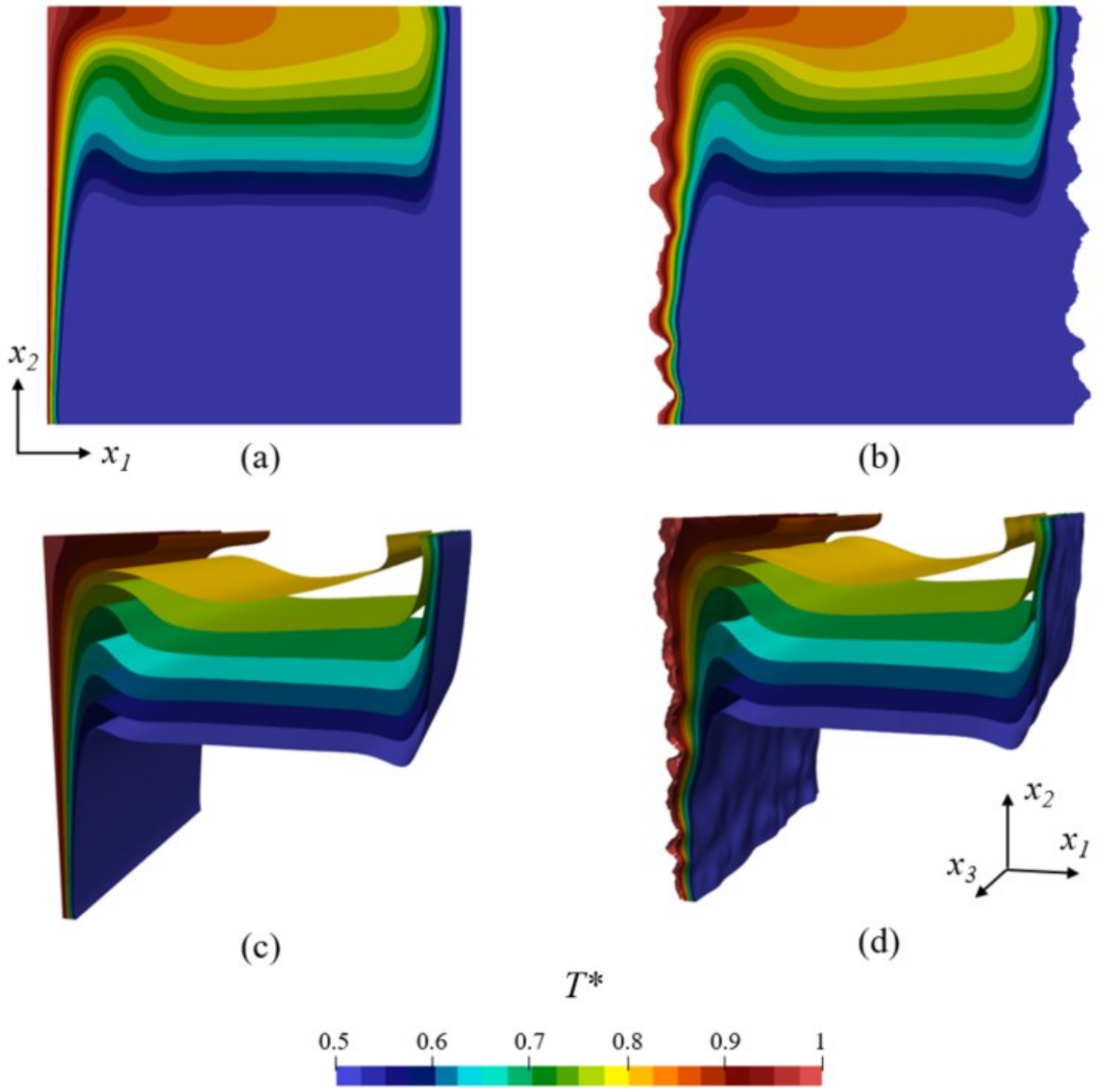

Figure 4.7. Temperature distributions of smooth and rough cases: (a, b) slices at x_3/L_3=0.25 plane (c, d) isothermal surface in half cavity from x_3/L_3=0 to 0.5.

Figure 4.8 (a) and (b) show the nondimensional velocity magnitudes of the two cases on three different planes ($x_1/L_1 = 0.005$, $x_2/L_2 = 0.5$ and $x_3/L_3 = 0.25$) respectively. From this figure, when the flow approaches the peaks on the rough surface, there is a slight acceleration in the magnitude of the velocity when compared with the smooth case, but after the peak has been crossed, the ensuing valley will cause the fluid velocity to decelerate sharply. Unlike the influence of the rough surface on the thermal boundary layer, the influence of the rough surface on the magnitude of the velocity in the downstream region is obvious. This can therefore be considered to be one explanation as to why the local Nusselt number distribution presents the

tendency where, in the case with the rough heated sidewalls, the local Nusselt number is higher than that in the smooth case in the vicinity of the peaks in the upstream region, while in the downstream region, the local average Nusselt number is smaller than that in the smooth case.

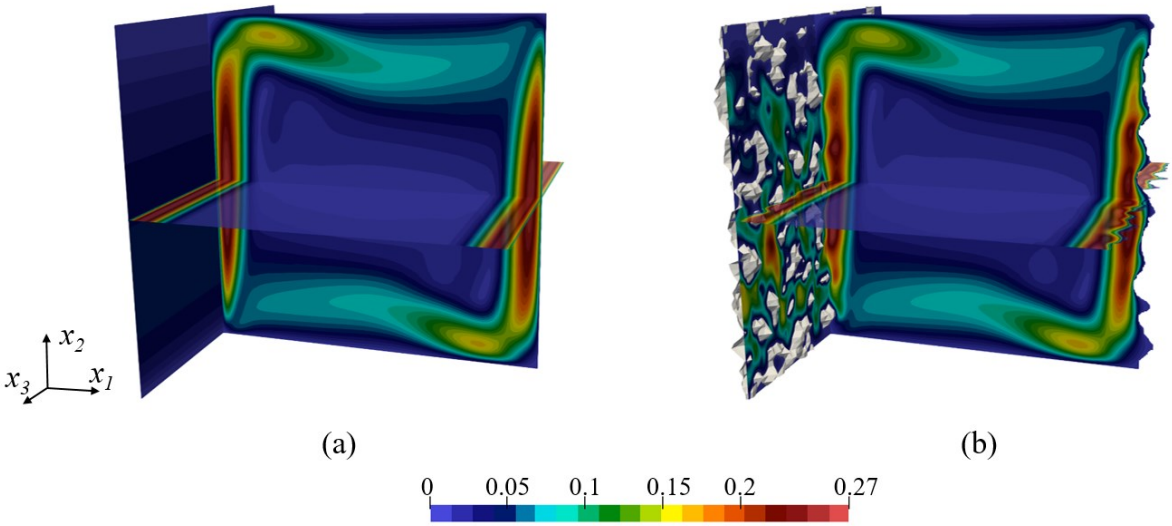

Figure 4.8. Nondimensional velocity magnitudes (where (a) and (b) show the smooth and rough cases, respectively).

Figure 4.9 shows the contours of the nondimensional velocity magnitude of both smooth and rough cases near the hot sidewall at four different x_1-x_2 planes (x_3/L_3 = 0.125, 0.25, 0.375 and 0.5), where the black curves are the profiles of hot sidewalls at these planes. From the figure, the velocity magnitudes of the flow field in the vicinity of the rough wall are smaller than smooth case generally, and only part of the fluid will be accelerated due to the roughness. In the region where the shape of roughness elements does not change drastically, the roughness plays a role more in slowing down the velocity of adjacent fluid rather than accelerating it.

Figure 4.10 (a) and (b) show the velocity vector fields in the half region located close to the hot sidewall at the same location used in Figure 4.9 (a) and (b). The figure containing the velocity vectors shows no evident fluid circulation to be found in the area between the two roughness elements on the x_1-x_2 plane at $Ra = 10^6$. In addition, the eddies that occur near the core regions of the two cavities do not show particularly notable differences.

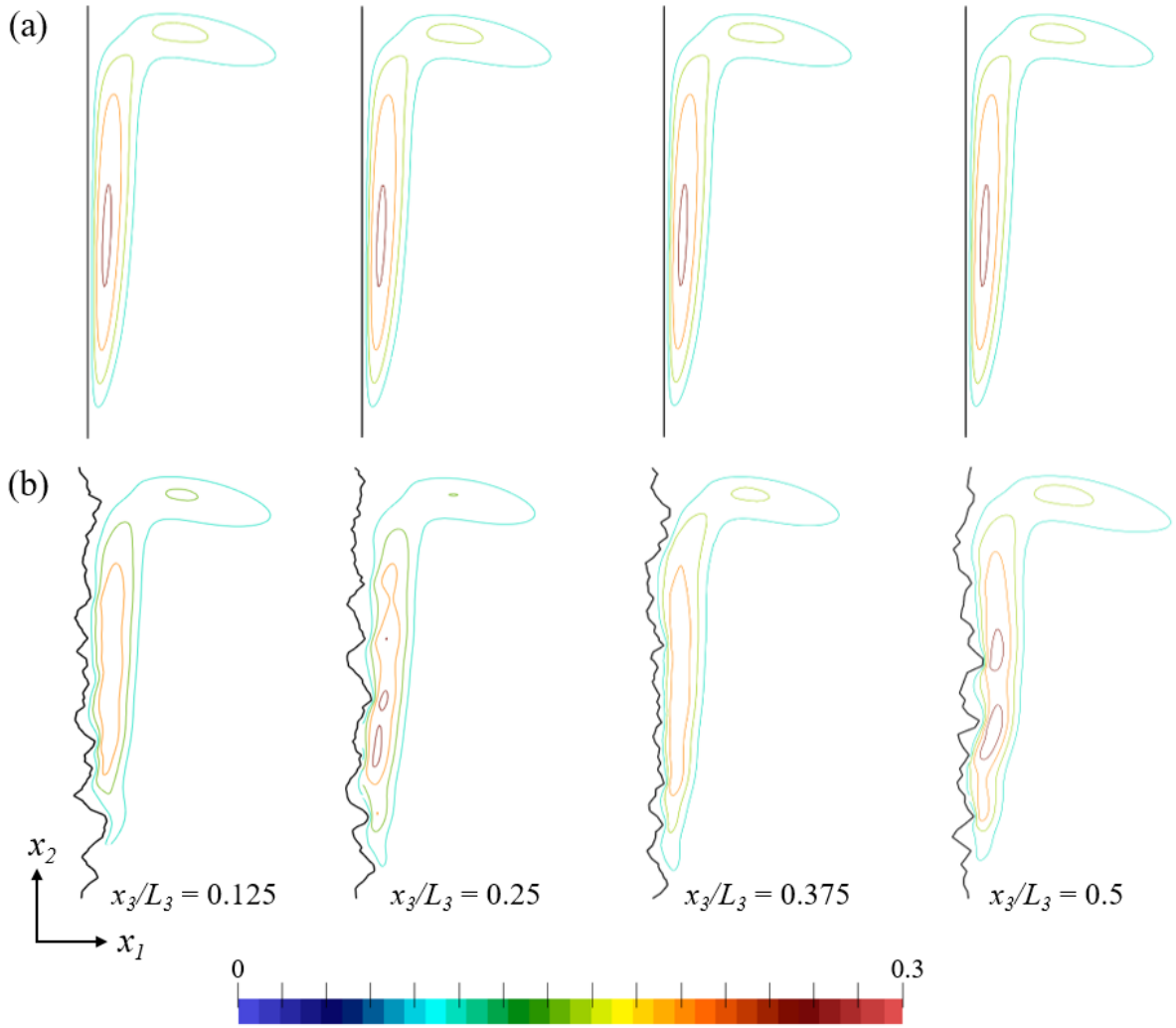

Figure 4.9. Contours of Nondimensional velocity magnitude of smooth (a) and rough (b) cases at different x_1-x_2 planes.

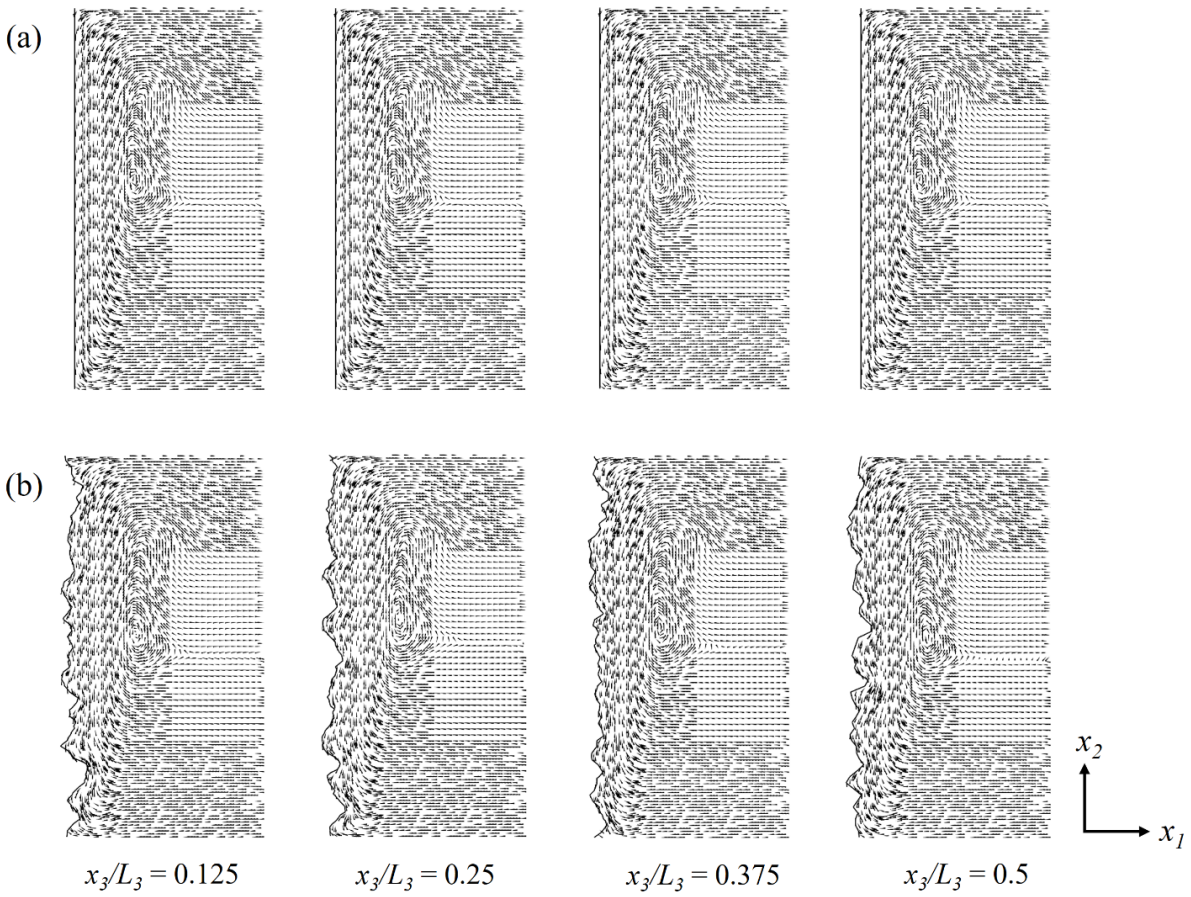

Figure 4.10. Velocity vector fields of smooth (a) and rough (b) cases at different x_1-x_2 planes.

In Figure 4.11, the components of the nondimensional temperature gradients in the x_1-direction have been measured in the cavities with both rough and smooth sidewalls at two measurement locations. These two locations are two different lines parallel to the x_2-direction($x_3/L_3 = 0.55$ line and $x_3/L_3 = 0.8$ line) at $x_1/L_1 = 0.05$ plane starting from the mean plane of the hot rough sidewall. The black curves shown in Figure 4.11 are the profiles of the hot rough surfaces at x_1-x_2 planes where two measurement locations lie respectively. The figure shows that in the upstream regions, the temperature gradient fluctuates drastically and this trend follows the distribution of the roughness elements perfectly, which means that higher peaks will bring increased heat transfer. However, this dominance of the roughness decreases in the end region, particularly in the downstream region, and after the nondimensional height exceeds 0.8, the patterns from the two cases almost overlap. In Figure 4.12, at the center of the adiabatic surface and across the heights of the cavities, the temperatures in both the rough and smooth cases have been measured. The temperature curves show very good agreement, thus

indicating that the random artificial roughness cannot influence the heat transfer that occurs in the core region of the square cavity.

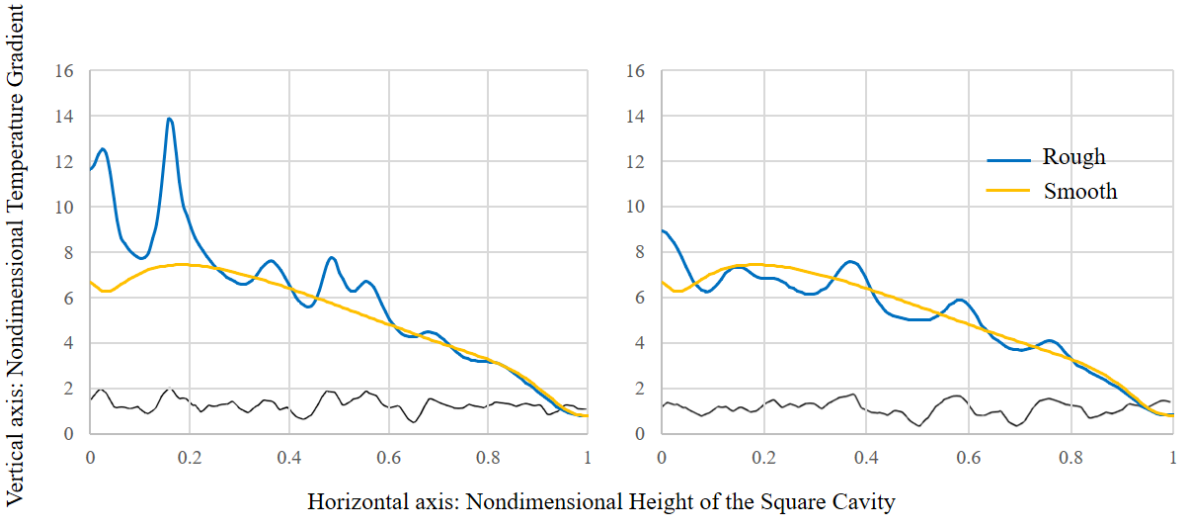

Figure 4.11. Nondimensional temperature gradients across the height of the cavity at two different measurement locations (black curves: profiles of the rough surface at the two measurement locations).

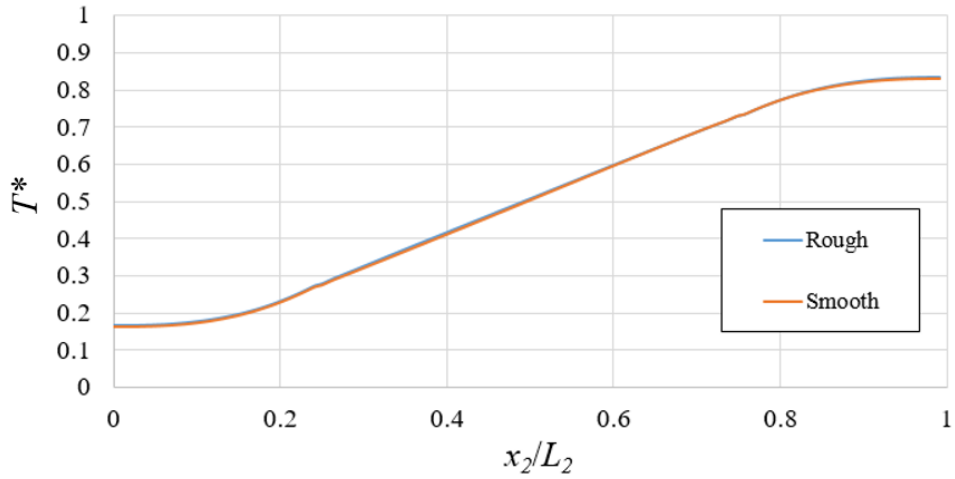

Figure 4.12. Nondimensional temperatures at the center of the adiabatic surface across the cavity height.

Figure 4.13 and Figure 4.14 show the effects of the surface roughness on the velocity component in the x_3-direction. The slices in Figure 4.13 are located at different x_1-x_2 planes. The magnitudes of this velocity component shows a trend where the initial magnitude is very

small in the upstream region and then increases to reach a maximum in the middle region; however, in the downstream region, deceleration occurs. Furthermore, the effect of the rough surface cannot reach the core region of the cavity. The slice shown in Figure 4.14 is located at a position of 0.5% of the cavity width from the mean plane of the rough surface. In this figure, the changes in the colors near the roughness elements and the speed vectors demonstrate that the geometry of the 3D random roughness structure gives the fluid the possibility of bypassing the roughness elements and no evident eddies were found. However, in two-dimensional cavity flow with homogeneous roughness elements on the cavity sidewalls[36][37], the fluid will become trapped more easily between two adjacent roughness elements, and this represents a major cause of the reduction in the heat transfer.

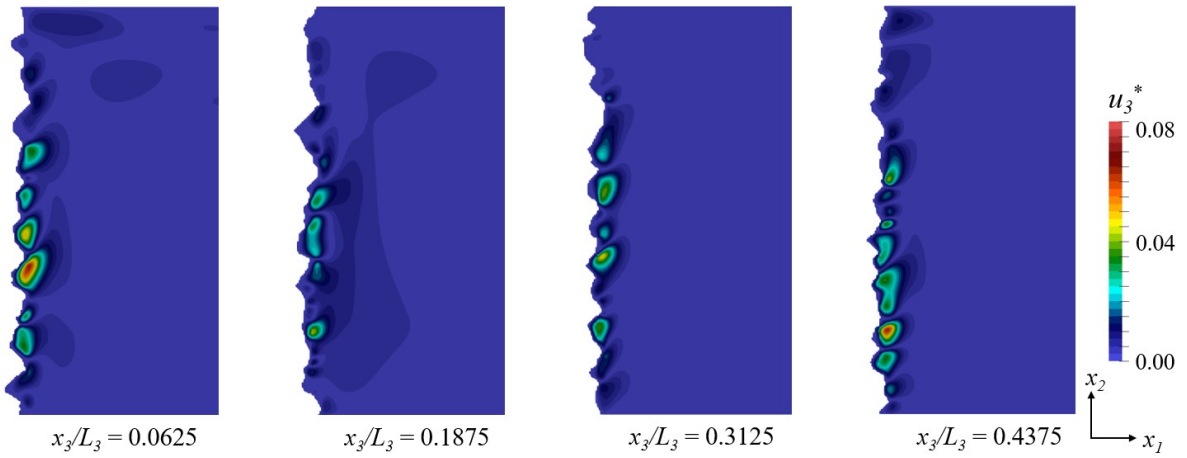

Figure 4.13. Magnitudes of the velocity component in the x_3 direction.

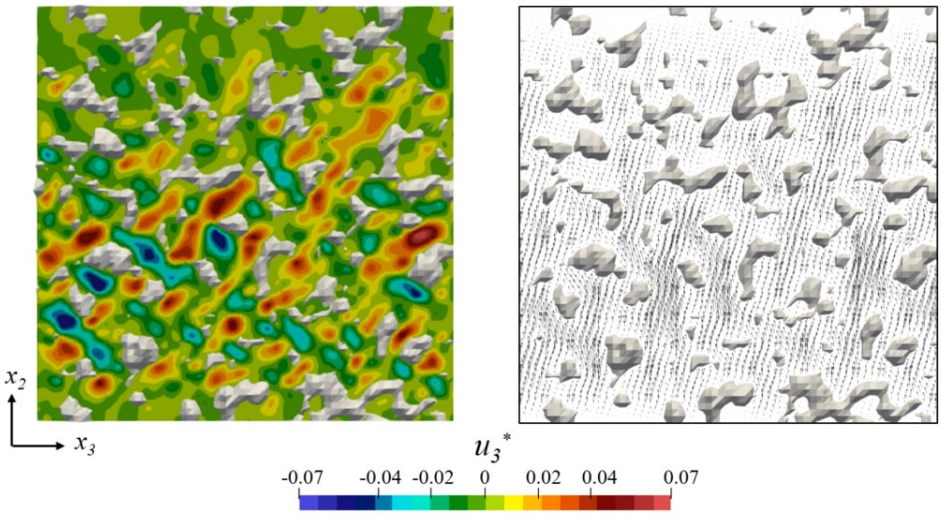

Figure 4.14. Flow field among the roughness elements of the hot sidewall.

CHAPTER 5. INVESTIGATION OF DIFFERENT IRREGULAR ROUGHNESS EFFECTS ON LAMINAR NATURAL CONVECTION FLOWS IN CUBOID CAVITY

5.1 Physical model

The enclosed cavity shown in Figure 5.1 has been chosen as the physical model in this chapter. The aspect ratios of the cavity are $L_2/L_1 = 4$, $L_2/L_3 = 2$. On both sidewalls (planes at x_1=0 and L_1), the boundary conditions of isothermal and non-slip have been implemented, where the higher temperature is indicated as T_H, and the lower temperature is T_C. The temperature difference between these two sidewalls is a constant of 50K. For all cases involved in this chapter, the cavity size and the temperature difference are kept invariant and *Ra* is equal to 10^6 based on the height of the cavity. The adiabatic and non-slip boundary conditions are imposed on the top and bottom (planes at x_2=0 and L_2) of the cavity. Because of the 3D characteristic of the irregular random roughness, it is hard to adopt periodic boundary condition at both depth-direction boundaries, thus to reduce the boundary effects on the flow fields near the rough surfaces, a slip boundary condition is applied on the borders at x_3=0 and L_3. Inside the cavity, the physical properties of the working fluid are based on the initial temperature $T_0 = (T_H + T_C)/2$. And for all cavity flows, the working fluid is air with a Prandtl number of 0.72 and the initial pressure is 101300 Pa.

Same with Chapter 4, the generation method of the irregular roughness introduced in Chapter 3 is applied. In this chapter, 4 different irregular rough surfaces have been generated according to 4 given *PSD* curves. These 4 rough surfaces have same root-mean square ($\sigma = 1.5\%L_1$) of roughness element height, and same Hurst exponent ($H = 0.8$), but different roll-off wavenumbers (q_R). That means, due to the constant size of cavities and *Ra*, this chapter focuses on the influence of roll-off wavenumber on the natural convection flows in the cavity with rough sidewalls. Under the condition of constant σ and H, q_R dominates the "power" of the roughness waves of different wavelengths. Larger q_R represents the geometric features of roughness elements with smaller wavelengths will be more conspicuous. In layman's term, the surface looks rougher. To intuitively express the roll-off wavenumber, the nondimensional wavenumber is defined as following:

$$q^* = \frac{L_2 q}{2\pi} \tag{5.1}$$

In this way, through q_R^* we can clearly calculate the number of the roughness waves with the wavelength of $2\pi/q_R$ that the height of the cavity can hold. In this chapter, $q_R^* = 9.5, 16, 24, 32$. It should be noted, $q_R^* = 9.5$ is a typical roll-off wavenumber of an asphalt road surface[60]. Figure 5.2 shows 4 irregular rough surfaces based on these 4 wavenumbers. The probability density functions (*PDF*) of the heights of the 4 rough surfaces are expressed in Figure 5.3. Obviously, the height distributions of the surfaces abide by the Gaussian distribution with averages of 0 and the same root-mean square σ.

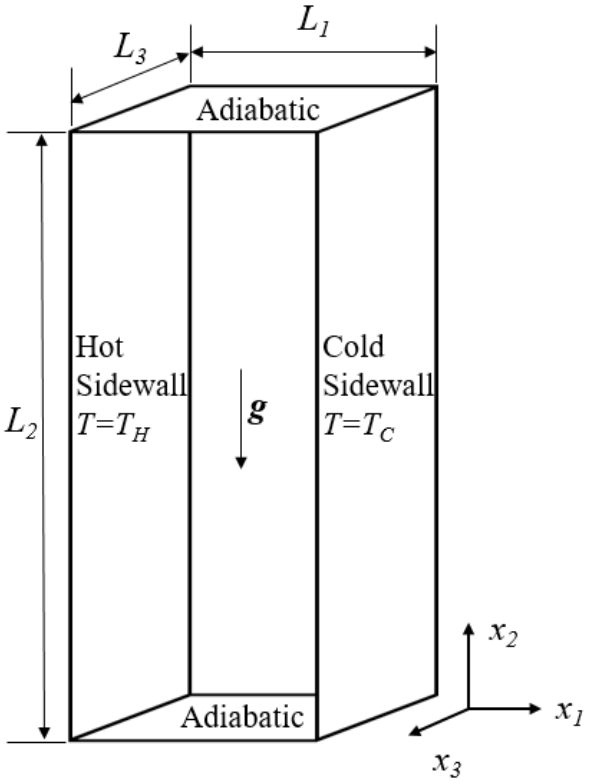

Figure 5.1. Illustration of physical and computational geometry.

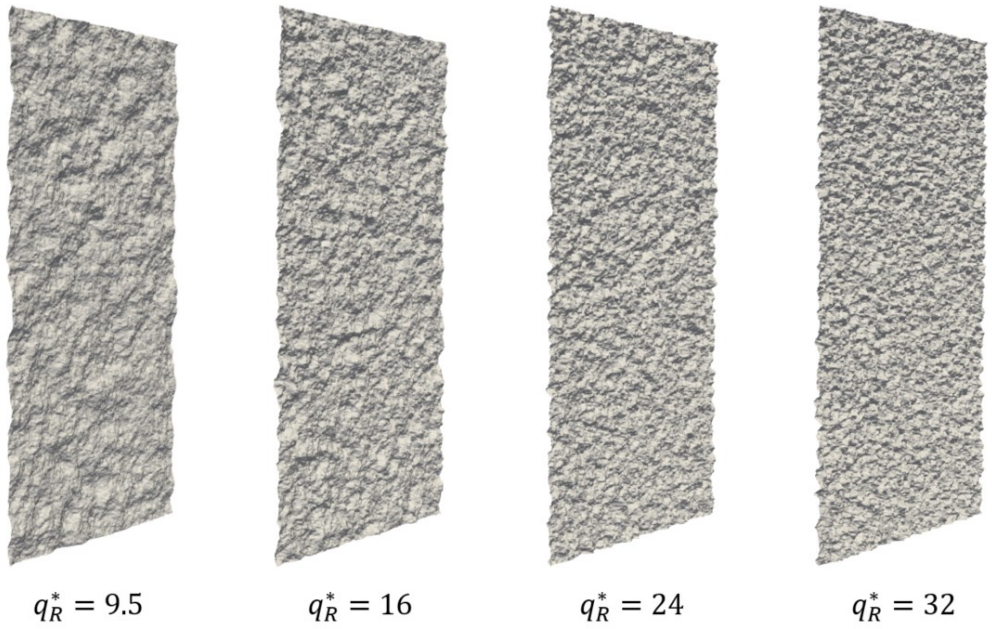

Figure 5.2. Different irregular rough surfaces.

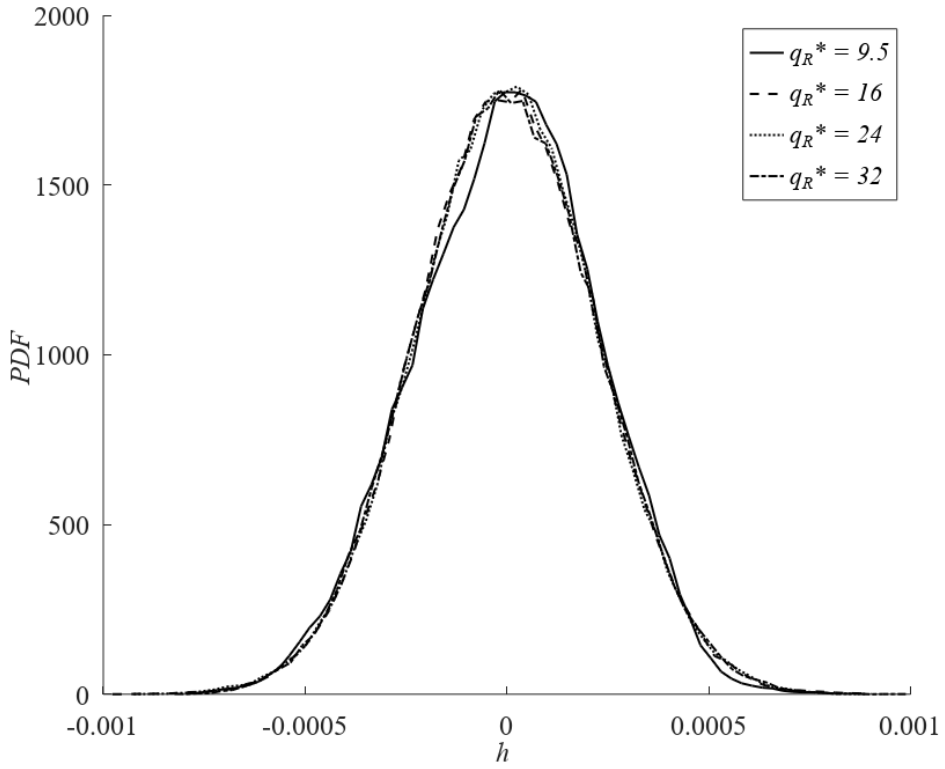

Figure 5.3. The height probability density functions of the surface roughness.

5.2 Numerical setting and validation

Figure 5.4 shows the distribution of numerical girds in present chapter. The uniform spacing of the girds is suitable for discribing the local roughness elements especially under the application of Immersed-boundary method. From the figure, the finest meshes are arranged in the vicinity of the rough sidewalls, and the meshes in the core region of the cavity will be coarser, and the stretch rate of the grids is kept at 2. The number of finest grids along the height direction is decided as 2048 to capture the information of roughness as much as possible and avoid an unaffordable grid number. The simulations of all the cases in this chapter are based on the same numerical grid distribution and the total grid numbers are around 260 million.

5.2.1 Code validation

To validate the grid distribution, a similar simulation with Xu et al[66] has been conducted. In this validation simulation, a cubic cavity with all six non-slip boundaries has been considered to keep consistent with the benchmark, and the comparisons of the results have been shown in Table 5.1. Here, the average Nusselt number $\overline{Nu}$ is calculated on the hot sidewall at $x_3/L_3 = 0.5$ plane, and the nondimensional velocity u_2^* is measured at the line of $x_2/L_2 = 0.5$ on the mid-depth plane. The average *Nu* and hydrodynamic quantities show good agreement with the achievements of previous researchers.

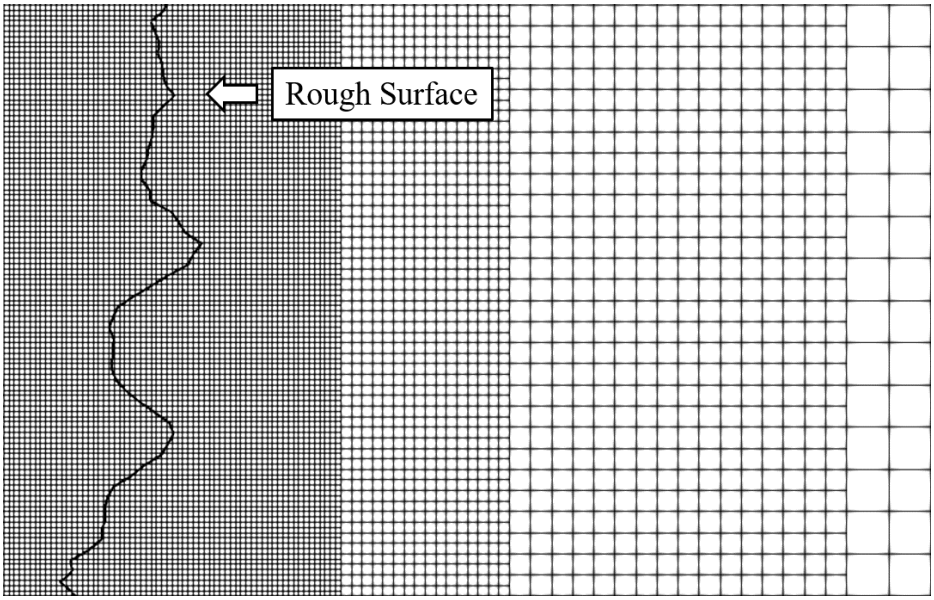

Figure 5.4. Illustration of numberical grids distribution.

Table 5.1. Comparisons of Nusselt numbers and hydrodynamic quantities.

Ra	Ref.	$\overline{Nu}_{overall}$	$\overline{Nu}$	$u^*_{2_{max}}$ (x_1/L_1)
10^6	A Xu[66]	8.643	8.881	0.258 (0.037)
	Present	8.698	8.872	0.254 (0.039)

5.2.2 Grid convergence study

In this section, the convergence studies of the numerical grid have been given. As mentioned in Chapter 3, the rough surface with a larger roll-off wavenumber (q_R) contains the geometric details of roughness elements with smaller wavelengths, so the roughness with higher q_R is more sensitive to the resolution of numerical grids. Thus, we chose the rough surface with q_R^* of 32 as the research object to test the grid convergence. On the other hand, the rough surfaces we generated in current study are isotropic, therefore on the x_2-x_3 plane, the distribution of roughness elements along the x_2-direction includes roughness elements of all wavelengths theoretically. To reduce the mesh number, and consider the 3D roughness elements which are able to increase the velocity in the x_3-direction of the nearby flow fields, we extracted a strip of the rough surface with a width of one-sixteenth of L_3 along the x_2-direction at the middle depth of the cavity. Then a quasi-2D cavity with 2 differently heated rough striped sidewalls has been generated with the same boundary condition shown in section 2.1. This 2D cavity has the same height and width as the original 3D cavity. On the hot rough striped surface, the quasi-2D Nusselt number is selected to present the mesh-independent solutions. This quasi-2D Nu can be calculated according to the following equation:

$$\overline{Nu}_{2D} = \frac{1}{A_{strip}} \int Nu_l dA$$

where, A_{strip} indicates the area of the rough strip.

The results are shown in Figure 5.5. The mesh resolutions in the figure are controlled by the number of the finest mesh along the x_2-direction and scaled by the height of the cavity.

From the figure, as the resolution increases, the quasi-2D *Nu* is observed close to the asymptotic values. Hence, we used 1/2048 mesh resolution for the following main simulations.

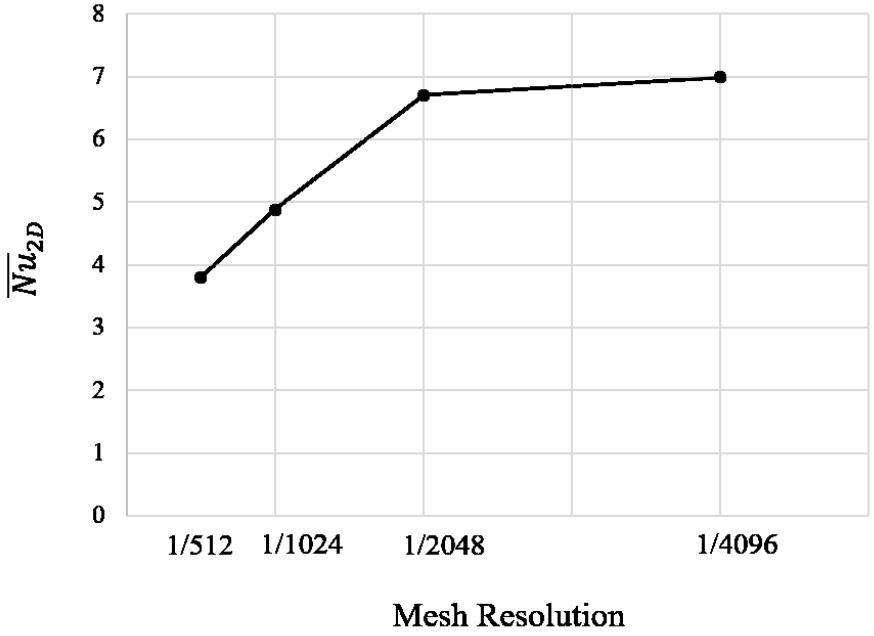

Figure. 5.5. Quasi-2D *Nu* with different mesh resolutions

5.3 Results and discussion

In this section, the average and local Nusselt numbers have been chosen to assess the effect of rough sidewall on the heat transfer performance in the cavity flows. Because the temperature gradient on the wall should be considered along the normal direction of the heated wall, the calculation method of the Nusselt number should be adjusted from Equation (4.2) into Equation (5.2), where ***n*** represents the local normal directions of the measured surface. And the averaged Nusselt number can be still calculated through Equation (4.3). It should be noted, $\overline{Nu}_{overall}$ is based on the total heat transfer through the solid surface, thus the calculation of this number includes the variation of surface area because of roughness elements. Thus, it is meaningful to use $\overline{Nu}_{overall}$ as a direct measurement of the influence of roughened surfaces on the overall heat transfer performance.

$$Nu_l = \frac{L_2}{k_0(T_H - T_C)} k(T) \frac{\partial T}{\partial n} \tag{5.2}$$

Table 5.2 presents the average Nusselt numbers of all 5 cases, of which case with smooth sidewalls is the benchmark to evaluate the influence of the rough surfaces on the heat transfer. The difference is computed by $Difference = (Rough - Smooth)/Smooth \times 100\%$. Thus, from the table, the differences show that the roughness has an appreciable negative effect on the heat transfer performance of the natural convection flows in a cavity, and shown in Figure 5.6, as the roll-off wavenumber q_R^* increases, the average *Nu* decreases. Figure 5.7 shows the augments of the surface area based on different q_R^*, where A_S indicates the area of the smooth sidewall which is equal to $L_2 \cdot L_3$. It is obvious the area of the sidewall will increase following the increasing q_R^*, but the increase in the area did not provide an increase in $\overline{Nu}_{overall}$. From section 5.1, the changes in the area come with the changes in the geometry of roughness elements and, doubtless, changes in roughness elements will change the local *Nu* on the solid surfaces. Therefore, it is better to consider the effects of surface area and geometry of roughness elements on the heat transfer comprehensively and locally.

To reveal the influence of the roughness on the local heat transfer performance, the local *Nu* distributions on the different rough surfaces are illustrated in Figure 5.8. For all 4 rough cases, the distributions of local *Nu* have the tendency of high in the upstream region and low in the downstream region. This is consistent with the local *Nu* on the smooth sidewall. But, due to the existence of roughness elements, the fluctuations on the surfaces will vary the heat transfer locally. Generally speaking, roughness peaks will increase the local *Nu*, and the roughness valleys will have opposite effects. As roll-off wavenumber increases, the average wavelength of the roughness elements will decrease. Reflected in the shapes of roughness elements, these elements will be steeper and jaggeder. Thus, the patterns of locally high *Nu* progressively become more discrete and no longer connect together as q_R^* changes from 9.5 to 32. Table 5.3 presents the maximums of local *Nu* on different rough surfaces. There is no doubt that the roughness peaks will extraordinarily amplify the local *Nu*, and this augment is more conspicuous on those steeper roughness peaks. According to the previous researches[69], the roughness peaks are able to accelerate the flow fields nearby and thicken the local thermal boundary layer. Further, in present research, steeper roughness peaks will have greater impacts on the local temperature and velocity fields. This results in a high local *Nu* and a drastic change rate of local *Nu*. Therefore, the figure of local *Nu* at $q_R^* = 32$ shows the feature of extremely high Nu_l but discrete distribution of high Nu_l regions. Although the total surface area of the rough sidewall will increase as q_R^* increases, from Figure 5.8, the regions with higher Nu_l

gradually cluster towards the peaks, and in other regions, the Nu_l will decrease. As a result, the increased surface area does not provide better overall heat transfer performance.

Considering the different influences of roughness peaks and valleys on the surface heat transfer, we have separated a rough surface into the top and bottom parts based on its mean plane and the respective contributions to heat transfer of these two parts are measured through the following equations:

$$\overline{Nu}_T = \frac{1}{A}\int_0^{A_T} Nu_l dA_T \tag{5.3}$$

$$\overline{Nu}_B = \frac{1}{A}\int_0^{A_B} Nu_l dA_B \tag{5.4}$$

where A_T and A_B represent the area of the top ($h > 0$) and bottom ($h \leq 0$) parts respectively. Figure 5.9 clearly illustrates the tendencies of $\overline{Nu}_T$ and $\overline{Nu}_B$ following q_R^* and the average Nusselt numbers show different performances. As q_R^* increases, $\overline{Nu}_B$ decreases appreciably, but $\overline{Nu}_T$ does not show a rigorous tendency of decrease and the change of $\overline{Nu}_T$ is much smaller comparatively. From this, we can get a conclusion that the heat transfer on the bottom region of a surface is more sensitive to the change of roll-off wavenumber than it on the top region. One potential explanation for this situation is the different flow fields near the top and bottom regions. The fluid near the top region of one rough surface can be considered into two parts: one is among the roughness elements and will bypass the roughness elements, the other is from the large-scale circulation and will cross over the roughness peaks. Differently, the fluid near the bottom region is among the roughness elements only. The flow fields in the space formed by roughness elements are directly affected by the arrangement of these peaks and valleys. Figure 5.10 shows the velocity magnitude of the fluid among the roughness elements. The measurement location has been chosen at the plane where the distances to the mean plane of the rough hot sidewall are equal to 1.5% of L_l. From these contours, the fluid is able to bypass the roughness elements, and the large space among the roughness elements will give the fluid the possibility to get rid of the boundary layer and achieve a relatively high velocity. However, the roughness elements with short wavelengths will tear this space into small pieces, so the fluid has to overcome more resistance to flow through these obstacles. Thus, as the q_R^* increases, the velocity magnitude of the fluid among the roughness elements decreases. And, the weakened convection will undoubtedly aggravate the heat transfer at the corresponding

locations. Then the effect of increased surface area on heat transfer will be diminished. On the other hand, the flows from the large-scale circulation will be accelerated by the roughness peaks, so the heat transfer through this part of flows will be augmented. Therefore, $\overline{Nu}_T$ and $\overline{Nu}_B$ show different tendencies like Figure 5.9.

Table 5.2. Values of average *Nu* for different cases.

	$\overline{Nu}_{overall}$	Difference (%)
Smooth	12.984	-
$q_R^* = 9.5$	12.545	-3.382
$q_R^* = 16$	11.641	-10.345
$q_R^* = 24$	11.062	-14.800
$q_R^* = 32$	10.579	-18.521

Table 5.3. Maximums of local *Nu* on different surfaces.

Nu_l	Maximum
Smooth	25.208
$q_R^* = 9.5$	77.279
$q_R^* = 16$	87.410
$q_R^* = 24$	97.026
$q_R^* = 32$	115.302

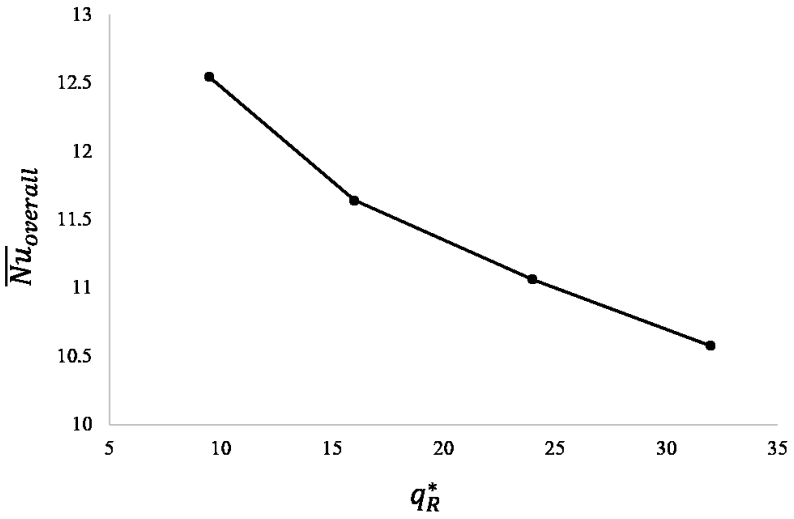

Figure 5.6. Averaged *Nu* with varying q_R^*.

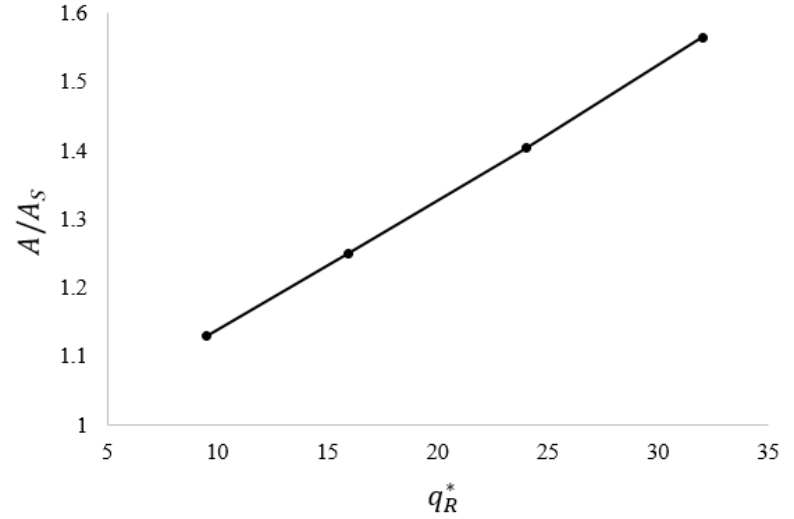

Figure 5.7. Total surface areas of roughened sidewalls with varying q_R^*.

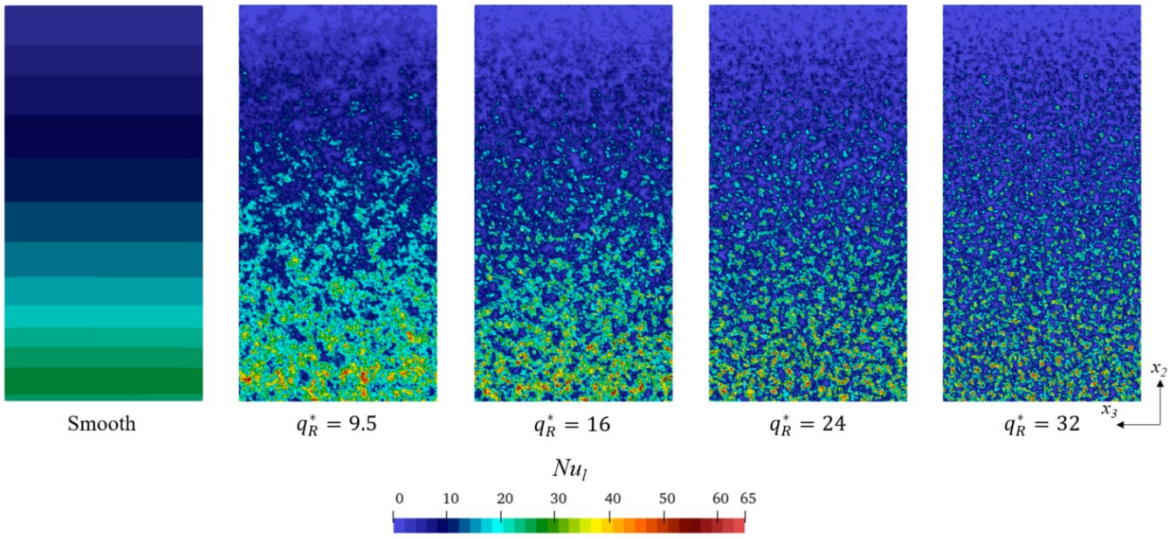

Figure 5.8. Distributions of the local Nu values.

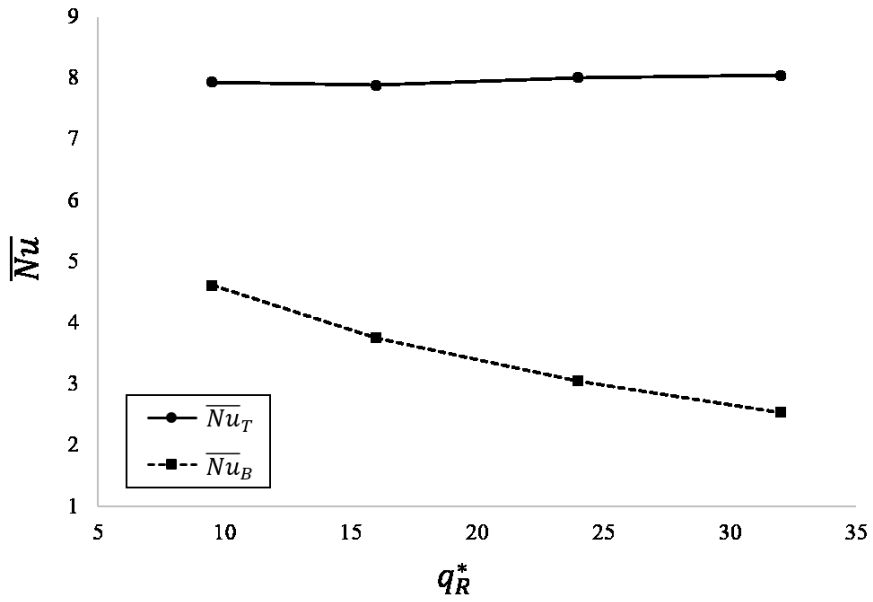

Figure 5.9. Average Nusselt numbers on top and bottom regions of different rough surfaces.

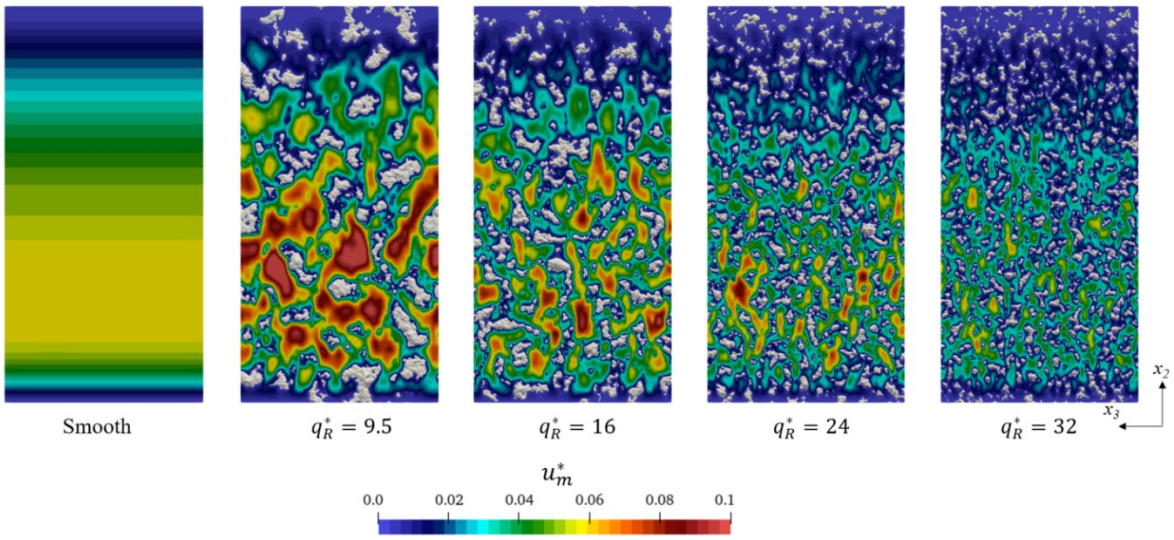

Figure 5.10. Velocity magnitude of the flow field among the roughness elements.

CHAPTER 6. CHAPTER 6. DIRECT NUMERICAL SIMULATION OF TURBULENT NATURAL CONVECTION FLOWS OVER 3D IRREGULAR ROUGH SURFACE

6.1 Physical model

In this chapter, the physical model of cavity is same with Chapter 5 in apsect ratios, initial environment settings and boundary conditions i.e the temperature difference of 2 vertical sidewalls is 50K. But in this chapter, Rayleigh number ($Ra = g\beta_0 \Delta T {L_2}^3 Pr/{\nu_0}^2$) is chosen as 10^{10}, that means this chaper focuses on the turbulent flows in the enclosure cavity. Thus the size of the cavities involved in chapter is much larger than Chapter 5.

According to the results of Chapter 5, the largest q_R^* has the most negative effect on the surface heat transfer. Considering the different flow conditions between laminar and turbulent flows, in Chapter 6, the surface roughness is same as the roughness in Chapter 5 with a nondimensional roll-off wavenumber of 32 but proportionally enlarged to fit the size of the current cavity.

6.2 Results and Discussion

6.2.1 Validation of numerical simulation setup

In order to validate our compressible solver established in chapter 2, we took the previous achievements of F. X. Trias et al.[70] at a Rayleigh number of 1×10^{10} as a reference. The present grid spacing is uniform in the x_3 (depth) direction and near the wall, the grids are uniform in x_1 (width) and x_2 (height) directions. The finest grids are implemented in the vicinity of sidewalls, and coarser grids are adopted in the core region of the cavity, and the stretch rate of the grids is kept at 2. The resolution shown in Figure 6.1 is chosen so that the simulation can deal with the eddies around the Kolmogorov microscale, which is defined as $\eta = (\upsilon^3/\varepsilon_{u'})^{1/4}$, where $\varepsilon_{u'} = \upsilon\overline{(\partial u_i'/\partial x_j)^2}$ [71]. There are 2048 finest grids along the height direction of the cavity, so that near the wall $\Delta x_1 = \Delta x_2 = \Delta x_3 < 0.118\eta$ and in the core region of the cavity, the mesh spacings, $\Delta x_1 = \Delta x_2 = \Delta x_3 < 1.07\eta$.

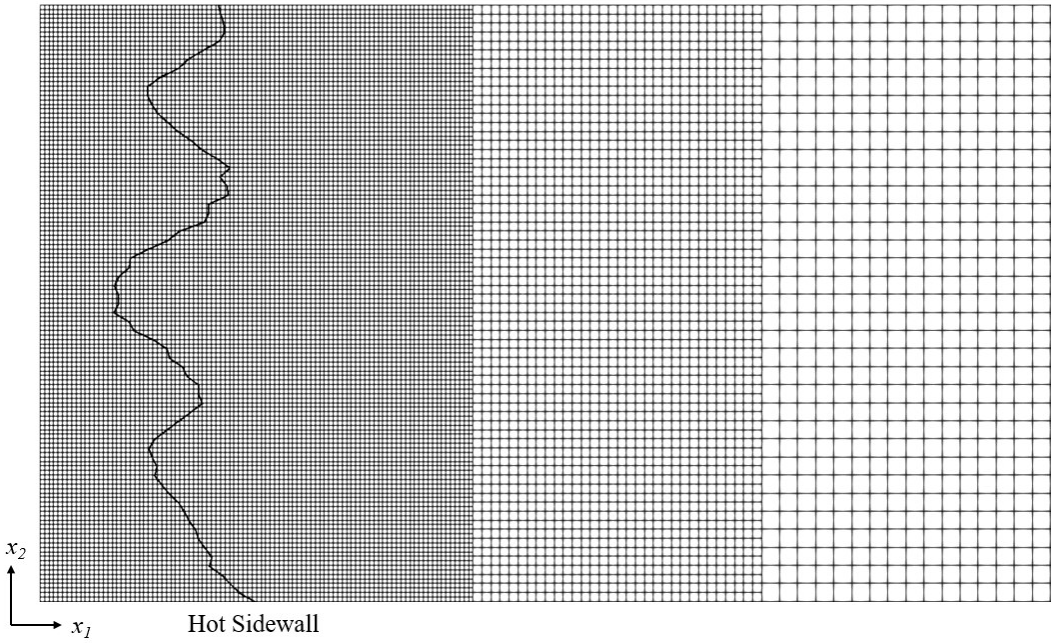

Figure 6.1. Numerical grids distribution.

Table 6.1 shows the comparison of vertical nondimensional velocities and the local Nusselt number on the hot sidewall and the reference length, temperature and velocity used for nondimensional forms are L_2, $\Delta T = T_H - T_C$ and $u_{ref} = \sqrt{g\beta_0 \Delta T L_2}$ respectively. Based on the time-averaged and spanwise-averaged (depth direction) results, the local and average Nusselt numbers can be calculated using Equation (5.2) and (4.1) and the nondimensional vertical velocity u_2^* is measured at the mid-height and across the nondimensional width of the cavity (x_1/L_1). In general, the results show good agreement with the studies of incompressible direct numerical simulation from F Trias[70]. Figure 6.2 presents the distribution of the local Nusselt number across the hot sidewalls. Compared with the incompressible result, our compressible result has a higher local Nusselt number in the upstream region but in the region of $0.2 < x_2/L_2 < 0.7$ the temperature gradient will be slightly smaller than the incompressible result. Then, in the higher region, $x_2/L_2 > 0.8$, the increase of local Nu in the incompressible result is hard to be observed from the compressible result. This phenomenon was also found in other cases with relatively low Rayleigh numbers[72] and as the temperature difference increases, the difference in local Nusselt number distributions of incompressible and compressible results will increase as well[9][69]. The temperature dependences of the fluid properties were considered as the reason for this difference.

Table 6.1. Convergence behaviors of hydrodynamic quantities and temperature gradient.

Ra	Ref.	$u_2^*{}_{\max}$ (x_1/L_1)	$\overline{Nu}$	Nu_{lmax}
1×10^{10}	F Trias[70]	0.264 (1.50×10^{-2})	101.70	454.86
	Present	0.254 (1.56×10^{-2})	102.12	426.69

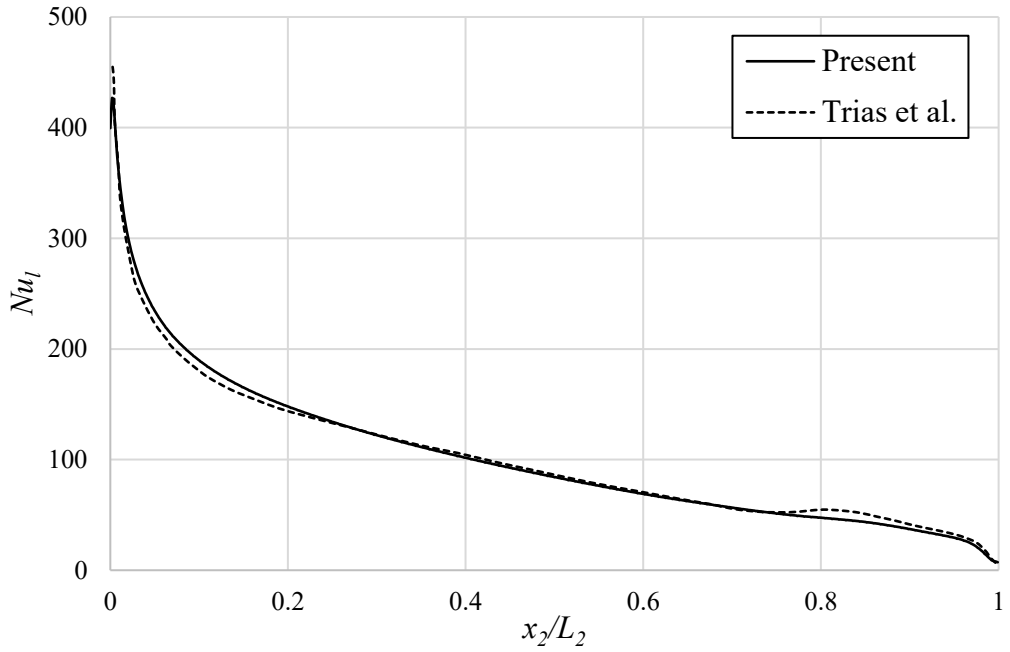

Figure 6.2. Local Nusselt number across the hot sidewall.

6.2.2 Probability density functions

In this section, the time traces of the temperature and the three components of the velocity have been monitored at 2 different locations near the hot sidewall of the cavities (see table 6.2). It is clear that the local geometry of the rough surface will affect the flow field near sidewalls, thus Figure 6.3 manifests the distributions of roughness elements near the locations of the probes, and the dashed lines in the figure denote the location of the smooth hot sidewall.

The probability density distributions of the temperature and three components of the velocity at the locations are investigated and shown in Figure 6.4 and Figure 6.5. The probability density function (*PDF*) is defined as the function of related thermal and

hydrodynamic quantities, f, and $\int_{-\infty}^{\infty} PDF(f)\, df = 1$. In these figures, the blue dash lines represent the average value of the measured physical quantities. From the profiles of *PFD*, it is noted that the obvious fluctuations of all measured quantities at probe A can be found around their average values, thus the flows in the downstream region of the cavity show the characteristic of turbulence. At location A, for the smooth cases, the average values of u_1* are positive and the *PDF* distributions of u_1* are not symmetrical with respect to the time-averaged values, i.e. the time-averaged u_1* is larger than the magnitude of u_1* which has maximum probability density. This is because the existence of the sidewalls and the effects of walls will prevent the occurrence of large negative velocity and the circulations in the cavities will give the fluid an obvious horizontal velocity in the downstream corners. But, for the flow field near the rough sidewall, the u_1* at A near the rough wall cannot reach the same maximum as the smooth case. Differently, it can be found in the PDF profiles of u_2*, for the rough case, the average and minimum of u_2* are larger than the smooth case. Meanwhile, due to the asymmetric distribution of the roughness elements, the profile of u_3* of the rough case is slightly asymmetric to its average value compared with the smooth case.

The probe location B is located near the mid-height of the cavity, therefore, the profiles at point B show a completely different phenomenon with point A. Overall, the fluctuation of the flow field at point B is much smaller than that at point A. It should be noted that for all monitored physical values, the spans of *PDF* profiles of the rough case are larger than the smooth case. This means the existence of roughness elements will enhance the instability of the flow in the mid-height region of the cavity at the *Ra* of 10^{10}.

Table 6.2. Locations of monitor probes.

Probe	x_1/L_1	x_2/L_2	x_3/L_3
A	0.05	0.85	0.5
B	0.05	0.55	0.5

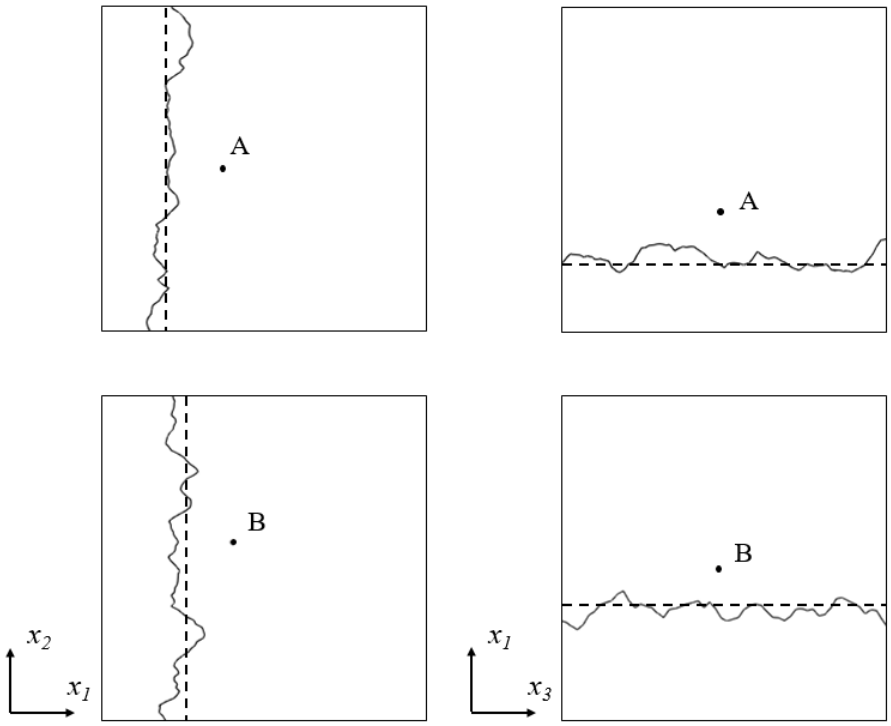

Figure 6.3. Probes and the distributions of roughness elements near the probes.

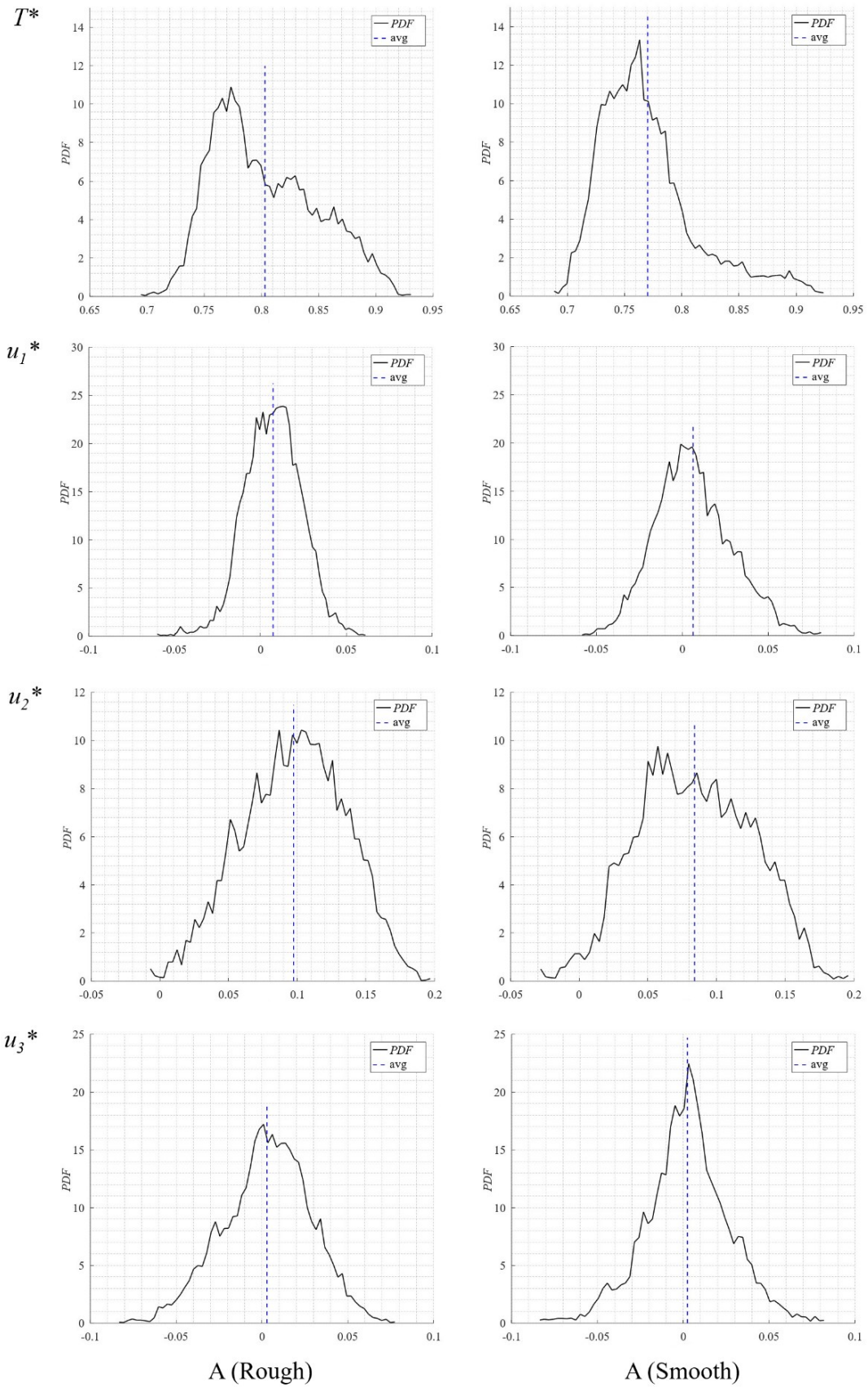

Figure 6.4. Probability density functions of thermal and hydrodynamic quantities at A.

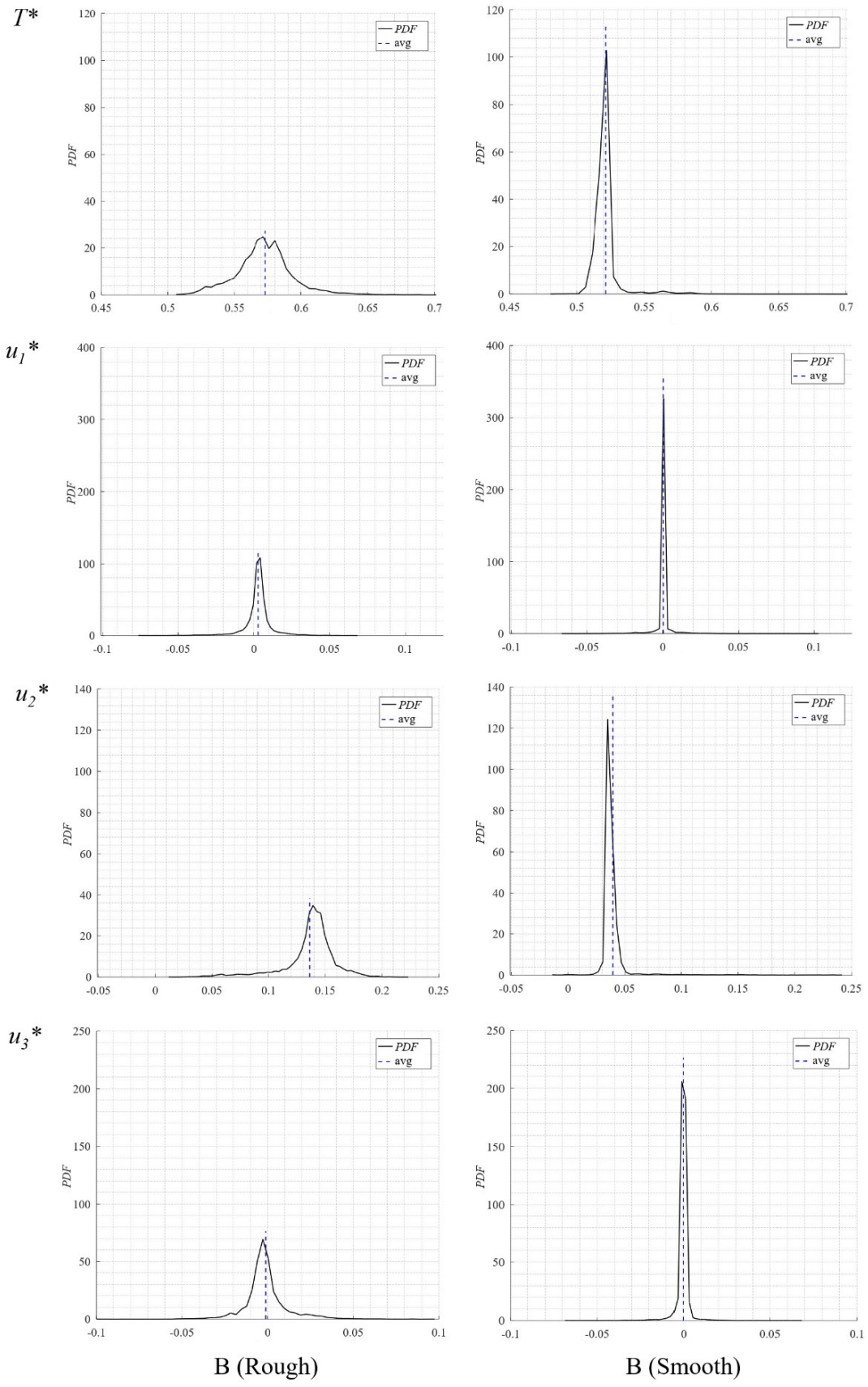

Figure 6.5. Probability density functions of thermal and hydrodynamic quantities at B.

6.2.3 Flow structures

The Q-criterion [73] has been adopted to investigate flow structures near the hot walls of cavities quantitively. Figure 6.6 shows the isosurfaces for different Q near the rough and smooth hot walls at the same instantaneous time step. The isosurfaces are colored by the nondimensional temperature. At Q = 500, for the rough sidewall, a large number of lumps of the isosurface emerge at the tips of roughness peaks, but in the downstream region, the velocity of the main flow decreases, and the number of lumps of the isosurface thus decreases gradually. We consider that these lumps are created by fluid flowing at relatively high velocities along the roughness peaks. Therefore, in the smooth case, there is no such apparent lump appearing when Q is reduced to 100, whereas in the rough case, the sizes of the lumps increase. Additionally, more lumps appear especially in the downstream region, and near the smooth wall, several lumps begin to emerge. At the lowest Q value of 20, the lumps are large near the rough wall but some connect away from the wall. Near the downstream corners, large and unsteady eddies are ejected from the sidewalls, generating strong recirculation. These eddies can also be observed but in more downstream locations near the smooth wall. Several transverse vortex structures appear in the smooth case, whereas there is no such vorticity in the rough case. We conclude from the results of the Q-criterion that surface roughness indeed affects flow structures near the sidewall. The roughness peaks notably increase the vorticity of the local fluid, and the mixing effect of this vorticity increases the local convection of the sidewall. However, these areas only account for a small part of the rough wall, and there is no evident lump on the Q-criterion isosurface in the valley areas.

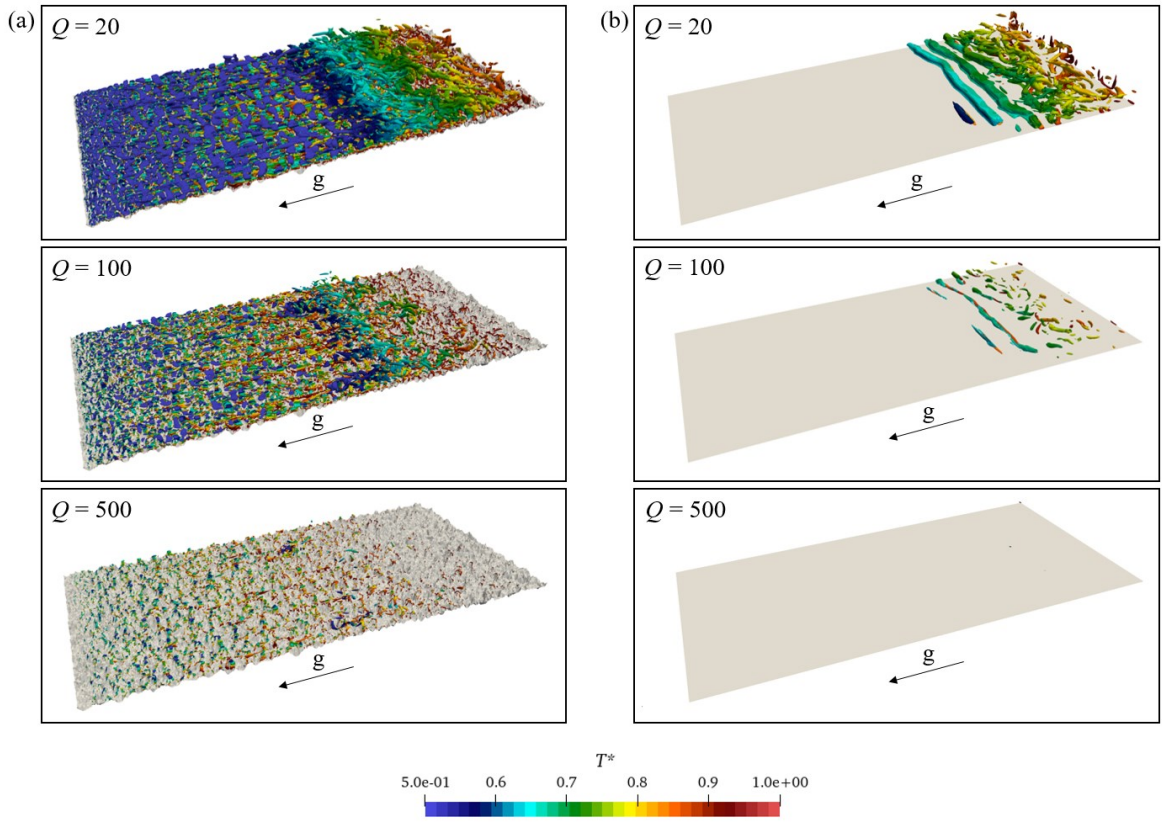

Figure 6.6. Isosurfaces of different Q colored by the nondimensional temperature near the hot sidewall in rough (a) and smooth (b) cases.

6.2.4 Thermal and flow fields

Figure 6.7 presents results of the temperature field in the cavities, where the nondimensional temperature T^* is calculated as $T^* = (T - T_C)/(T_H - T_C)$. For each pair of solutions, the results for the rough case are shown on the left and those for the smooth case are shown on the right. The figure clearly shows that the existence of roughness distorts the isothermal surface near the wall, but in the core regions of the cavities, the distributions of the isosurfaces are similar in rough and smooth cases. In the downstream region, wrinkles emerge on the isosurfaces, and it is considered that there are fluctuations in the local fluid in this area. These fluctuations are obviously stronger in the rough case than in the smooth case and emerge in an earlier region in the rough case. Figure 6.7 (b) and (c) shows the isotherms of cavities with rough and smooth sidewalls on mid-depth planes. In the upstream region, compared with the smooth case, the thickness of the thermal boundary layer decreases near the roughness peaks. This effect is particularly obvious near the large peaks. In the valley regions, however, the thickness of the thermal boundary layer has the opposite trend. Downstream, the instability

of the fluid increases, and the flow ejects many unsteady eddies to the core region of the cavity. Taking the hot sidewall as an example, this phenomenon increases the local temperature, and it is thus seen in Figure 6.7 that the thermal boundary layer in the rough case is thicker than that in the smooth case in the downstream region.

Figure 6.8 presents the nondimensional velocity magnitudes in the rough and smooth cases on two planes (x_1–x_2 plane at $x_3/L_3 = 0.5$ and x_2–x_3 plane at $x_1/L_1 = 0.005$). There is a clear effect of roughness on the velocity field near the walls. In the areas near roughness peaks, there are detectable accelerations of the flow, but the average velocity magnitude is lower in the rough case than in the smooth case, especially in the very upstream region and downstream regions. In the valley areas, the fluid decelerates obviously. Meanwhile, contours on the x_2–x_3 planes show the flow field near the hot sidewall of the cavities. The island-like objects in Figure 6.8 (a) are the roughness elements that protrude from the measurement plane. In the smooth case, because the measurement plane (at $x_1/L_1 = 0.005$) is located inside the velocity boundary layer, the magnitude of the velocity is much lower than the maximum of the main flow. In contrast, owing to the irregular roughness elements, there are many spaces among the elements, and the fluid in these spaces reaches a high speed under driving by the buoyancy force.

6.2.5 Heat transfer

This section uses the average and local Nusselt numbers to assess the effect of the rough sidewall on the heat transfer in the cavity flows. Figure 6.9 shows the distributions of the local Nusselt number on the hot walls in rough and smooth cases. In general, the distributions of the local Nusselt number have higher Nusselt numbers in the upstream region and lower numbers in the downstream region. In the local area, the roughness peaks increase the Nusselt number and the valleys decrease the Nusselt number, which is consistent with the thermal boundary layer distribution shown in Figure 6.7. After the upstream region, the effect of the roughness peaks diminishes, and only large peaks increase the Nusselt number. Meanwhile, the velocity of the fluid in the valley areas is low. Therefore, even in the very upstream part of the cavity hot wall, the reductions in the Nusselt number in the valley areas are appreciable. Table 6.3 gives the average Nusselt number and the maximum and minimum local Nusselt numbers for rough and smooth cases. In this study, the average Nusselt number over the entire hot sidewall is calculated according to the project area along the x_1-direction. In the table, there is a notable

increase in the maximum local Nusselt number because of the effect of roughness peaks. At the same time, the minimum local Nusselt number in the rough case is much smaller than that in the smooth case owing to the existence of the roughness valley. The average Nusselt number is 8.321% smaller in the rough case than in the smooth case; i.e., in this study, the heat transfer performance of the heated wall is aggravated by the wall roughness.

Taking into account the difference in thickness of the thermal boundary layer and the flow structures in the upstream and downstream regions, we separate the hot sidewall into 16 equal parts along the height direction. For each part, we calculate the integral of the local Nusselt number and define it as local average Nusselt number, as shown in Figure 6.10 (a). It is seen that the curves in rough and smooth cases have a similar tendency of a higher local average Nusselt number upstream and lower local average Nusselt number downstream. For most of these parts, local average Nusselt numbers are lower in the rough case. Only in the region of x_2/L_2 around 0.4 is the local average Nusselt number larger in the rough case than in the smooth case. This phenomenon can be explained in that the fluid in this region has been accelerated to a considerable speed and there are notable positive effects due to the large rough elements distributed at this position, and the local Nusselt number thus increases.

Figure 6.10 (b) shows the difference in the local average Nusselt number between the rough and smooth cases. Generally speaking, the difference is less than 10% in the region of $x_2/L_2 < 0.8$. However, in the downstream region, the difference increases as the measurement location moves downstream. As in the results shown in Figure 6.7 and 6.8, in the very downstream region, the thickness of the thermal boundary layer increases but the velocity magnitude decreases, and the effects of roughness peaks diminish such that it is difficult to overcome the negative effects of the roughness valleys. In summary, although the roughness peaks reduce the thickness of the thermal boundary layer and increase the local Nusselt number, the reduction from the valley areas is stronger than the increment from the peaks.

In this study, the local Nusselt number and average Nusselt number indicate the heat flux or energy transmission on the hot sidewall, and the fluctuation of the fluid is thus considered negligible in the calculation of the Nusselt number. However, at $Ra = 10^{10}$, turbulence becomes apparent, especially in the downstream corners of the cavity. The eddy heat flux is thus investigated to assess the rate of transfer of heat in the fluid by the turbulent eddies. The eddy heat flux is calculated as

$$EHF_i = \bar{\rho} C_p \overline{u_i' T'} \tag{6.1}$$

where *Cp* is the specific heat of the fluid and u' and T' are the fluctuations of the velocity and temperature respectively [74].

Figure 6.11 (a) and (b) shows the eddy heat flux due to the velocity fluctuations in width and height directions for the rough case whereas Figure 6.11 (c) and (d) presents the results for the smooth case. It is noted that the distributions of roughness elements affect the local flow field. Therefore, in evaluating the overall effect of roughness, the results shown in Figure 6.11 are based on the spanwise average eddy heat flux along the depth direction. Consistent with the results of the flow field, the unsteady eddies in the downstream corners increase the eddy heat flux in height and width directions. Additionally, it is clear that the eddy heat flux along the main flow direction is much stronger than that in the other direction for both rough and smooth cases. The figure shows that the eddy heat flux has a higher magnitude in the rough case than in the smooth case for both height and width directions. Meanwhile, compared with the smooth case, the point at which notable high eddy heat flux appears moves upstream in the rough case. Especially for the eddy heat flux generated by the fluctuations of the main flow, the high eddy heat flux emerges in the very upstream region. In general, the hot sidewall transfers heat to the fluid in the width direction. Figure 6.11 (a) and (c) shows that the roughness enhances the eddy heat flux along x_1-direction (EHF_1). The existence of roughness elements disrupts the development of the velocity boundary layer, and this disruption facilitates the exchange of fluid near the boundary layer. Owing to the flow having a higher magnitude of velocity in the main flow direction, the flow is more sensitive to the roughness in this direction, which explains how the roughness increases the eddy heat flux along x_2-direction (EHF_2) sharply.

To investigate the convective process near the solid surface, the wall shear stress and area-averaged wall shear stress on the hot sidewalls are measured. Figure 6.8 shows that, owing to the irregular roughness elements and the spaces among the roughness elements, the fluid bypasses the roughness elements, and the two components of velocity perpendicular to the main flow direction are then much higher than those in the smooth case. This study thus considers the tangential velocity near the wall as [75]

$$\tau_w = \mu \frac{\partial u_t}{\partial n}\bigg|_{wall} \tag{6.2}$$

where τ_w is the wall shear stress and u_t is the tangential wall velocity with respect to the local wall surface. The area-averaged wall shear stress provides the overall magnitude of the wall shear stress of the rough or smooth sidewall:

$$\overline{\tau_w} = \frac{1}{A}\int |\tau_w|\, dA \tag{6.3}$$

Figure 6.12 shows the distributions of the shear stress on the hot rough and smooth walls. Similar to the local Nusselt number distribution, in the areas of roughness peaks, the local wall shear stress is much higher than that in the smooth case, but in the valley areas, the shear stress is much lower. Table 6.4 gives the average values and the extrema of the wall shear stress on hot sidewalls in rough and smooth cases. The maximum value of the local wall shear stress on the rough sidewall is much greater than that in the smooth case, but the average shear stress in the rough case is only half that in the smooth case. According to the definition of shear stress, the velocity gradient plays a decisive role in determining the magnitude of shear stress. The fluid flows slowly in the valley areas, and the velocity gradients in the same areas are thus low inevitably. Meanwhile, the fluid near the peaks of roughness undergoes obvious acceleration, and the velocity gradients near these regions are thus much larger than those in other regions. The convective effects near the roughness peaks are thus stronger than those near the roughness valleys.

The results of the average Nusselt number and wall shear stress show that the irregular roughness on the sidewall has a negative effect on the heat transfer of the cavity flows in the case of vertical natural convection. This is opposite of the case for forced convection, where an irregularity has been widely shown to enhance the surface heat transfer but increase the wall shear stress notably [41,42,76]. The reason is that the driving forces of these two convection flows are different. In forced convection, there is usually a constant external source as the driving force. However, in natural convection, the only driving force is the buoyancy force, which depends on energy transfer from the heat source. Returning to the present study, the variances of velocity and temperature of the fluid inside the cavity originate from the energy conveyed from the hot sidewall. Therefore, this energy is calculated according to the heat flux of the wall as

$$q_w = k\frac{\partial T}{\partial n}\bigg|_{wall} \tag{6.4}$$

$$E_w = \int q_w \, dA \tag{6.5}$$

It is clear that the conveyed energy is dominated by the surface heat flux, and the energy can thus be evaluated using the average Nusselt number. Table 6.3 shows that, even if the rough sidewall has a greater area, the energy coming from the rough sidewall is less than that coming from the smooth hot sidewall. Owing to the thermal boundary condition imposed on the hot and cold sidewalls of the cavities, the magnitudes of the local heat flux in different regions are different. The above results indicate that, in the areas of roughness valleys, the temperature of the fluid is high and the temperature gradient is thus low. This situation makes it difficult to transfer energy from the hot sidewall. Less energy is transferred from the rough wall, and the slight buoyancy is thus unable to drive the fluid in the roughness valley areas. Therefore, the fluid in the valleys flows at low velocity. The overall convection near the rough wall is then weaker than that in the smooth case.

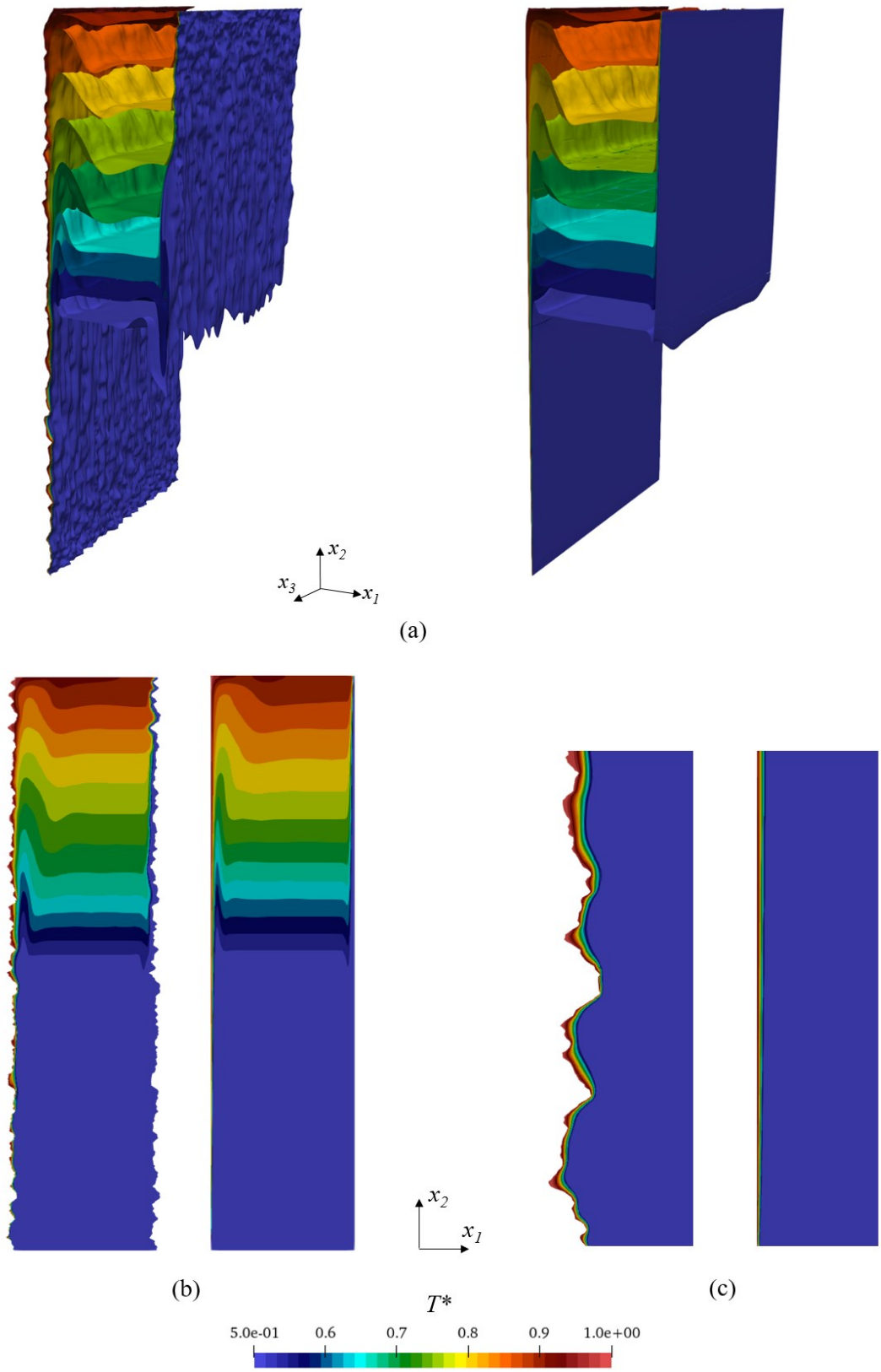

Figure 6.7. Temperature distributions near the hot sidewall: (a) isothermal surfaces, (b) temperature on the mid-depth plane ($x_3/L_3 = 0.5$), and (c) temperature in the upstream region on the mid-depth plane.

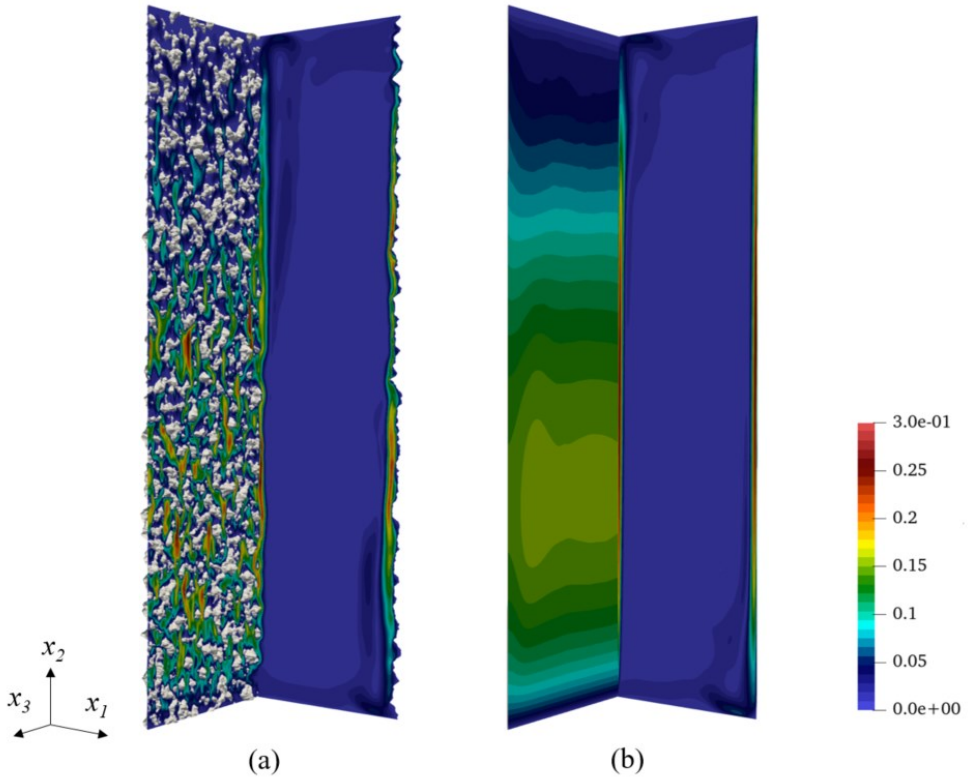

Figure 6.8. Nondimensional velocity magnitudes in rough (a) and smooth (b) cases. In both cases, the x_1–x_2 plane is located at the mid-depth of the cavity ($x_3/L_3 = 0.5$) and the x_2–x_3 plane is located at $x_1/L_1 = 0.005$.

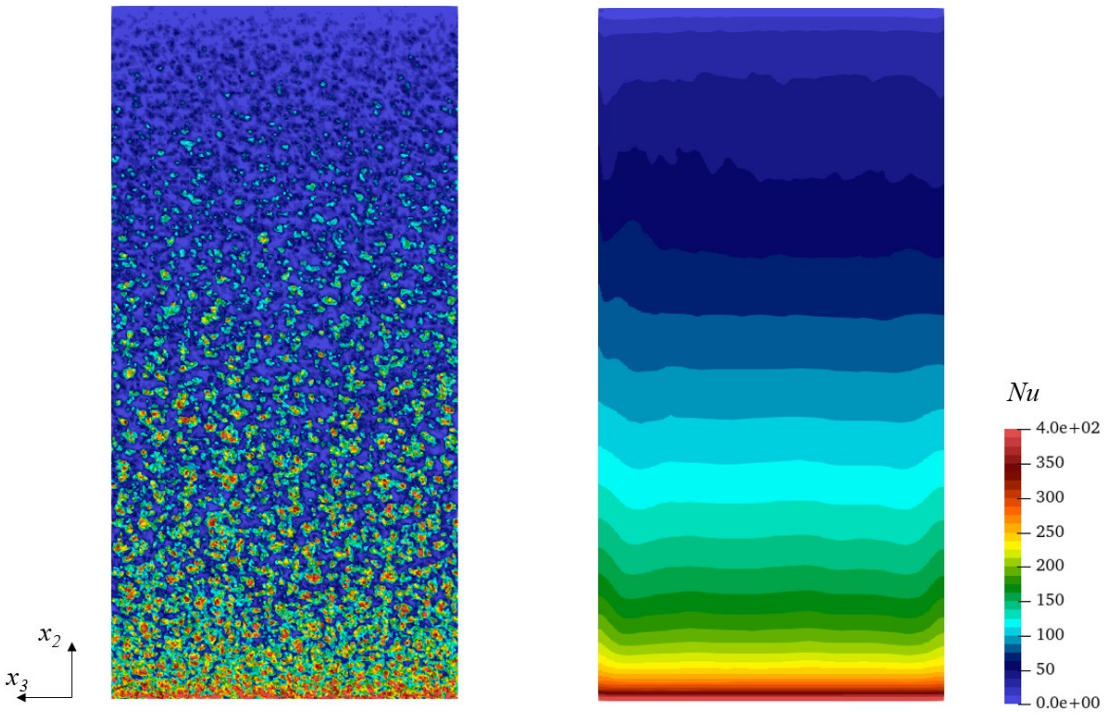

(a) (b)

Figure 6.9. Distributions of the local Nusselt number on the hot sidewalls in the (a) rough and (b) smooth cases.

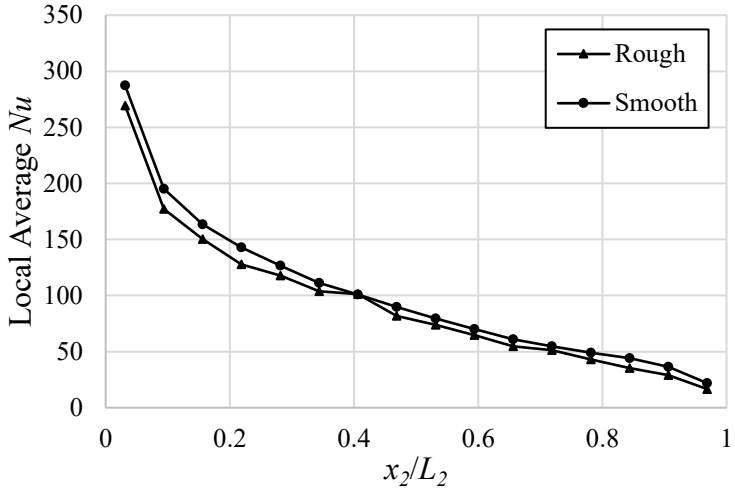

(a)

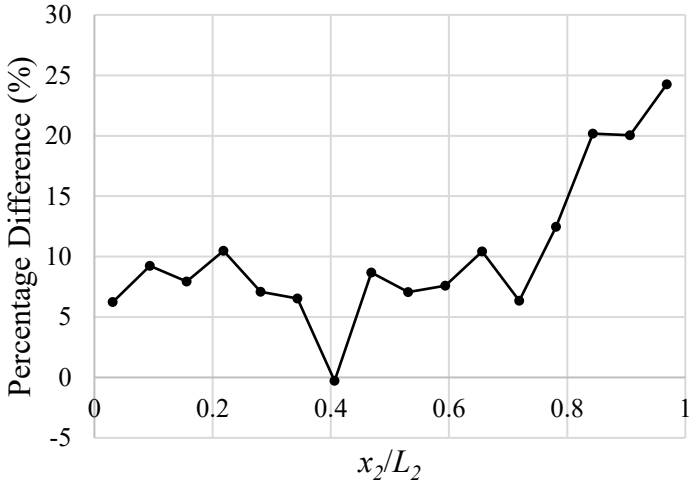

(b)

Figure 6.10. Local average Nusselt number (a) and the difference (b) between rough and smooth cases.

Table 6.3. Averaged Nusselt number and extrema of the local Nusselt number

	Rough	Smooth
$\overline{Nu}$	93.625	102.123
Nu_{lmax}	584.206	428.126
Nu_{lmin}	0.016	5.178

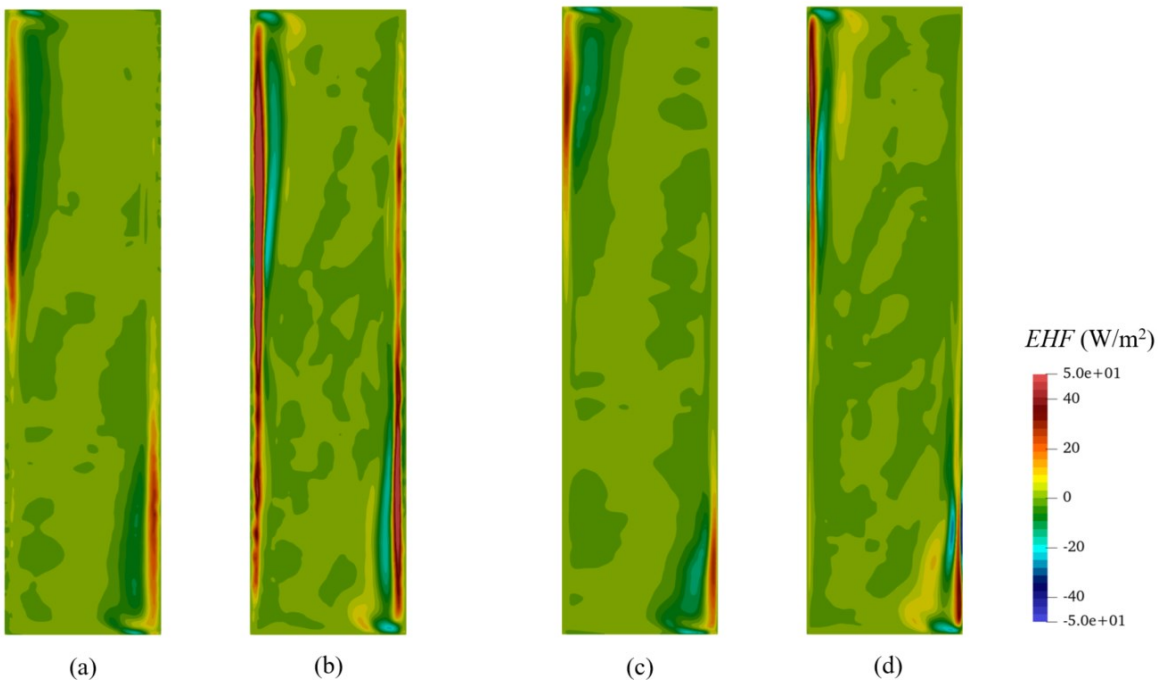

Figure 6.11. Eddy heat flux: EHF_1 (a) and EHF_2 (b) in the rough case and EHF_1 (c) and EHF_2 (d) in the smooth case.

Table 6.4. Comparison of wall shear stress between rough and smooth cases

	Rough	Smooth
$\overline{\tau_w}$ ($\times 10^{-3}$)	0.939	1.989
τ_{wmax} ($\times 10^{-3}$)	7.34	2.95
τ_{wmin} ($\times 10^{-3}$)	8.76×10^{-5}	6.25×10^{-4}

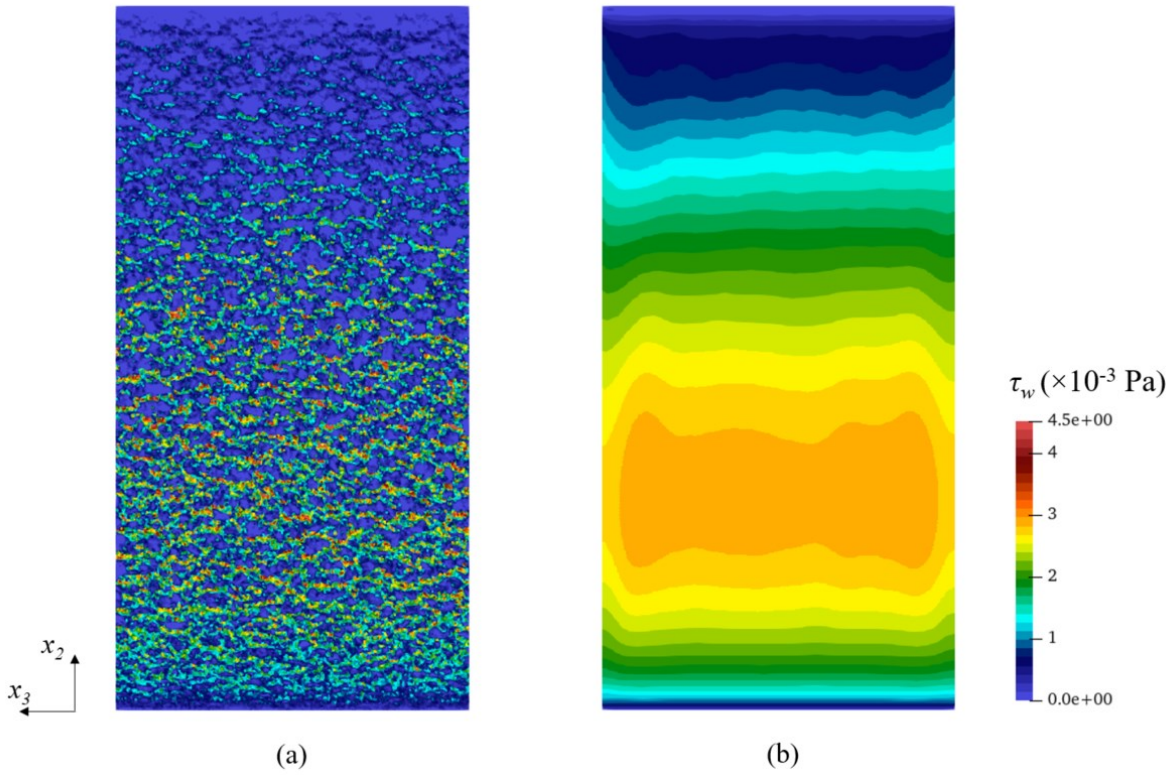

Figure 6.12. Distributions of wall shear stress on the hot walls in (a) rough and (b) smooth cases.

6.2.6 Effect of roughness under different Rayleigh numbers

This section discusses the effects of rough surfaces on the heat transfer performance at different Rayleigh numbers. The Rayleigh number is changed by varying only the height of the cavity while keeping the temperature difference between hot and cold sidewalls, the aspect ratios of cavities, and other physical parameters constant. Meanwhile, the geometric model of

the roughness is scaled proportionally according to the ratios of the cavity heights. Four different Rayleigh numbers (Ra = 10^6, 10^7, 6.4×10^8, and 10^{10}) are set. Table 6.5 gives the grids used for different Rayleigh numbers. As shown in this table, for all these four Ra, the finest resolution near the sidewalls is kept constant to ensure sufficient numerical grids to capture geometric details. Considering the low Ra, the fluid shows more laminar and steady, so the coarser grid structure has been used in the core region of the enclosure then the total number of the numerical grid is smaller than that of higher Ra. The differences in $\overline{Nu}$ on the hot sidewall between rough and smooth cases are shown in Figure 6.13. These differences are calculated according to $\text{Difference} = (\overline{Nu}_{smooth} - \overline{Nu}_{rough})/\overline{Nu}_{smooth} \times 100\%$), and a positive difference thus indicates that the heat transfer on the rough sidewall is worse than that on the smooth sidewall. In the figure, there is the notable tendency that as the Rayleigh number increases, the difference between rough and smooth cases decreases. For Ra = 10^6 and 10^7, the flows in cavities have features of laminar flow, and the negative effects of a rough surface are more obvious than those in the case of the highest Rayleigh number. In the four cases, a higher Rayleigh number can be considered to correspond to more turbulent flow, and the negative effects of the roughness are alleviated by the mixing effects of the eddies. We thus expect that the gap between rough and smooth cases will narrow further as the Rayleigh number increases further.

Table 6.5. Numerical grids for different Rayleigh numbers

Ra	Finest grids ($\Delta x_{imin}/L_2$)	Total grid number (millions)
10^6	2048	260
10^7	2048	260
6.4×10^8	2048	450
1×10^{10}	2048	450

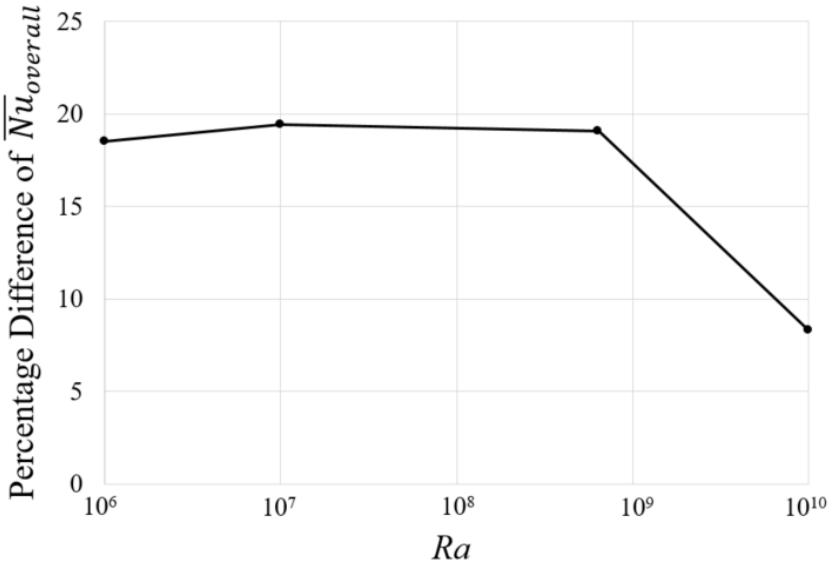

Figure 6.13. Differences in the averaged Nusselt number between rough and smooth cases for different Rayleigh numbers.

CHAPTER 7. CONCLUSION AND RECOMMENDATIONS

7.1 Conclusion

This dissertation has focused on the influence of surface roughness on the heat transfer performance of natural convection flows inside the enclosure cavities. Considering the universality of environments with high-temperature difference in modern industry and nature, the working fluid has been treated as compressible and simulations have been conducted under the non-Boussinesq conditions. On the other hand, to fit the reality, the isotropic self-affine roughness has been taken into account. The irregular roughness is generated through the given power spectrum densities. The total dissertation is trying to research the effects of different irregular roughness on the surface heat transfer under a laminar condition and the influence of one irregular roughness on the laminar and turbulent natural convection in enclosures.

In Chapter 4, the natural convection in a cavity with 3D irregular roughness elements on sidewalls has been investigated at the Rayleigh number of 10^6, using a compressible solver. The roughness was generated through a given power spectrum density with the roll-off wavenumber equal to 10^3 m^{-1} and the temperature difference between two sidewalls was 50K. The results of thermal fields showed the peaks on the rough surface will decrease the thickness of the thermal boundary layer but the valleys will increase it in the upstream region. However, in the downstream region, the thickness of the thermal boundary layer is thick enough that this effect is no longer obvious. Near the hot sidewall, the peaks will accelerate the flow field slightly, but the valleys will give a conspicuous deceleration to the flow field, and this phenomenon exists in both upstream and downstream regions. On the other hand, the fluid will bypass the elements in 3D simulation instead of getting trapped between two roughness elements.

The influence of different irregular rough surfaces on heat transfer was investigated in Chapter 5. By changing the roll-off wavenumber, 4 different irregular rough surfaces were generated. An accurate method to measure the temperature gradient on the complex surface was applied and the results showed that as the q_R^* increases the average Nu on the surfaces decreases under the condition of $Ra = 10^6$. Another notable phenomenon is that large q_R^* indicated the denser distribution of the roughness elements with short wavelengths, then these roughness peaks were able to amplify the maximums of local Nu, but meanwhile, the space

among the roughness elements would be separated into small pieces by these roughness peaks and valleys. After dividing the average *Nu* into top average *Nu* and bottom average *Nu*, the results showed that the bottom average *Nu* was more sensitive to the change of q_R^* than the top average *Nu*, and as q_R^* increased, the bottom average *Nu* had a conspicuous tendency to decrease.

Chapter 6 investigated compressible natural convection flows in a cuboid cavity with 3D irregular roughness elements on its sidewalls at a Rayleigh number of 1×10^{10} based on DNS. The irregular roughness with q_R^* of 32 was same as in Chapter 5. The power density functions of the temperatures and velocities at the monitor probes were measured and the profiles of *PDF* show the flows in the downstream regions had the features of turbulence and the roughness increased the fluctuations of the flows nearby. From the isosurfaces of Q-criterion near both rough and smooth sidewall, we noted that the roughness was able to increase the vorticity and change the structures of the fluid nearby, but the vortices only appeared in the local areas of roughness peaks, and the fluid in valley areas kept a very low rotation rate. The time-averaged results indicated that in the local areas, the roughness peak accelerated the fluid nearby, and then the local convection increased, but the roughness valley had an opposite effect on the fluid. Thus the distributions of local Nusselt numbers have a high value in the vicinity of roughness peaks but the low in valley regions. From the average *Nu* on the hot sidewall, the rough case is lower than the smooth case by nearly 8%. But results of *EHF* indicated that the heat transfer generated by the turbulence near the rough surface was much higher than the smooth case, and compared with the smooth case, conspicuous *EHF* could be found from a more upstream area near the rough sidewalls. Analysis of the total energy transferred from the hot sidewalls revealed that the smooth sidewall conveyed more energy than the rough sidewall on the basis of the isothermal boundary condition. The convection near the rough sidewall was weaker than that near the smooth wall, and the shear stress was lower in the rough case than in the smooth case. As the *Ra* increases, the difference of average Nusselt numbers between smooth and rough cases will be diminished, and the mixing effects of turbulence played an important role in this tendency.

The current study clarified the effects of isotropic irregular roughness on the compressible natural convection flows in enclosed cavities under both laminar and turbulent conditions without Boussinesq approximation. Meanwhile, the flow structures near the rough surfaces were represented in detail. The results of this dissertation can provide a reference for the design of engineering applications involving high-temperature problems.

7.2 Recommendations for future work

The following recommendations can be considered as potential directions for further research.

- It would be very interesting to investigate the influence of different irregular roughness under the condition of turbulence.
- Higher temperature difference could be imposed on both sidewalls to research the effects of the roughness on the heat transfer performance and flow structures under the extremely thermal boundary condition.
- The thermal boundary condition imposed on the sidewalls could be considered as constant heat flux instead of isothermal.
- The types of roughness surface could be extended such as anisotropic roughness which also extensively exists in modern industry.

Reference

[1] Barhaghi D G. A study of turbulent natural convection boundary layers using large-eddy simulation[M]. Chalmers University of Technology, Department of Applied Mechanics, 2007.

[2] Ozisik M N. Heat transfer: a basic approach[M]. New York: McGraw-Hill, 1985.

[3] Takahashi N, Duan G, Furuya M, et al. Analysis of hemispherical vessel ablation failure involving natural convection by MPS method with corrective matrix[J]. International Journal of Advanced Nuclear Reactor Design and Technology, 2019, 1: 19-29.

[4] Zhou Z, Liu K, Xu L, et al. Study on propagation characteristics of laser in turbulent Rayleigh–Bénard thermal convection[J]. The Journal of Engineering, 2019, 2019(20): 6902-6905.

[5] Spiegel E A, Veronis G. On the Boussinesq approximation for a compressible fluid[J]. The Astrophysical Journal, 1960, 131: 442.

[6] Gray D D, Giorgini A. The validity of the Boussinesq approximation for liquids and gases[J]. International Journal of Heat and Mass Transfer, 1976, 19(5): 545-551.

[7] Zhong Z Y, Yang K T, Lloyd J R. Variable property effects in laminar natural convection in a square enclosure[J]. 1985.

[8]Chenoweth D R, Paolucci S. Natural convection in an enclosed vertical air layer with large horizontal temperature differences[J]. Journal of fluid mechanics, 1986, 169: 173-210.

[9] Paillere H, Viozat C, Kumbaro A, et al. Comparison of low Mach number models for natural convection problems[J]. Heat and mass transfer, 2000, 36(6): 567-573.

[10] Quere P. Le, Weisman C., Paillere H., Vierendeels J., Dick E., Becker R., Braack M. and Locke J., 2005, Modelling of natural convection flows with large temperature differences: A benchmark problem for low Mach number solvers. Part 1. Reference solutions, ESAIM: Mathematical Modelling and Numerical Analysis, 39, 609 – 616

[11] Talukdar D, Li C G, Tsubokura M. Numerical investigation of buoyancy-driven compressible laminar flow using new method preconditioned all-speed roe scheme[J]. International Communications in Heat and Mass Transfer, 2018, 98: 74-84.

[12] Hamimid S, Guellal M, Bouafia M. Limit of the buoyancy ratio in Boussinesq approximation for double-diffusive convection in binary mixture[J]. Physics of Fluids, 2021, 33(3): 036101.

[13] Fusegi T, Hyun J M. Laminar and transitional natural convection in an enclosure with complex and realistic conditions[J]. International journal of heat and fluid flow, 1994, 15(4): 258-268.

[14] Nayak P R. Random process model of rough surfaces[J]. 1971.

[15] Wagner S, Shishkina O. Heat flux enhancement by regular surface roughness in turbulent thermal convection[J]. Journal of Fluid Mechanics, 2015, 763: 109-135.

[16] Yang X I A, Meneveau C. Modelling turbulent boundary layer flow over fractal-like multiscale terrain using large-eddy simulations and analytical tools[J]. Philosophical Transactions of the Royal Society A: Mathematical, Physical and Engineering Sciences, 2017, 375(2091): 20160098.

[17] Ren J. Micro/nano scale surface roughness tailoring and its effect on microfluidic flow[J]. Iowa State University, 2013.

[18] Jacobs T D B, Junge T, Pastewka L. Quantitative characterization of surface topography using spectral analysis[J]. Surface Topography: Metrology and Properties, 2017, 5(1): 013001.

[19] Duparre A, Ferre-Borrull J, Gliech S, et al. Surface characterization techniques for determining the root-mean-square roughness and power spectral densities of optical components[J]. Applied optics, 2002, 41(1): 154-171.

[20] Weiss J M, Smith W A. Preconditioning applied to variable and constant density flows[J]. AIAA journal, 1995, 33(11): 2050-2057.

[21] Yamamoto S, Niiyama D, Shin B R. A numerical method for natural convection and heat conduction around and in a horizontal circular pipe[J]. International journal of heat and mass transfer, 2004, 47(26): 5781-5792.

[22] Turkel E. Preconditioning techniques in computational fluid dynamics[J]. Annual Review of Fluid Mechanics, 1999, 31(1): 385-416.

[23] de Vahl Davis G. Natural convection of air in a square cavity: a bench mark numerical solution[J]. International Journal for numerical methods in fluids, 1983, 3(3): 249-264.

[24] Markatos N C, Pericleous K A. Laminar and turbulent natural convection in an enclosed cavity[J]. International journal of heat and mass transfer, 1984, 27(5): 755-772.

[25] Le Quéré P. Accurate solutions to the square thermally driven cavity at high Rayleigh number[J]. Computers & Fluids, 1991, 20(1): 29-41.

[26] Barakos G, Mitsoulis E, Assimacopoulos D O. Natural convection flow in a square cavity revisited: laminar and turbulent models with wall functions[J]. International journal for numerical methods in fluids, 1994, 18(7): 695-719.

[27] Chenoweth D R, Paolucci S. Natural convection in an enclosed vertical air layer with large horizontal temperature differences[J]. Journal of fluid mechanics, 1986, 169: 173-210.

[28] Wang Q, Xia S N, Yan R, et al. Non-Oberbeck-Boussinesq effects due to large temperature differences in a differentially heated square cavity filled with air[J]. International Journal of Heat and Mass Transfer, 2019, 128: 479-491.

[29] Demou A D, Frantzis C, Grigoriadis D G E. A low-Mach methodology for efficient direct numerical simulations of variable property thermally driven flows[J]. International Journal of Heat and Mass Transfer, 2019, 132: 539-549.

[30] Soria M, Trias F X, Pérez-Segarra C D, et al. Direct numerical simulation of a three-dimensional natural-convection flow in a differentially heated cavity of aspect ratio 4[J]. Numerical Heat Transfer, Part A: Applications, 2004, 45(7): 649-673.

[31] Corcione M. Heat transfer features of buoyancy-driven nanofluids inside rectangular enclosures differentially heated at the sidewalls[J]. International Journal of Thermal Sciences, 2010, 49(9): 1536-1546.

[32] Gvozdić B, Alméras E, Mathai V, et al. Experimental investigation of heat transport in homogeneous bubbly flow[J]. Journal of fluid mechanics, 2018, 845: 226-244.

[33] Liu Y, Lei C, Patterson J C. Natural convection in a differentially heated cavity with two horizontal adiabatic fins on the sidewalls[J]. International Journal of Heat and Mass Transfer, 2014, 72: 23-36.

[34] Xu F, Patterson J C, Lei C. Transient natural convection flows around a thin fin on the sidewall of a differentially heated cavity[J]. Journal of fluid mechanics, 2009, 639: 261-290.

[35] Dou H S, Jiang G. Numerical simulation of flow instability and heat transfer of natural convection in a differentially heated cavity[J]. International Journal of Heat and Mass Transfer, 2016, 103: 370-381.

[36] Yousaf M, Usman S. Natural convection heat transfer in a square cavity with sinusoidal roughness elements[J]. International Journal of Heat and Mass Transfer, 2015, 90: 180-190.

[37] Shakerin S, Bohn M, Loehrke R I. Natural convection in an enclosure with discrete roughness elements on a vertical heated wall[J]. International journal of heat and mass transfer, 1988, 31(7): 1423-1430.

[38] Mohebbi R, Izadi M, Sidik N A C, et al. Natural convection heat transfer of nanofluid inside a cavity containing rough elements using lattice Boltzmann method[J]. International Journal of Numerical Methods for Heat & Fluid Flow, 2019.

[39] Jiang H, Zhu X, Mathai V, et al. Convective heat transfer along ratchet surfaces in vertical natural convection[J]. Journal of fluid mechanics, 2019, 873: 1055-1071.

[40] Napoli E, Armenio V, De Marchis M. The effect of the slope of irregularly distributed roughness elements on turbulent wall-bounded flows[J]. Journal of Fluid Mechanics, 2008, 613: 385-394.

[41] Peeters J W R, Sandham N D. Turbulent heat transfer in channels with irregular roughness[J]. International Journal of Heat and Mass Transfer, 2019, 138: 454-467.

[42] Kuwata Y. Direct numerical simulation of turbulent heat transfer on the Reynolds analogy over irregular rough surfaces[J]. International Journal of Heat and Fluid Flow, 2021, 92: 108859.

[43] Xiong R, Chung J N. A new model for three-dimensional random roughness effect on friction factor and heat transfer in microtubes[J]. International Journal of Heat and Mass Transfer, 2010, 53(15-16): 3284-3291.

[44] Li C G, Tsubokura M, Bale R. Framework for simulation of natural convection in practical applications[J]. International Communications in Heat and Mass Transfer, 2016, 75: 52-58.

[45] Jansson N, Bale R, Onishi K, et al. CUBE: A scalable framework for large-scale industrial simulations[J]. The international journal of high performance computing applications, 2019, 33(4): 678-698.

[46] Anderson Jr J D. Hypersonic and high-temperature gas dynamics[M]. American Institute of Aeronautics and Astronautics, 2006.

[47] Roe P L. Approximate Riemann solvers, parameter vectors, and difference schemes[J]. Journal of computational physics, 1981, 43(2): 357-372.

[48] Venkateswaran S, Merkle C. Dual time-stepping and preconditioning for unsteady computations[C]//33rd Aerospace Sciences Meeting and Exhibit. 1995: 78.

[49] Abalakin I, Dervieux A, Kozubskaya T A. A vertex centered high order MUSCL scheme applying to linearised Euler acoustics[J]. 2002.

[50] R. Ghias, R. Mittal, H. Dong, A sharp interface immersed boundary method for compressible viscous flows [J], Journal of Computational Physics 225 (1) (2007) 528–553.

[51] de Tullio M D, De Palma P, Iaccarino G, et al. An immersed boundary method for compressible flows using local grid refinement[J]. Journal of Computational Physics, 2007, 225(2): 2098-2117.

[52] Nakahashi K, Kim L. Building-cube method for large-scale, high resolution flow computations[C]//42nd AIAA Aerospace Sciences Meeting and Exhibit. 2004: 434.

[53] Nishiguchi K, Bale R, Okazawa S, et al. Full Eulerian deformable solid-fluid interaction scheme based on building-cube method for large-scale parallel computing[J]. International Journal for Numerical Methods in Engineering, 2019, 117(2): 221-248.

[54] Jansson N, Bale R, Onishi K, et al. CUBE: A scalable framework for large-scale industrial simulations[J]. The international journal of high performance computing applications, 2019, 33(4): 678-698.

[55] Gadelmawla E S, Koura M M, Maksoud T M A, et al. Roughness parameters[J]. Journal of materials processing Technology, 2002, 123(1): 133-145.

[56] M.M. Kanafi, A.J. Tuononen, Top topography surface roughness power spectrum for pavement friction evaluation [J], Tribology International 107 (2017) 240–249.

[57] Y. Xian, P. Zhang, S. Zhai, et al., Re-estimation of thermal contact resistance considering near-field thermal radiation effect [J], Applied Thermal Engineering 157 (2019) 113601.

[58] Chatfield C. The analysis of time series: an introduction[M]. Chapman and hall/CRC, 2003.

[59] Duparre A, Ferre-Borrull J, Gliech S, et al. Surface characterization techniques for determining the root-mean-square roughness and power spectral densities of optical components[J]. Applied optics, 2002, 41(1): 154-171.

[60] Persson B N J, Albohr O, Tartaglino U, et al. On the nature of surface roughness with application to contact mechanics, sealing, rubber friction and adhesion[J]. Journal of physics: Condensed matter, 2004, 17(1): R1.

[61] Persson B N J. Contact mechanics for randomly rough surfaces[J]. Surface science reports, 2006, 61(4): 201-227.

[62] Pelliccione M, Lu T M. Evolution of thin film morphology[M]. New York: Springer New York, 2008.

[63] Jacobs T D B, Junge T, Pastewka L. Quantitative characterization of surface topography using spectral analysis[J]. Surface Topography: Metrology and Properties, 2017, 5(1): 013001.

[64] Barabási A L, Stanley H E. Fractal concepts in surface growth[M]. Cambridge university press, 1995.

[65] Tric E, Labrosse G, Betrouni M. A first incursion into the 3D structure of natural convection of air in a differentially heated cubic cavity, from accurate numerical solutions[J]. International Journal of Heat and Mass Transfer, 2000, 43(21): 4043-4056.

[66] Xu A, Shi L, Xi H D. Lattice Boltzmann simulations of three-dimensional thermal convective flows at high Rayleigh number[J]. International Journal of Heat and Mass Transfer, 2019, 140: 359-370.

[67] R.A. Kuyper, T.H. Van Der Meer, C.J. Hoogendoorn, et al., Numerical study of laminar and turbulent natural convection in an inclined square cavity [J], International Journal of Heat and Mass Transfer 36 (11) (1993) 2899–2911.

[68] T. Fusegi, J.M. Hyun, Laminar and transitional natural convection in an enclosure with complex and realistic conditions [J], International Journal of Heat and Fluid Flow 15 (4) (1994) 258–268.

[69]Ren B, Li C G, Tsubokura M. Laminar natural convection in a square cavity with 3D random roughness elements considering the compressibility of the fluid[J]. International Journal of Heat and Mass Transfer, 2021, 173: 121248.

[70] Trias F X, Soria M, Oliva A, et al. Direct numerical simulations of two-and three-dimensional turbulent natural convection flows in a differentially heated cavity of aspect ratio 4[J]. Journal of Fluid Mechanics, 2007, 586: 259-293.

[71] Wang G, Yang F, Wu K, et al. Estimation of the dissipation rate of turbulent kinetic energy: A review[J]. Chemical Engineering Science, 2021, 229: 116133.

[72] Demou A D, Grigoriadis D G E. Variable property DNS of differentially heated cavities filled with air[J]. International Journal of Heat and Mass Transfer, 2020, 149: 119259.

[73] Jeong J, Hussain F. On the identification of a vortex[J]. Journal of fluid mechanics, 1995, 285: 69-94.

[74] Fleagle R G, Businger J A. An Introduction to Annospheric Physics, 2d ed. New York[J]. International Geophysics Series, 1980, 25.

[75] Owen D G, Schenkel T, Shepherd D E T, et al. Assessment of surface roughness and blood rheology on local coronary haemodynamics: a multi-scale computational fluid dynamics study[J]. Journal of the Royal Society Interface, 2020, 17(169): 20200327.

[76]Thakkar M, Busse A, Sandham N. Surface correlations of hydrodynamic drag for transitionally rough engineering surfaces[J]. Journal of Turbulence, 2017, 18(2): 138-169.

神戸大学博士論文「圧縮性自然対流における不規則粗度の影響に関する数値解析」
全８３頁

提 出 日 ２０２３年1月１７日

本博士論文が神戸大学機関リポジトリ Kernel にて掲載される場合、掲載登録日（公開日）はリポジトリの該当ページ上に掲載されます。

Doctor Thesis, Kobe University “A numerical study on the irregular roughness effects in compressible natural convection flow”, 83 pages

Submitted on January, 17th, 2023

The date of publication is printed in cover of repository version published in Kobe University Repository Kernel.